Rochester Institute of Technology

RIT Digital Institutional Repository

7-2023

Diffractive Light and Solar Sails

Prateek Ranjan Srivastava
prs7786@rit.edu

Diffractive Light and Solar Sails

by

Prateek Ranjan Srivastava

B.Sc(Hons), Banaras Hindu University (BHU), 2013
M.Sc., Indian Institute of Technology Delhi (IIT-Delhi), 2015

A dissertation submitted in fulfillment of the
requirements for the degree of
Doctor of Philosophy in Imaging Science
at
The Chester F. Carlson Center for Imaging Science
College of Science
Rochester Institute of Technology, USA

July 2023

Signature of the Author _____

Accepted by _____
Coordinator, Ph.D. Degree Program   Date

CHESTER F. CARLSON CENTER FOR IMAGING SCIENCE

COLLEGE OF SCIENCE

ROCHESTER INSTITUTE OF TECHNOLOGY

ROCHESTER, NEW YORK

CERTIFICATE OF APPROVAL

Ph.D. DEGREE DISSERTATION

The Ph.D. Degree dissertation of
Prateek Ranjan Srivastava
has been examined and approved by the
dissertation committee as satisfactory
for the thesis required for the
Ph.D. degree in Imaging Science

Dr. Grover A. Swartzlander, Jr., Advisor	Date
Dr. Emmett J. Ientilucci	Date
Dr. Charles Bachmann	Date
Dr. Seth Hubbard (External)	Date

Acknowledgements

Abstract

In the realm of space exploration, humanity has achieved remarkable feats like landing humans on the moon. However, our progress in venturing beyond our solar system has been limited. Light sails, which utilize photon momentum from laser or solar radiation, offer a promising propulsion technology. Unlike traditional rockets, light sails carry no fuel and can achieve high velocities and precise orbital maneuvers. In this research, we propose using an elementary space variant diffractive film to design passively stable light sails propelled by laser radiation. We also explore applying this concept to solar sails, enabling spiral trajectories and high orbital inclination angles at close solar orbits.

Our focus is on a 'bi-grating' light sail, designed for stable 'beam-riding' on a Gaussian laser beam. This concept aligns with the Breakthrough Starshot program, aiming to propel an ultra-lightweight sail to a nearby star at relativistic speeds. We analyze stability conditions and evaluate 2D and 3D configurations. To ensure realistic designs, we develop a framework that optimizes electromagnetic simulations using MEEP software, considering stable dynamics. Furthermore, our framework extends to the design and optimization of solar sails, maximizing transverse force efficiency across a broad solar spectrum. Leveraging advanced multi-objective optimization techniques, we create a solar sail with the highest force and lowest mass for maximum acceleration. Through this research, we contribute insights into the design and optimization of light and solar sails, advancing propulsion technologies and pushing the boundaries of space exploration.

Dedicated To

My parents, family & friends

Provide ships or sails adapted to the heavenly breezes, and there will be some who will brave even that void.

Johannes Kepler (1608)

Contents

Chapter 1

Introduction

Year: 1974. Location: Somewhere between Mercury and Venus. NASA's Mariner 10 - the first spacecraft to study Mercury - is running very low on propellant, because of some unplanned maneuvers after launch. If a workaround is not found quickly, the spacecraft will miss Mercury altogether. And this is when "Radiation Pressure" came to the rescue as the engineers decided to use the solar panels of the probe to use the sun, just like a sailboat uses wind - even though it was not part of the original mission design. Thus demonstrating for the first time that navigating in space is possible with radiation pressure alone. Instead of the sun, this work relies on radiation coming in from a laser, and spacecraft is called a Light Sail - a concept that has been around for more than a century but now, as we will see, it is within our current technological reach.

1.1 Early Optimism

Solar Sailing was first written about by Johannes Kepler in 1610, who thought a sail in space might capture sunlight just like a boat catches the wind. Kepler did not fully understand its mechanism of it. It was later in 1873 theorized by Scottish physicist James Clerk Maxwell, who mathematically demonstrated the momentum carried by electromagnetic waves may generate pressure on objects. While science fictions authors, most notably the French authors Faure and Graffigny was busy writing novels about spaceships propelled by giant mirrors in 1889, it was only in 1900 when the force from light was first measured by Peter Lebedew, followed by an articulation of a practical solar sail by the Soviet father of astronautics Konstantin

Figure 1.1: Konstantin Tsiolkovsky (1857-1935) - Soviet Father of Astronautics

Tsiolkovsky, and his co-worker, Fridrickh Tsander in 1920s. The work remained dormant for almost 30 years until Richard Garwin, in 1958, at IBM Watson laboratory of Columbia University authored the first technical paper on solar sail in the journal *Jet Propulsion* and coined the term "solar sailing".

1.2   Laser-driven Light Sails

One of the many reasons that solar radiation pressure may not be useful for interstellar travel is the inverse square variation of solar radiation pressure with heliocentric distance. Many ideas using fission, fusion, nuclear-weapon driven, fusion using collected interstellar protons, and even anti-matter based propulsion and warp-drives have been proposed to overcome this challenge [2, 11, 23, 26]. But these ideas lack
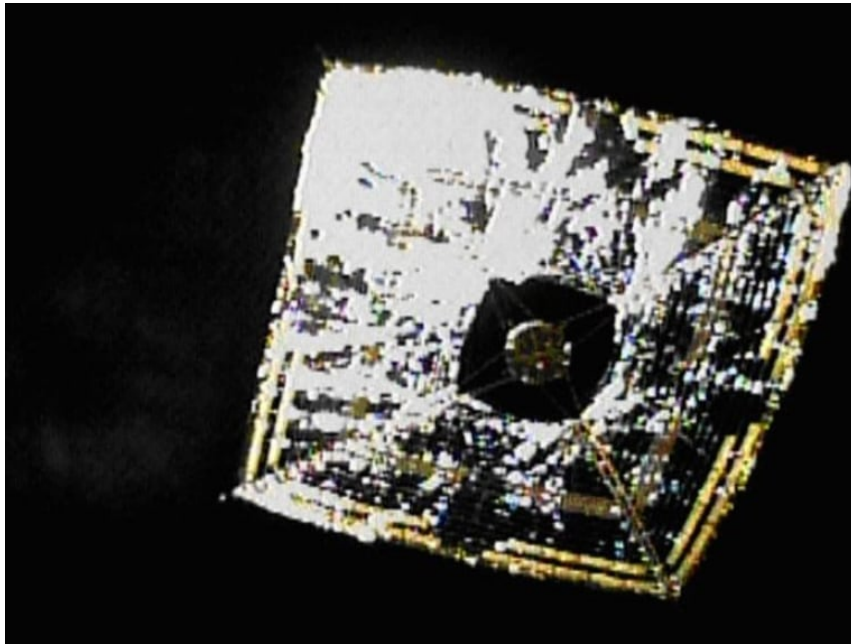
Figure 1.2: IKAROS - First successful solar sail

practicality and some of them lack even fundamental understanding.

Photon propulsion i.e., transporting momentum to a light sail using a collimated beam of light from a space-based laser - a method first proposed by physicist Robert Forward [27] is one of the ideas that is no longer a fantasy. Recent advancements in directed energy technology [31] have a profound impact on many areas of science including photon propulsion. Though difficult, it is within our technological reach to send a miniature probe to the nearest star Alpha Centauri within our lifetime using laser-based propulsion - an ambitious goal of the Breakthrough Starshot program [10].

The main benefit of laser-driven sail over conventional chemical engines is the source of the motive force is fixed, while the sail with payload is accelerated. Thus, laser, the main component of the propulsion system remains fixed, which can be maintained and does not add to the mass of the spacecraft. The benefits are offset by the lack of active maneuverability once accelerated. Thus either a hybrid or passive system is desirable.

Figure 1.3: An artistic representation of the concept of Breakthrough Starshot.

1.3   Challenges of Laser-driven Light Sails

While there exists a vast body of work on solar sail and light sail, the obvious fact is none of it has led to an actual flight of a light sail. Since, 2010 there have been many successful demonstrations of solar sailing, for example, IKAROS (Interplanetary Kite-craft Accelerated by Radiation of the Sun) by JAXA, NASA, and Planetary Society, that has revived the enthusiasm in light sailing and inspired programs like Breakthrough Startshot Initiative [10].

Breakthrough Starshot Initiative aims at designing a gram-scale 100 atoms thick ultralight light sail that will carry the "StarChip" or payload that contains an array of electronics and sensors to gather data from Proxima Centauri b — an exoplanet within the habitable zone of Proxima Centauri and 4.2 light-years away from Earth — in approximately 20 years. The nanocraft will reach a relativistic speed of 60,000 km/s (20% the speed of light) using radiation pressure from a high-powered phased array of lasers on Earth (10 GW/m^2 of net laser intensity), capable of continuous-wave power generation at the 50–70 GW level for an impulse of approximately 1,000-second duration. The laser is very likely a phase-locked optically dense phased array

of individual kW-scale solid-state diode laser amplifiers. Since this work focuses on the light sail, we skip the design challenges associated with laser and identify the following challenges of designing a light sail [4]:

1.3.1 Choice of Materials

Since the sail is propelled by photon momentum transfer, a sail with low mass density, low absorption coefficient, and sufficiently high refractive index contrast is desirable. As for the wavelength, a near-IR window of 1-2 μm may be targeted considering atmospheric transparency. Thus, semiconducting materials with a high refractive index and sub-band energies near-IR may seem like a good fit. However, semiconducting materials also tend to have a higher mass density. It is difficult to find a material that satisfies all three criteria. Materials like c-Si, a-Si, diamond, MoS_2 satisfy at least two of the three criteria and may be considered.

1.3.2 Photonic Design

As the sail accelerates to the target velocity ($v_f = 0.2c$), the incident wavelength is redshifted due to Doppler Effect ($\lambda_f = 1.22\lambda_0$), the immediate implication of which is the sail should have high average reflectance in the range $[\lambda_0, 1.22\lambda_0]$. Nonlinear optimization of structures like slab, multilayer stacks, photonic crystal pillars/holes must be performed to maximize the average reflectance. However, maximizing reflectance alone will render structures with a large mass per area. A more appropriate figure of merit may be total traveled distance (D) to reach the desired velocity (v_f) during the acceleration phase, approximated by

$$D(v_f) \sim \left(\frac{c}{2IA}\right) \int_0^{v_f} \frac{m_t}{R(v)} \frac{\gamma(v)v}{\left(1 - \frac{v}{c}\right)^2} dv \tag{1.1}$$

where $m_t = m_{sail} + m_{payload}$, $R(v)$ is the instantaneous reflectance of the sail for Doppler shifted light, A is the area of sail, I is the laser intensity and $\gamma(v)$ is the Lorentz factor. Eventually, an ideal optimization will take into account multiple figures of merit, for example, stability, tensile stress distribution and off-normal incident light and even damage tolerance due to interplanetary dust.

1.3.3 Thermal Management

The ultra-thin light sail is expected to reach 500-1500K temperature, which may be catastrophic. Thus, the sail is required to manage absorptivity on the illuminated side and emissivity on the dark side of the sail simultaneously to achieve successful thermal management. As the light sail is expected to cool radiatively, the equilibrium temperature during illumination will strongly depend on its emissivity. One of the possible solutions is to use defect engineering to generate tailored materials with elevated inherent emissivity in mid-IR and low absorption in the laser illumination band. Another possible solution is to use low-index materials such as aerogels, that offer better stability and reflectivity. However, very limited data is available for candidate materials in that temperature range. A systematic effort of engineering and measuring thermal properties for samples ¡100 nm is stressed so that a new class of ultrahigh quality ultralow absorption materials can be designed.

1.3.4 Design for Stability

An ideal laser-propelled sailcraft will not only maximize the acceleration and minimize the heating, but also passively stabilize itself with respect to the beam. A stable sail-beam configuration will require either (a) a bi-grating or spherical sail that is immune to non-uniformity in illumination over a large 10 m^2 area or (b) tailoring the laser beam intensity to artificially create intensity minima and trap the sail (like a doughnut-shaped beam). Thus, a holistic system design considering factors like laser beam profile, payload, sail shape, Reflectance, and Absorptivity must be performed. All of these parameters are to be optimized simultaneously and the development of high-performance computing tools is desirable.

1.3.5 Fabrication and Integration

Due to extreme constraints on mass, the sail is very likely to be in form of an ultra-thin film/membrane. Potential materials like Si may be deposited on a few nanometers thick sheet of glass that will act as an excellent low-index spacer and cladding. Fusion-drawn glass sheets have a thickness in the range of 10-50 μm and much more research and investigation is required to reduce the thickness of glass sheets. In addition to the aforementioned challenge, producing and integrating smaller structures to form a uniform high-quality sail of size 10 m^2 is still a critical issue. One of the possible solutions is to fabricate smaller tiles that can be stitched

together to form the final sail. Wafer bonding, aerogel grid/mesh, carbon nanotubes are some useful techniques, however, an investigation of these solutions with respect to defect and stress at the joint is desired.

Chapter 2

The Beam-Riding Problem

As discussed in previous chapter, there are numerous challenges related laser propelled sailcraft that remain unsolved. Amongst those problem, the one which is of particular interest and also the focus of this work is keeping the sail centered with respect to the beam, despite miaslignment, perturbations, and even fabrication imperfections. Ideally, the sail should be passively stable and be able to center itself without seeking any active feedback from actuators i.e., a beam-rider. A close analogy would be a pendulum that tends to come back to its equilibrium point when perturbed and continues to oscillate in the absence of any damping force. In the following sections, we will describe the beam-riding problem and problems with existing solutions.

2.1 Possible Beam-Riding Configurations

2.1.1 Optical Tweezers

Single-beam gradient force trap, popularly known as Optical Tweezers, were originally invented by Arthur Ashkin in 1970 [3], who even got a Nobel Prize in Physics for the same in 2018. Since then, we have been able to exploit both linear and angular momenta of light to bind, trap, cool, sort, and transport particles with applications in biology to microfluidics. However, the particles manipulated using optical tweezers are micron sized or even smaller (see Fig.2.1 . Whereas the Light Sail under study is meter scale object and can not be manipulated using conventional optical manipulation techniques.
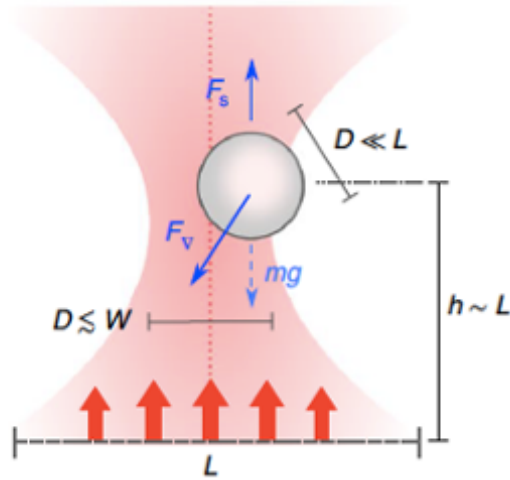
Figure 2.1: Trapping and manipulating a microscopic scale particle using single beam gradient force trap. (Picture credit [5])

2.1.2   Conical Mirror Sail

Conventionally, the go-to choice of a light sail has always been a flat mirror. In principle, the flat mirror with unity reflection will produce maximum thrust along the beam axis. In practice, however, there is a lack of stability if the mirror is perturbed from the equilibrium point, and the sail kicked out of the beam rendering an unstable sail (see Fig.2.2(a)).

Although, the stability of laser propelled sail has not been extensively studied, we may seek some inspiration from numerical simulations and experiments on microwave propelled sails [50, 13, 7, 6]. All of these solutions assume a conical sail with a payload attached to it, like the one shown in Fig.2.2(b). The payload is attached to the sail by means of a boom. A rigorous theoretical analysis of the stability of a reflective conical sail was also performed and its dependence on the boom length was shown [41]. The authors have also demonstrated, by theoretical means, it is almost impossible for a spinning conical reflective sail to accomplish beam-riding. Similar to a conical sail, a spherically curved sail was also proposed [47], that also depends on a boom length such that the sail is stable when the distance from the Lightsail center to the center of mass is larger than the radius of curvature.
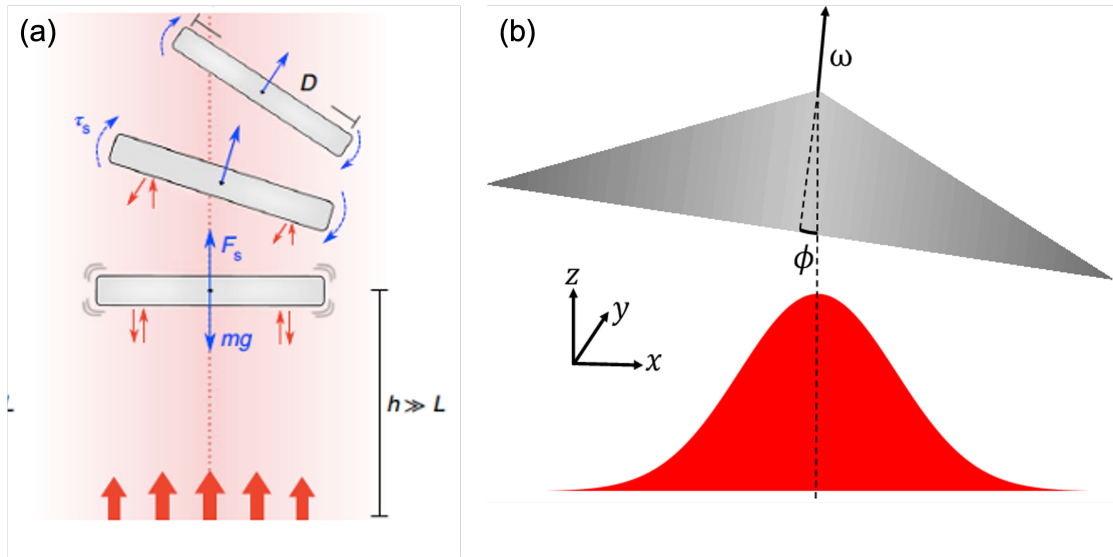
Figure 2.2: (a) A flat mirror sailcraft is unstable because of lack of forces parallel to the mirror (b) a conical mirror introduces transverse component of forces that may result in a stable sail. (Picture credit [41, 5])

2.1.3   Spherical Sail

In order to overcome the challenges of a reflective conical sail due to coupling in translational and rotational degrees of freedom, the authors in [41] proposed a spherical shell sail whose symmetry eliminates such coupling, shown in Fig.2.3. In order to "trap" the sail and keep it stable, the authors rely on a multi-modal Gaussian beam with deeper potential well. Please note, the aforementioned solutions assume a rigid sail that will keep its cone angle/spherical shell shape intact. While in practice, the sail may billow this and possess structural modes.

2.2   Formulation of Problem with ODEs

In Physics, modelling a problem is just solving an initial value problem i.e., an Ordinary Differential Equation (ODE) with an initial condition that specifies the value of unknown function at a given point in the domain like time or space. In the context of light sail, the dynamically changing force and torque may be described in
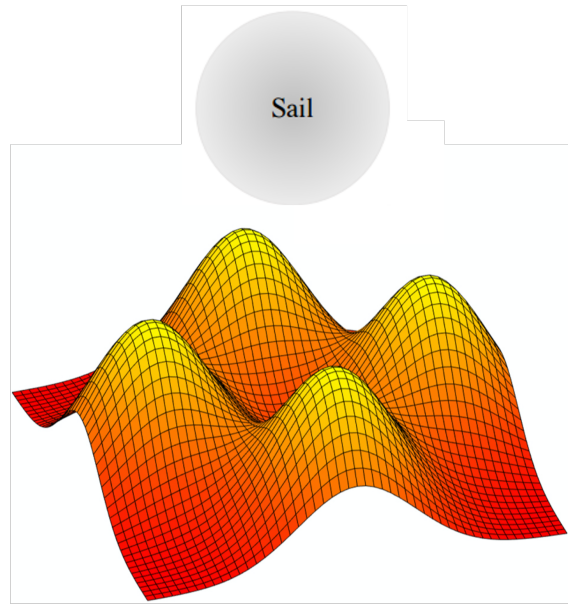
Figure 2.3: The sail eliminates rotational and translational coupling using symmetry and gets trapped in the potential well of a multi-modal beam (Picture credit [41])

terms of one or more ODEs. In the following section, we will look into linearizing a system and solving them in MATLAB.

2.2.1 Linear Stability Analysis of ODEs

A dynamical system may be modeled by a finite number of coupled ODEs written in form of a state equation:

$$\dot{x} = f(t, x, u) \tag{2.1}$$

where x is an n-dimensional state vector, t is the time and u is the input. A special case of Eq.2.1 arises when f does not depend on time and is called *autonomous*. The point x^* in state space is called an equilibrium point if the system starts at x^* and remains at x^*. For an autonomous system, x^* is root of the equation

$$f(x) = 0 \tag{2.2}$$

More often than not, a common practice is to linearize a non-linear system to learn as much as possible about the non-linear system. Since, the equilibria x^* may or

may not be stable, it is useful to classify equilibrium points based on their stability.

If the components of the state vector x are $(x_1, x_2, ...x_n)$ and the compoents of the rate vector f are $(f_1, f_2, ...f_n)$, then the Jacobian is

$$J = \begin{bmatrix} \frac{\partial f_1}{\partial x_1} & \frac{\partial f_1}{\partial x_2} & \cdots & \frac{\partial f_1}{\partial x_n} \\ \frac{\partial f_2}{\partial x_1} & \frac{\partial f_2}{\partial x_2} & & \frac{\partial f_2}{\partial x_n} \\ \vdots & \vdots & & \vdots \\ \frac{\partial f_n}{\partial x_1} & \frac{\partial f_n}{\partial x_2} & \cdots & \frac{\partial f_n}{\partial x_n} \end{bmatrix} \tag{2.3}$$

where the Eq.2.3 is obtained by taking a multivariate Taylor expansion of the Eq.2.1 assuming an autonomous system. We now define $\delta x = x - x^*$ such that $\dot{\delta x} = \dot{x}$. For small enough δx, the autonomaous form of Eq.2.1 may be expressed

$$\dot{\delta x} = J^* \delta x \tag{2.4}$$

where J^* is the Jacobian evaluated at equilibrium point. Eq.2.4 is just a linear differential equation since the matrix J^* is a constant. Thus, a solution can be written as a superposition of the terms $e^{\lambda_j t} = e^{\mu_j t + i v_j t}$ where $\lambda_j = \mu_j + i v_j$ are the eigenvalues of the Jacobian. The complex part of the eigenvalue v_j suggests an oscillating behaviour of the solution, it is the real part μ_j that determines if the trajectories will move away or converge to the equilibrium point. In other words, an equilibrium point x^* is *stable* if all the values of eigenvalues of J^* evaluated at x^* have negative real part. The equilibrium point is *unstable* if at least one of the eigenvalues have positive real part. An analysis based on this approach is called *linear stability analysis*. Based on whether the eigenvalues are real, complex, positive or negative, the nature of stability can be concluded and is summarized in Fig.2.4 along with the corresponding phase space diagram.

Clearly it becomes difficult to analyze a system with at least one eigenvalue with real part zero and this case can't be decided based on linear stability analysis alone. However, linearization has its own limitation and can only be used in the neighborhood of an operating point like equilibrium point predicting a "non-local" behaviour. Also, there are phenomena that only occurs in the presence of nonlinearity and can not be described by linear models, for example, subharmonic or almost-periodic oscillations, limit-cycles chaos, and multiple modes of behaviour [36].

To determine stability far from equilibrium point, a technique developed by Lyapunov may be employed [36]. Suppose $V(x)$ is a function of state variable x which has a minimum at an equilibrium point but no local minima. If we can show that

Node		Proper Node
Two distinct real eigenvalues, same sign		Repeated real eigenvalue two eigenvectors
UNSTABLE		UNSTABLE if positive
If both eigenvalues are positive		ASYMPTOTICALLY STABLE
ASYMPTOTICALLY STABLE		If negative
If both are negative		
	I	II
Saddle Point		Center
		Complex eigenvalues
Two distinct real eigenvalues, opposite signs		Purely IMAGINARY (real part = 0)
		STABLE,
		or "NEUTRALLY STABLE "
Always UNSTABLE		Not asymptotically stable
	III	IV
Spiral Point		Improper Node
Complex eigenvalues, w/ Non-zero real part		Repeated real eigenvalue one eigenvector only
UNSTABLE		UNSTABLE
If real part is positive		If positive
ASYMPTOTICALLY STABLE		ASYMPTOTICALLY STABLE
If real part is negative		If negative
	V	VI

Figure 2.4: Phase diagrams and corresponding eigenvalues of a dynamical system.

the dynamics of the system results in some neighbourhood of the equilibrium point results in a steady decrease in V, it implies we are tending towards the minimum of V and we can conclude that the equilibrium point is stable in the entire neighborhood of x^* over which V decreases. Such a function V is called *Lyapunov function*. The idea of Lyapunov function may be formalized as follows:

"Let U be the region of space containing an equilibrium point x^* and V is a positive definite function for this point if it satisfies two conditions: $V(x^*) = 0$, and $V(x) > 0$ for $x \in U - x^*$, then the equilibrium point is asymptotically stable if for initial conditions in the neighborhood of U if $\dot{V}(x) < 0$ for all $x \in U - x^*$."

Unfortunately, it is really difficult to come up with a Lyapunov function except in some special cases where the physics of the problem suggests a particular choice.

2.2.2   Solving ODEs in MATLAB

ODEs may only be solved explicitly in terms of integrals and functions only for simpler cases. For practical purposes, an approximate solution is sufficient and is calculated by means of numerical integration. Since, this work is largely based on calculating the trajectory of sailcraft with time in MATLAB, it is important to understand the ODE solvers available to us and their limitations.

In total, there are 8 ODE initial value problem solvers in MATLAB: `ode45, ode23, ode113, ode15s, ode23s, ode23t, ode23tb, ode15i`. Please note, `ode15i` is not the part of this discussion because it solves its own class of fully implicit initial value ODEs. The ODE solvers in MATLAB work on problems of the form

$$M(t,y)y' = f(t,y) \tag{2.5}$$

where $y' = dy/dt$ and $M(t,y)$ is called *mass matrix*. Depending on the chosen solvers algorithm, a solution is calculated iteratively by using solutions from previous step, using an initial value y_0 provided at t_0 in the given range of time (t_0, t_f). The final result is a vector of solutions $y_0, y_1, ... y_f$ corresponding to $t_0, t_1, ... t_f$. These algorithm are based on fundamental theorem of calculus:

$$y(t + h) = y(t) + \int_t^{t+h} f(s, y(s)) ds \tag{2.6}$$

i.e., where h is the step size and the integration on right hand side is approximated by the solvers algorithm. There exists various schemes to solve these integrals numerically and a given algorithm makes a trade-off between accuracy and efficiency. For example, a given solver may take smaller and smaller step-size h for accuracy but loses on efficiency and speed. Sophisticated ODE solvers like in MATLAB are either *single-step* (like `ode45`) or *multi-step* (like `ode113`) solvers i.e., they either use the results from a single previous step or several past steps. What's more, instead of using a fixed step size, these solvers estimate the error in each step to determine the step size of next iteration. MATLAB's naming convention allows a user to determine how the error in each step is caclulated: `odeMN` solver compares the results of Mth-order and N^{th}-order Runge-Kutta method.

Some ODEs are stubborn and not easily evaluated using numerical technique such that the algorithm is forced to take a step-size down to an unreasonably small value causing either the integration to fail or take a lot of time to solve. Such ODEs are known as *stiff*. *Stiffness* is hard to define since it may be a result of a variety of reasons, for example, a mathematically stable problem may become stiff if its Jacobian $J = \partial f_n / \partial y_i$ has a large ratio of negative eigenvalues constraining the step-size. However, some of the ODE solvers are designed to work on stiff ODEs and perform more work per step and hence less efficient. It is important to remember, non-stiff solvers can work on stiff ODEs though for a low efficiency. Similarly, stiff solvers can work on non-stiff ODEs at the price of low speed because they are doing extra work in each step which is not really required. Thus, the goal here is to strike a right balance between accuracy and efficiency of the solver. Please note, stiffness is a complex topic and this discussion is only cursory in nature. For an in-depth look, please see [38]. In most of the cases, either `ode45` or `ode15s` will suffice for non-stiff and stiff problems respectively. As a general rule:

- `ode45` is the first ODE solver you should chose to begin with.

- Use `ode113` for orbital and celestial mechanics problem where high precision is required.

- For mildly stiff problems and the problems that permit crude error tolerances, try using `ode23`.

- In case of singular mass matrix or if `ode45` fails to integrate, use `ode15s`.

- Use `ode23s` if the problem is stiff and the Jacobian is available.

Chapter 3

Bi-Grating Beam-Rider

For nearly a century, the law of reflection is assumed to be the only mechanism of transfer of momentum from electromagnetic field to the light sail. While a reflective film offers maximum force normal to the film (assuming the incident beam is at 0°), it offers no force whatsoever parallel to it. Curved reflective film may offer dynamic stability owing to transverse component of forces normal the surface, only if a few atomic layer thick film can maintain such curvature. What's more, the reflective films are metallic and will absorb heat and may not withstand a GW laser. In the following section, we will explore how a space-variant diffractive film may be used as a passively stable sailcraft.

3.1 Bi-Grating Sail Design

To demonstrate the fundamental design principles, the bi-grating sail is reduced to two-dimensional configuration is shown in Figure 3.1. The sail accelerates along the beam axis and is free to rotate about an axis passing through the center of mass. Thus, the sail in this configuration has 3 degrees of freedom.Since, the laser is fixed and the sail is accelerating, it is convenient to consider two frames of references: $(\hat{x}, \hat{z})$ for laser and $(\hat{n}, \hat{p})$ for the sailcraft.

The bi-grating is composed of two diffraction grating panels (A and B) of length L that diffracts light in opposite direction and towards the optical axis owing to opposite diffraction order. The incident laser of power P_0 has a wavelength λ and a characteristic width of $2w_0$. The beam propagates with wave vector $\vec{k}_i = (2\pi/\lambda)\hat{z}$ along $\hat{z}$. The lightsail is assumed to be rigid with total mass $M = M_s + M_p + M_b$,
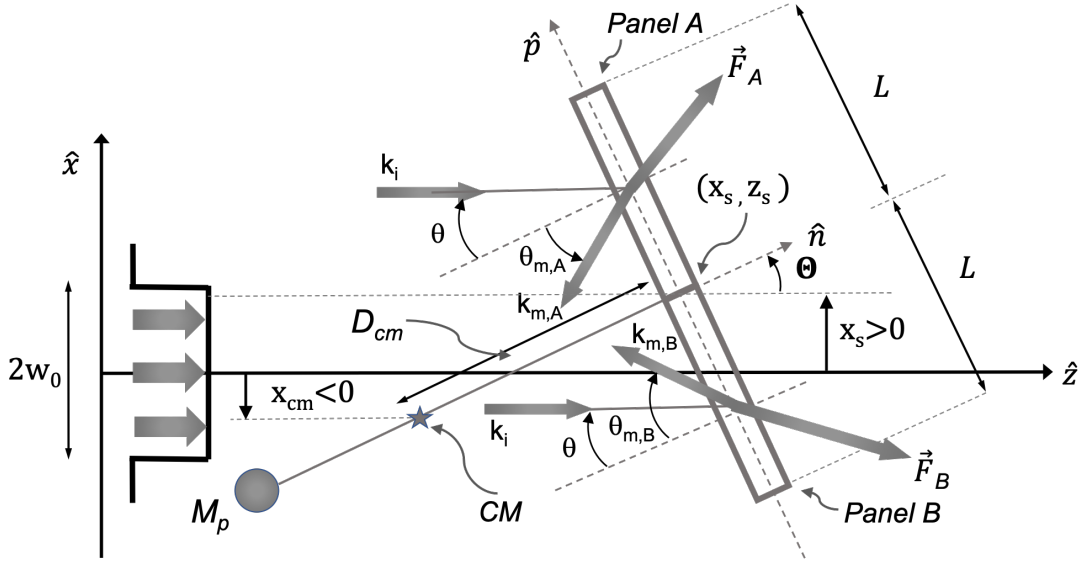
Figure 3.1: A beam of full-width $2w_0$ is incident from the left on a sail composed of two diffractive panels A and B, each of length L. A payload of mass M_p is attached to the sail by a boom of length D_b and mass M_b. Sail displacement and attitude with respect to the beam axis: x_s and Θ. Forces on each panel are shown as F_A and F_B. Incident and diffracted wave vectors, $\vec{k}_i$, $\vec{k}_{m_A}$, $\vec{k}_{m_B}$.

where M_s, M_p, and Mb are the mass of sail, payload and the boom respectively. $D_b > 0$ if the payload is on the illuminated side of the sail. The center of mass of the sailcraft and the bi-grating sail is shown as (x_{cm}, y_{cm}) and (x_s, z_s) respectively. The attitude of the sail is measured with respect to the optical axis is denoted by Θ (measured counterclockwise) and the clockwise optical angle of incidence θ is measured from the sail normal, with angular unit vectors $\hat{\theta} = -\hat{\Theta}$.

The grating panels are assumed to have same grating period Λ and diffracts the beam into a single diffraction order at angles $\theta_{m_{A,B}}$ with unity efficiency [24, 29, 49] as per the grating equation

$$\sin\theta_{m_{A,B}} = m_{A,B}\lambda/\Lambda - \sin\theta \tag{3.1}$$

where equal and opposite values of grating orders are assumed: $m_B = -m_A$. As shown below, the system may be stable to small perturbations when m_A is a negative integer. A laser has a Gaussian irradiance distribution along the bi-grating surface

$$I_g(p) = \frac{P_0}{2{\rm w_0}^2\sqrt{\pi/2}} \cos\Theta \, \exp\left(-2\frac{(p\cos\Theta + x_s)^2}{{\rm w_0}^2}\right) \tag{3.2}$$

where P_0 is the peak power and where $p = (x - x_s)/\cos\Theta$. In an attempt to simplify our analysis and derive an analytical solution, we assume a square/flat-top beam cross-section of full-width $2{\rm w_0}$. The distribution of irradiance along the bi-grating surface may now be expressed

$$I_f(p) = (P_0/4{\rm w_0}^2)\cos\Theta \, \mathrm{rect}\left((p\cos\Theta + x_s)/{\rm w_0}\right) \tag{3.3}$$

where $\mathrm{rect}(s)$ has a value of unity (zero) if $|s| < 1$ ($|s| > 1$). The power on each panel may be determined from convolution integral of the panel distribution: $P_A = 2{\rm w_0}\int_0^L I(p)dp$ and $P_B = 2{\rm w_0}\int_{-L}^0 I(p)dp$ and Eq.3.3 (or Eq.3.2). The distribution of power with respect to displacement x_s/L of the bi-grating sail center are plotted in Fig.3.2 for a flat-top and a Gaussian irradiance distribution, both having a characteristic full-width $2{\rm w_0} = L$.

3.2 Linear Stability Analysis

For displacements such that $|x_s| < {\rm w_0}$, the relative power $P_{A,B}/P_0$ on one panel increases linearly with x_s while it decreases linearly on the other panel. Also it stays nearly invariant for small angles. Thus, for a flat-top beam of full-width $2{\rm w_0} < 2L$,

$$P_{A,B} = (P_0/2{\rm w_0})({\rm w_0} \mp x_s) \ , \quad |x_s| < {\rm w_0} \tag{3.4}$$

where the minus (plus) sign corresponds to Panel-A(B). The forces on each panel may be expressed [56]

$$\vec{F}_{A,B} = F_{A,B}^{(p)}\hat{p} + F_{A,B}^{(n)}\hat{n} = (P_{A,B}/c)(-\kappa_{A,B}\hat{p} + \Gamma_{A,B}\hat{n}) \tag{3.5}$$

where the plus (minus) sign corresponds to Panel-B(A). The forces on each panel may be expressed [56]

$$\vec{F}_{A,B} = F_{A,B}^{(p)}\hat{p} + F_{A,B}^{(n)}\hat{n} = (P_{A,B}/c)(-\kappa_{A,B}\hat{p} + \Gamma_{A,B}\hat{n}) \tag{3.6}$$

where c is the speed of light, $\Gamma_{A,B} = \cos\theta + \cos\theta_{m_{A,B}}$, $\cos\theta_{m_{A,B}} = \pm(1 - \sin^2\theta_{m_{A,B}})^{1/2}$ where the minus (plus) sign corresponds to a transmissive (reflective) grating and
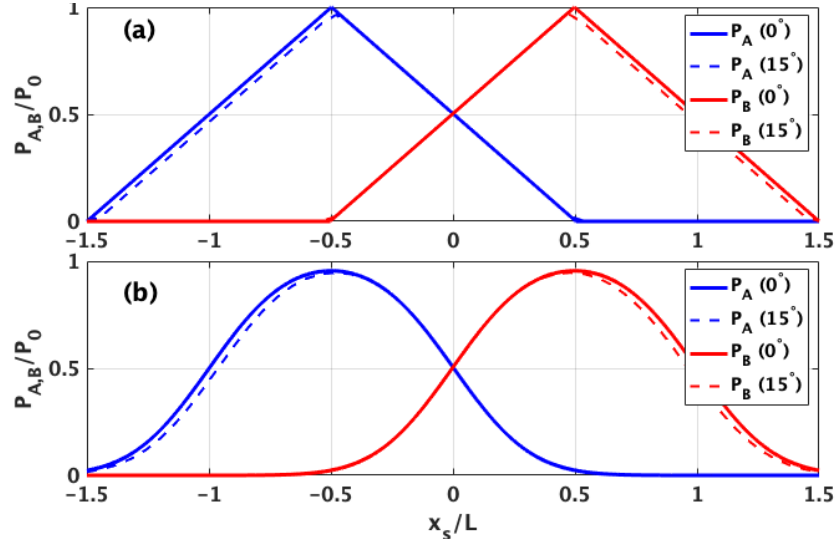
Figure 3.2: Relative power on panels A, B as a function of sail displacement x_s/L for (a) flat-top and (b) Gaussian beams of full-width $2w_0 = L$. Power is nearly invariant for $\Theta << 1$ rad.

$$\kappa_{A,B} = m_{A,B}\lambda/\Lambda \tag{3.7}$$

The torques about the center of mass may be expressed

$$\vec{N}_A = \frac{2w_0}{c}\int_0^L I(p)dp\,(D_{cm}\hat{n} + p\hat{p}) \times (-\kappa_A\hat{p} + \Gamma_A\hat{n}) \tag{3.8a}$$

$$\vec{N}_B = \frac{2w_0}{c}\int_{-L}^0 I(p)dp\,(D_{cm}\hat{n} + p\hat{p}) \times (-\kappa_B\hat{p} + \Gamma_B\hat{n}) \tag{3.8b}$$

where D_{cm} is the distance from the center of mass to point (x_s, z_s). For small relative displacements with $|x_s| < w_0$, we find

$$\vec{N}_{A,B} = \frac{P_0}{2w_0c}(w_0 \mp x_s)\left[-D_{cm}\kappa_{A,B} \mp \frac{(w_0 \mp x_s)\Gamma_{A,B}}{2\cos\Theta}\right]\hat{y} \tag{3.9}$$

The rotational equation of motion about the center of mass may be expressed

$$\vec{N} = (\vec{N}_A + \vec{N}_B)\,\hat{y} = J\ddot{\Theta}\,\hat{y} \tag{3.10}$$

where $\hat{y} = \hat{n} \times \hat{p} = \hat{z} \times \hat{x}$, $J = J_s + J_p + J_b = MR_g^2$ is the total moment of inertia of sailcraft about the center of mass, J_s, J_p, and J_b are the moment of inertia of sail, payload, and boom about the center of mass respectively , R_g is the radius of gyration, and $M = M_s + M_p + M_b$ is the total mass of sailcraft. For analytical convenience we assume $M_s = M_p$ such that $D_{cm} = D_b/2$ and $J = M_s L^2/3 + (M_s + M_p)D_b^2/4 + M_b D_b^2/12$. The translational equations of motion of the sail in the laboratory reference frame may then be expressed

$$F_z = M\ddot{z}_s = (F_A^n + F_B^n)\cos\Theta - (F_A^p + F_B^p)\sin\Theta \tag{3.11a}$$

$$F_x = M\ddot{x}_s = (F_A^p + F_B^p)\cos\Theta + (F_A^n + F_B^n)\sin\Theta \tag{3.11b}$$

For small perturbations near equilibrium ($x_s = 0$, $\Theta = 0$) the equations of motion (Eq.s 3.10, 3.11) may be linearized

$$\ddot{z}_s = \alpha - K_1 \Theta x_s \tag{3.12a}$$

$$\ddot{x}_s = K_1 x_s + K_2 \Theta \tag{3.12b}$$

$$\ddot{\Theta} = K_3 x_s + K_4 \Theta \tag{3.12c}$$

where

$$\alpha = P_0(1 + \sqrt{1 - \kappa_A^2})/Mc \tag{3.13a}$$

$$K_1 = P_0 \kappa_A / Mc\mathrm{w}_0 \tag{3.13b}$$

$$K_2 = P_0(1 + \sqrt{1 - \kappa_A^2})/Mc \tag{3.13c}$$

$$K_3 = P_0 D_b \kappa_A / 2\mathrm{w}_0 Jc + MK_2/J \tag{3.13d}$$

where $K_4 = 0$. From Eq.s 3.12a and 3.16a we find the sail uniformly accelerates along the beam path when both $0 < \kappa_A^2 < 1$ and $|x_s\Theta| << L$. To achieve a Hooke's law type restoring force that depends on the displacement x_s it is evident from Eq.s 3.7, 3.12b and 3.16b that $\kappa_A < 0$, and thus the diffraction order $m_A < 0$. As stated previously, the panels are designed to diffract into equal and opposite grating orders, and thus $m_B = -m_A > 0$. Setting $K_3 = 0$ in Eq.3.16d we find a critical value for the boom length:

$$D_{cr} = -2\mathrm{w}_0(1 + \sqrt{1 - \kappa_A^2})/\kappa_A \tag{3.14}$$

Having established that $\kappa_A < 0$ we find $D_{cr} > 0$, and thus, the payload must be placed on the illuminated side of the sail. We note that D_{cr} is a function of
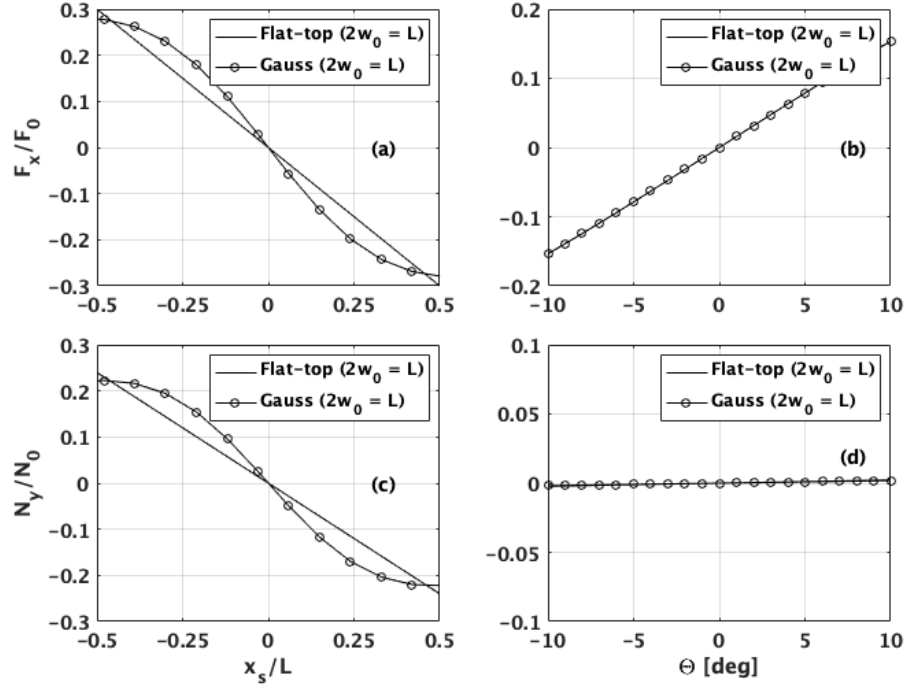
Figure 3.3: (a) Transverse force F_x and (b) torque N_y as a function of angle Θ and transverse displacement x_s owing to radiation pressure from a (top) flat-top and (bottom) Gaussian beam profile of power P_0. Normalization: $F_0 = 2P_0/c$ and $N_0 = F_0 D_b/2$ where c is the speed of light and D_b is the boom length. System parameters are listed in Table 1.

beam width and thus the boom length $D_b > D_{cr}$ must be selected according to the anticipated beam spread over the acceleration phase of the lightsail, during which time the beam may expand owing to diffraction.

To determine whether Eq.s 3.12b and 3.12c allows stable oscillations, we calculate the eigenvalues [35]:

$$\epsilon_{1,2} = -\omega_0^2 \left[1 \pm \sqrt{1 - \Delta} \right] \tag{3.15}$$

where $\Delta = (D_b/D_{cr} - 1)(D_{cr}/R_g)^2$, and $\omega_0 = \sqrt{-K_1/2} = 2\pi/T_0$ describes the degenerate frequency when $\Delta = 1$. In general, the system will exhibit two stable

Table 3.1: Parameters and values used in numerical model.

Parameters	Value
Panel Length, L	1.0 m
Beam Power, P_0	10 kW
Wavelength, λ	1.0 μm
Grating period, Λ	1.6 μm
Diffraction order, $m_A(m_B)$	$-1(+1)$
Boom Length, D_b	15.0 m
Mass of Sail, M_s	0.50 g
Mass of Boom, M_b	0.17 g
Mass of payload, M_p	0.50 g
Radius of Gyration, R_g	7.13 m
Period, $T_0 = 2\pi/\omega_0$	48.1 s

oscillation frequencies $\omega_{1,2} = \sqrt{-\epsilon_{1,2}}$ when $\epsilon_{1,2}$ is real ($\Delta \leq 1$) and negative.

3.3   Solution to the Equations of Motion

As an example of a stable beam rider, we designed a low mass system with parameters listed in Table 6.1. The force and torque on the sail are shown in Fig.5.4 as a function of x_s and Θ. The slopes of these lines at $x_s = 0$ and $\Theta = 0$ are proportional to the stiffness values:

$$K_1 = (F_0/L)\partial(F_x/F_0)/\partial(x_s/L)|_{x_s=0} \tag{3.16a}$$

$$K_2 = (F_0)\partial(F_x/F_0)/\partial\Theta|_{\Theta=0} \tag{3.16b}$$

$$K_3 = (N_0/L)\partial(N_y/N_0)/\partial(x_s/L)|_{x_s=0} \tag{3.16c}$$

$$K_4 = (N_0)\partial(N_y/N_0)/\partial\Theta|_{\Theta=0} \tag{3.16d}$$

The equations of motion (Eq.s 3.10, 3.11) were numerically integrated by means of a fourth-order Runge-Kutta algorithm for $t = 100T_0$ and longer. Phase diagrams and frequency spectra indicative of stable mechanical oscillations are shown
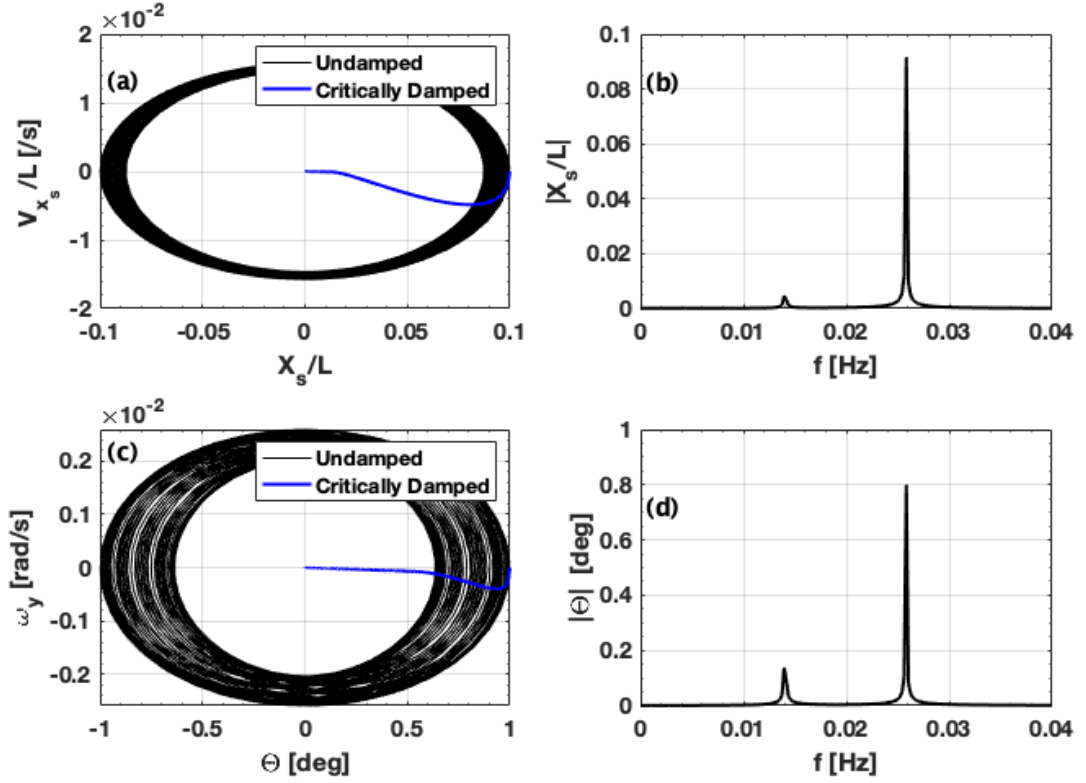
Figure 3.4: Numerical solutions for a flat-top beam with parameters listed in Table 1. (a) Phase plot and (b) frequency spectrum for transverse displacement, x_s. (c) Phase plot and (b) frequency spectrum for attitude Θ. Undamped (solid) and critically damped (solid blue) examples are shown.

in Fig.3.4 for the initial condition (IC) $(x_s, \Theta, \dot{x}_s, \dot{\Theta}) = (0.1L, 1°, 0, 0)$. As expected both the phase diagram for displacement, Fig.3.4(a), and the Fourier transform of $x_s(t)$, Fig.3.4(b), exhibit stable two-frequency dynamics. The same is true for the phase diagram for attitude, Fig.3.4(c), and the Fourier transform of $\Theta(t)$, Fig.3.4(d). The numerically determined oscillation frequencies agree with the predicted values, $f_{1,2} = \omega_{1,2}/2\pi = 0.0141, 0.0258$ Hz to within less than 1%. Numerical values for the respective amplitude and attitude values are $0.0047L$, $0.091L$, $0.1376°$, and $0.800°$.

We expected the undamped system to remain nominally stable for small angles
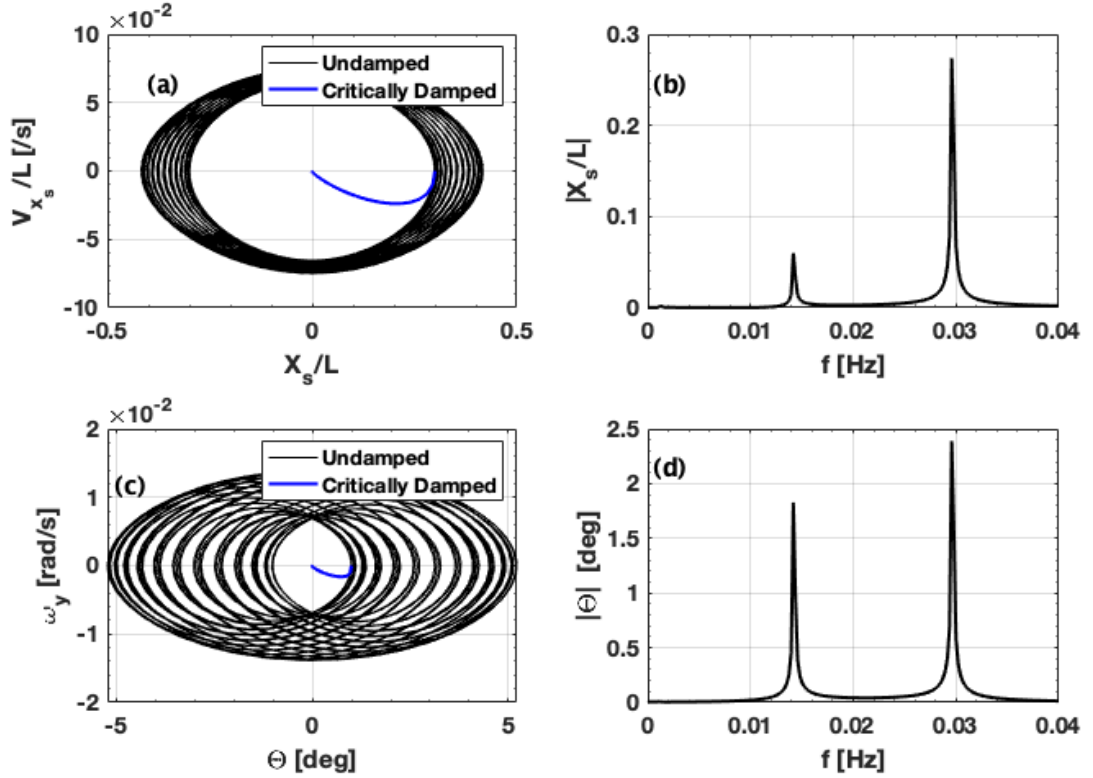
Figure 3.5: Numerical solutions for a Gaussian beam with parameters listed in Table 1. (a) Phase plot and (b) frequency spectrum for transverse displacement, x_s. (c) Phase plot and (b) frequency spectrum for attitude Θ. Undamped (solid) and critically damped (solid blue) examples are shown.

if $|x_s/L| < 0.5$. However, our numerical model reveals a restricted stability range of initial conditions which may be expressed

$$|x_s|/x_{cr} + |\Theta|/\Theta_{cr} < 1 \tag{3.17}$$

where $x_{cr} = 0.34L$, $\Theta_{cr} = 6.0°$, and zero initial transverse and angular velocities have been assumed. We attribute this smaller range of dynamic stability to coupling between the linear and angular degrees of freedom.

A damping mechanism may be expected to improve the lightsail performance by

driving the system toward equilibrium. Common space-qualified dampers include viscous and magnetic induction devices. The introduction of a damping force $-\mu \dot{x}_s$ and torque $-\gamma \dot{\Theta}$ may extend the range of stability and reduce the uncertainty of the lightsail trajectory. As an example, a case of critical damping is depicted in Fig.3.4 (solid blue line) for an initial state $(0.1L, 1°, 0, 0)$ and damping coefficients $\mu = 0.4$ kg/s and $\gamma = 0.9$ kg m^2/rad s. For these damping values our numerical model predicts an extension of stability for $|x_s|$ of $4.4x_{cr}$, i.e., IC: $(1.5L, 0, 0, 0)$, and an extension of stability for $|\Theta|$ of $3.9\Theta_{cr}$ with IC: $(0, 23.6°, 0, 0)$.

From a practical point of view the light beam may have a Gaussian irradiance profile (see Eq.3.2 and Fig.3.2(b)), rather than a flat-top profile. An examination of the dependence of force and torque on displacement and attitude plotted in Fig.5.4, suggests that a linear analysis may be a useful approximation for the Gaussian case, provided $x_s/L < 0.1$. Indeed numerical solutions of the general equations of motion exhibit stable oscillations having two frequencies for a range of initial conditions for a Gaussian beam. Typical phase diagrams and frequency spectra for the system characterized by the parameters in Table 6.1 are shown in Fig.3.5 for IC: $(0.3L, 1°, 0, 0)$. The numerically determined frequencies are 0.0141 Hz and 0.0295 Hz, with respective translation and attitude amplitudes: $0.059L$, $0.273L$, $1.83°$, and $2.39°$. Exploring the range of stability without damping we obtained the values $x_{cr} = 0.36L$ and $\Theta_{cr} = 8.0°$, which are comparable to the values for an undamped lightsail driven by a flat-top beam.

3.4   Summary & Conclusions

In summary we have described the optomechanics of a diffractive beam rider that may be of practical interest to organizations that are developing laser-driven propulsion, navigation, and control concepts. This two-dimensional analysis for flat-top and Gaussian beam profiles may be readily extended to three dimensions and structured light beams. The flat-top case provides tractable analytic solutions that aid the lightsail design process. Stability criteria have been identified that allow small linear and angular displacements with respect to the driving beam (e.g., a laser). Greater stability comes at the expense of less acceleration along the beam path. An example that provides 90% of the theoretical maximum acceleration (see Eq.3.16a) has been described for a system that includes an attached payload on the illuminated side of the sail. Opto-mechanical stability is robust against variations of the

boom length and beam size, provided the length exceeds a threshold value. The broad latitude afforded by space-variant diffraction gratings provides a wide range of alternative stable sailcraft designs. For example electro-optically active gratings [49] may provide a means to guard against center-of-mass and center-of-pressure offsets or to assert attitude control [61]. An advantage of a diffractive sail (fabricated with low absorbing dielectric materials such as oxides or liquid crystal polymers) over a metallized sail is a higher damage threshold and thermal robustness.

A comparison of various reflective and diffractive sailcrafts must account for the intended space mission or application. For example an optimal sail designed to achieve a solar polar orbit will be strikingly different from one designed to reach a solar escape velocity. Extremely large diffractive sails (much greater than 1m^2) comprised of arrays of easily manufactured gratings [49] provide a distinct cost advantage over those using diffractive elements requiring nanometer-scale feature sizes. Sails reaching near-relativistic velocities must account for the Doppler shifted wavelength and reduced irradiance. We find that a 10% redshift seen by the bi-grating sail would increase the mean oscillation frequency by roughly 3.5% owing to the redshifted wavelength alone, but also accounting for the Doppler shifted irradiance, the mean oscillation frequency decreases [34]. Finally, we note that an opto-mechanical bi-grating and variants such as a diffractive (or holographic) axicons may also find terrestrial applications for energy harvesting, mode control in an optical cavity, or the in-aqueous transport of biological tissue.

Chapter 4

Axicon Beam-Rider

This chapter extends our one-dimensional theoretical investigations of a bi-grating to a two-dimensional axicon grating sail. Section 4.1 describes the transfer of momentum from the light beam to the sail, making use of sail and observer reference frames moving at small relative velocities so that the Doppler shifted wavelength may be ignored. The equations of motion for linear and angular degrees of freedom owing to optomechanical force and torque are described in Section 4.2. A linear stability analysis is described in Section 4.3 where conditions for stable light propulsion are described. Numerical solutions of the equations of motion are presented in Section 4.4, including an analysis of motion in the stable regime.

4.1   Photon Momentum Transfer to an Axicon

Let us consider a laser beam of characteristic radial width w incident upon a sail of radius a. Radiation pressure applies a local force at all sail points, resulting is longitudinal acceleration along the optical axis, lateral force, and torque. The minimum beam size, w_0 (the waist) is positioned at the origin of the observer coordinate system (X, Y, Z), as illustrated in Fig. 4.1 and the beam propagates in the Z-direction (the optical axis). The electric field profile of a monochromatic beam of wavelength λ and constant power P may be expressed [51]

$$
\begin{aligned}
E(X, Y, Z) = \sqrt{I_0(Z)} \, (w_0/w(Z)) \, \exp\left(-(X^2 + Y^2)/w(Z)^2\right) \\
\exp\left(i\Phi(r, z)\right) \, \exp\left(i\left(k_Z Z - \omega t\right)\right)
\end{aligned}
\tag{4.1}
$$
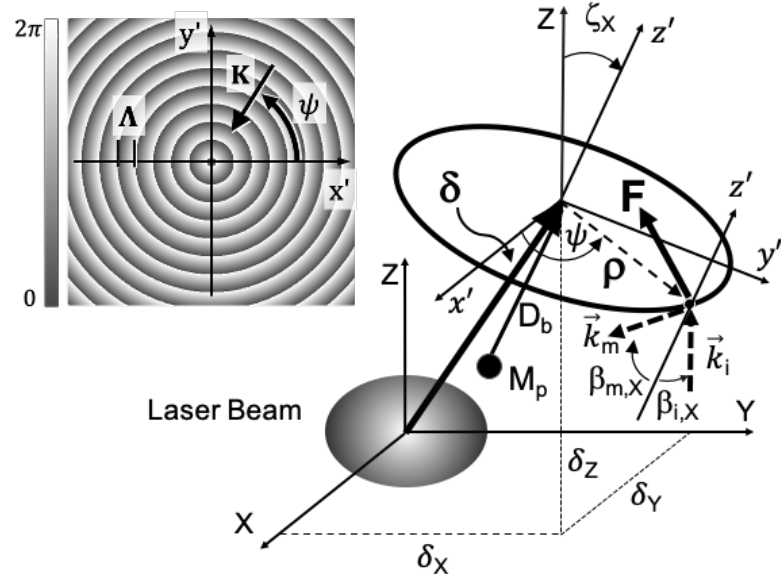
Figure 4.1: Diffractive sail illuminated by a beam at incident angle $\beta_{i,X}$ and diffraction angle $\beta_{m,X}$. Sail tilt axis $\zeta_X = -\beta_{i,X}$. Attached payload of mass M_p with boom length D_b. Laser beam origin $(X, Y, Z) = (0, 0, 0)$. Sail displacement $\vec{\delta}$. Inset: Magnified view of axicon phase with grating vector $\vec{K}$.

where $k_Z = 2\pi/\lambda$, $\omega = ck$ is the angular frequency, c is the speed of light, $I_0(Z) = 2P/\pi w^2(Z)$ is the irradiance on the optical axis, $w(Z) = w_0 [1 + (Z/Z_0)^2]^{1/2}$ is the radial beam size, $Z_0 = \pi w_0^2/\lambda$ is the diffraction length, $\Phi(r, z) = k_z(X^2 + Y^2)/2R(z) - \arctan(Z/Z_0)$, and $R(Z) = Z[1 + (Z_0/Z)^2]$ for a TEM$_{00}$ Gaussian beam. Assuming the beam is much larger than the wavelength ($w_0 >> \lambda$), we ignore the transverse component of the wave vector, $k_X = \partial\Phi/\partial X$ and $k_Y = \partial\Phi/\partial Y$, which are much smaller than k_Z. That is, the paraxial approximation is made such the incident wave vector may be expressed $\vec{k}_i = (2\pi/\lambda)\hat{Z}$.

We consider a sail comprised of a reflection grating that diffracts light toward the sail axis when illuminated at normal incidence. That is, the sail functions as an optical axicon (see inset of Fig. 4.1), having a periodic phase profile, $\Phi_{axicon}(\rho'+\Lambda) = \Phi_{axicon}(\rho') = -2\pi(\rho'/\Lambda)$ where $\rho' = (x'^2 + y'^2)^{1/2}$. For analytical convenience we assume a single diffraction order, noting that this analysis may be readily extended to include multiple reflection and transmission orders. The axicon grating vector $\vec{K}$

lies in the plane of the sail and points radially toward the sail axis (see inset of Fig. 4.1).

The grating vector (see inset of Fig. 4.1) of the sail is directed radially inward from the center of the sail and is expressed

$$\vec{K} = -(2\pi/\Lambda)\left(\cos\psi\ \hat{x}' + \sin\psi\ \hat{y}'\right) \qquad (4.2)$$

where Λ is the grating period and ψ is the polar angle measured counterclockwise from $\hat{x}'$. At normal incidence, the angle between $\hat{Z}$ and $\hat{z}$ is zero i.e., the sail normal and incident wave-vector are perfectly aligned and the grating functions as a reflective axicon.

For an arbitrary attitude, the momentum imparted to the sail may be determined from the difference of linear photon momenta before and after diffraction. This difference is quantified by the photon momentum transfer efficiencies in the two reference frames:

$$\vec{\eta}' = \left(\vec{k}'_i - \vec{k}'_d\right)/(2\pi/\lambda) \qquad (4.3a)$$

$$\vec{\eta} = \left(\vec{k}_i - \vec{k}_d\right)/(2\pi/\lambda) \qquad (4.3b)$$

where $\vec{k}'_i$ ($\vec{k}_i$) is the incident wave vector in the sail frame (stationary frame) and $\vec{k}'_d$ ($\vec{k}_d$) is the diffracted wave vector in the sail frame (stationary frame). For example, if $\vec{k}_d = -\vec{k}_i = -(2\pi/\lambda)\hat{Z}$ then $\vec{\eta} = 2\hat{Z}$. We note that for a Doppler-free elastic process $|\vec{\eta}'| = |\vec{\eta}|$. For an arbitrary sail attitude the method of Euler angles is use to relate the wave vectors in the two reference frame (see Appendix 1). However, it is instructive to first consider a sail that is tipped in a single direction as depicted in Fig. 4.1.

Let us therefore set $\zeta_Y = \zeta_Z = 0$ and consider a rotation angle ζ_X about the $\hat{X}$ axis. The angle ζ_X represents the attitude of the sail normal($\hat{z}'$) with respect to the beam axis ($\hat{Z}$) and is measured counterclockwise from $\hat{Z}$ i.e., $\zeta_X < 0$ for the attitude of sail shown in Fig.4.1. The angle of incidence $\beta_{i,x}$ is measured counterclockwise from the sail normal such that $\beta_{i,x} = -\zeta_X$ and $\beta_{i,x} > 0$ for the orientation shown in Fig.4.1.

In the sail reference frame the incident wave vector may be expressed

$$\vec{k}'_i = (2\pi/\lambda)\left(-\sin\beta_{i,X}\ \hat{y}' + \cos\beta_{i,X}\hat{z}'\right) = (2\pi/\lambda)\left(\sin\zeta_X\ \hat{y}' + \cos\zeta_X\ \hat{z}'\right) \qquad (4.4)$$

The diffracted wave vector $\vec{k}'_d$ is determined from the phase matching condition, whereby the phase of the electric field tangential to the sail surface is continuous at the interface:

$$\vec{k}'_i \cdot \hat{x}' = \vec{k}'_d \cdot \hat{x}' + m\vec{K} \cdot \hat{x}' \tag{4.5a}$$

$$\vec{k}'_i \cdot \hat{y}' = \vec{k}'_d \cdot \hat{y}' + m\vec{K} \cdot \hat{y}' \tag{4.5b}$$

where m is the integer valued diffraction order. For a normally incident beam where $\vec{k}'_i \cdot (\hat{x}' + \hat{y}') = 0$ and $\vec{k}'_d = -m\vec{K}$, the beam is diffracted toward the sail axis as desired and discussed below when $m = -1$.

Let us express the components of the diffracted wave vector by use of a unit vector $\hat{A}$:

$$\vec{k}'_d = (2\pi/\lambda)\,(A_{x'}\ \hat{x}' + A_{y'}\ \hat{y}' + A_{z'}\ \hat{z}') \tag{4.6}$$

where phase matching and elastic scattering ($|\vec{k}'_i| = |\vec{k}'_d)|$ provide

$$A_{x'} = -(m\lambda/\Lambda)\cos\psi \tag{4.7a}$$

$$A_{y'} = -\sin\beta_{i,X} - (m\lambda/\Lambda)\sin\psi = \sin\zeta_X - (m\lambda/\Lambda)\sin\psi \tag{4.7b}$$

$$A_{z'} = \pm(1 - A_{x'}^2 - A_{y'}^2)^{1/2} \tag{4.7c}$$

where the $-$ $(+)$ sign corresponds to a reflection (transmission) grating. To achieve efficient acceleration along the beam axis we assume a reflection grating in this report.

Let us now describe diffraction in the stationary reference frame where $\vec{k}_i = (2\pi/\lambda)\hat{Z}$ and

$$\vec{k}_d = (2\pi/\lambda)(B_X\hat{X} + B_Y\hat{Y} + B_Z\hat{Z}) \tag{4.8}$$

where the unit vector $\hat{B}$ is the rotated version of $\hat{A}$:

$$B_X = A_{x'} \tag{4.9a}$$

$$B_Y = A_{y'}\cos\beta_{i,X} + A_{z'}\sin\beta_{i,X} = A_{y'}\cos\zeta_X - A_{z'}\sin\zeta_X \tag{4.9b}$$

$$B_Z = -A_{y'}\sin\beta_{i,X} + A_{z'}\cos\beta_{i,X} = A_{y'}\sin\zeta_X + A_{z'}\cos\zeta_X \tag{4.9c}$$

General expressions relating rotated vectors $\hat{A}$ and $\hat{B}$ are described in Appendix 2.

We therefore find the components of the efficiency vectors:

$$\eta_{x'} = (m\lambda/\Lambda)\cos\psi \qquad\qquad \eta_X = -B_X \tag{4.10a}$$

$$\eta_{y'} = (m\lambda/\Lambda)\sin\psi \qquad\qquad \eta_Y = -B_Y \tag{4.10b}$$

$$\eta_{z'} = \cos\beta_{i,X} - A_{z'} = \cos\zeta_X - A_{z'} \quad \eta_Z = 1 - B_Z \tag{4.10c}$$

4.2 Optomechanics of a Diffractive Sail

The force and torque imparted to the sail produce both linear and angular displacements that depend on initial conditions and other factors such as the beam power, sail shape, and the spatial distribution of the grating vector. As depicted in Fig. 4.1 we assume a rigid circular sail of radius a whose distribution in the sail reference frame $\mathscr{F}'$ may be expressed:

$$P_{\mathscr{F}'} = \text{Circ}\left(\sqrt{x'^2 + y'^2}/a\right) \tag{4.11}$$

where the function $\text{Circ}(s)$ has a value of unity (zero) if $|s| < 1 (|s| > 1)$. A payload of mass M_p is attached to the sail of mass M_s by means of a rigid boom of mass M_b and length D_b and negligible thickness. A positive (negative) value of D_b corresponds to a non-exposed (exposed) payload. For convenience we assume $M_s = M_p$ such that the center of mass coincides with the mid-point of the boom. For this configuration the principal moment of inertia are $J_{x'} = J_{y'} = M_s a^2/4 + M_s D_b^2/4 + M_p D_b^2/4$ and $J_{z'} = Ma^2/2$ such that the sailcraft has a diagonal inertia tensor $J = \text{diag}(J_{x'}, J_{y'}, J_{z'})$.

An observer standing next to a stationary laser system will observe the sail moving through space in the $\mathscr{F} = (X, Y, Z)$ coordinate system, where the reference frame $\mathscr{F}$ is described by a right-handed set of unit vectors $\{\hat{X}, \hat{Y}, \hat{Z}\}$ and origin $\mathcal{O}$. We wish to predict the position, velocity, and attitude of the sail in that inertial reference frame. However, radiation pressure exerted on the sail is more readily described in the non-inertial reference frame of the sail, $\mathscr{F}'$, with right handed coordinate system (x', y', z') and origin $\mathcal{O}'$ (see Fig. 4.1). In a homogeneous coordinate system (see Appendix 3), an arbitrary point in $\mathscr{F}$ ($\mathscr{F}'$) is expressed as a column vector $[X, Y, Z, 1]^T$ ($[x', y', z', 1]^T$), where the 4th component is a scaling factor set to unity.

Radiation pressure on a sail gives rise to forces and torques that may translate and rotate the sail. The translation of the sail in the frame $\mathscr{F}$ may be described by the displacement vector $\boldsymbol{\delta} = [\delta_X, \delta_Y, \delta_Z]$. We represent the attitude of the sail in this frame in terms of ZYX sequence of Euler angles

$\{\zeta_Z, \zeta_Y, \zeta_X\}$ (see Appendix 1.) For an arbitrary rotation and translation the

relationship between the two frames of reference may be expressed

$$
\begin{bmatrix} x' \\ y' \\ z' \\ 1 \end{bmatrix} = \mathbf{H} \begin{bmatrix} X \\ Y \\ Z \\ 1 \end{bmatrix} = \begin{bmatrix} c_Y c_Z & c_Y s_Z & -s_Y & \delta_X \\ s_X s_Y c_Z - c_X s_Z & s_X s_Y s_Z + c_X c_Z & s_X c_Y & \delta_Y \\ c_X s_Y c_Z + s_X s_Z & c_X s_Y s_Z - s_X c_Z & c_X c_Y & \delta_Z \\ 0 & 0 & 0 & 1 \end{bmatrix} \begin{bmatrix} X \\ Y \\ Z \\ 1 \end{bmatrix}
$$
(4.12)

where $\boldsymbol{H}$ is the Homogeneous transformation matrix described in Appendix 3, and the elements containing factors of $c_{X,Y,Z} = \cos \zeta_{X,Y,Z}$ and $s_{X,Y,Z} = \sin \zeta_{X,Y,Z}$ belong to the rotation matrix described in Appendix 1.

The net radiation pressure force in the stationary reference frame is found by integrating over the local force elements:

$$
\vec{F}_{net} = (1/c) \iint\limits_{-\infty}^{\infty} I \ P_{\mathscr{F}} \ \cos \phi \ \vec{\eta} \ dX \ dY = M \ddot{\vec{\delta}}
$$
(4.13)

where $P_{\mathscr{F}'}$ is transformed into the reference frame $\mathscr{F}$ by the expression $P_{\mathscr{F}} = \mathbf{H}^{-1} P_{\mathscr{F}'}$, ϕ is the angle between the sail normal and the incident wave vector (i.e., $\cos \phi = \left(\hat{Z} \cdot \hat{z}' \right)$), $I = |E(X,Y,Z)|^2$ is the beam irradiance described in Eq.(4.1), c is the speed of light, and we have applied Newton's second law to the right hand side where $M = M_s + M_p + M_b$ is the total light sail mass.

Unlike the net force, the net torque $\vec{N}'_{net}$ measured about the center of mass of the sail is calculated in the sail reference frame $\mathscr{F}'$ and may be found by integration:

$$
\vec{N}'_{net} = (1/c) \iint\limits_{-\infty}^{\infty} I \ P_{\mathscr{F}'} \ \cos \phi \ \vec{r}' \times \vec{\eta}' \ dx' dy'
$$
(4.14)

where $\vec{r}' = x' \hat{x}' + y' \hat{y}' - (D_b/2) \hat{z}'$ is the moment arm. Euler's equations for rotational degrees of freedom may be expressed

$$
\begin{aligned}
N_{net,x'} &= J_{x'} \dot{\Omega}_{x'} + (J_{z'} - J_{y'}) \Omega_{y'} \Omega_{z'} \\
N_{net,y'} &= J_{y'} \dot{\Omega}_{y'} + (J_{x'} - J_{z'}) \Omega_{z'} \Omega_{x'} \\
N_{net,z'} &= J_{z'} \dot{\Omega}_{z'} + (J_{y'} - J_{x'}) \Omega_{x'} \Omega_{y'}
\end{aligned}
$$
(4.15)
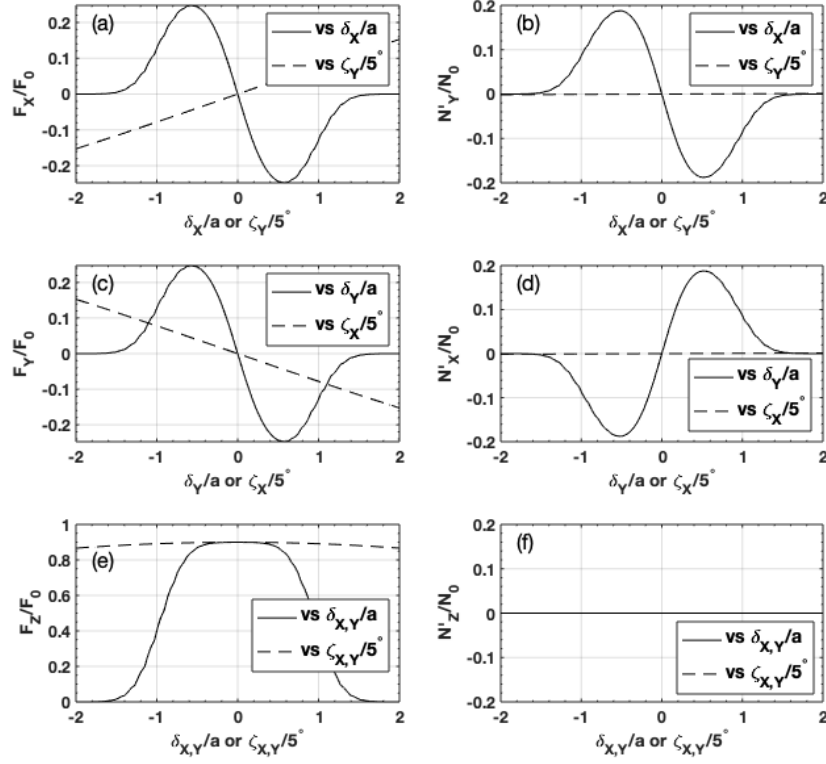
Figure 4.2: Normalized components of (a,c,e) force and (b,d,f) torque as a function of transverse displacement, $\delta_{X,Y}$, and attitude, $\zeta_{X,Y}$, where $F_0 = 2P_0/c$ and $N_0 = F_0 D_b/2$

.

where the angular velocity of the sail measured in the reference frame $\mathscr{F}'$ is related to the time rate of change of Euler angles (see Appendix 1.)

$$\dot{\vec{\Omega}}' = (\dot{\zeta}_X - s_X \dot{\zeta}_Z)\,\hat{x}' + (c_X \dot{\zeta}_Y + c_Y s_X \dot{\zeta}_Z)\,\hat{y}' + (-s_X \dot{\zeta}_Y + c_Y c_X \dot{\zeta}_Z)\,\hat{z}' \qquad (4.16)$$

and where the dot symbol represents the time derivative. The displacement, velocity, attitude, and angular velocity of the sail may be found by simultaneously solving the coupled equations, Eqs.(4.13) - (4.16).

4.3   Linear Stability Analysis of a Diffractive Sail

From a practical point of view we desire the sail to accelerate in the $\hat{Z}$ direction while otherwise at an equilibrium position centered on the beam and an equilibrium attitude with the sail axis parallel to the optical axis. To determine whether a given set of system parameters satisfies this requirement, linear stability analysis is applied [35]. Let us define a state vector: $\mathbf{q} = [\delta_X, \delta_Y, \zeta_X, \zeta_Y, \dot{\delta}_X, \dot{\delta}_Y, \dot{\Omega}_X, \dot{\Omega}_Y]^T$. The linearized equations of motion for translation and rotation may be expressed:

$$\dot{\mathbf{q}} = \mathbf{\Gamma_0 q} = \begin{bmatrix} \dot{\delta}_X \\ \dot{\delta}_Y \\ \dot{\Omega}_X \\ \dot{\Omega}_Y \\ \ddot{\delta}_X \\ \ddot{\delta}_Y \\ \ddot{\Omega}_X \\ \ddot{\Omega}_Y \end{bmatrix} = \begin{bmatrix} 0 & 0 & 0 & 0 & 1 & 0 & 0 & 0 \\ 0 & 0 & 0 & 0 & 0 & 1 & 0 & 0 \\ 0 & 0 & 0 & 0 & 0 & 0 & 1 & 0 \\ 0 & 0 & 0 & 0 & 0 & 0 & 0 & 1 \\ \Gamma_1 & \Gamma_2 & 0 & 0 & 0 & 0 & 0 & 0 \\ \Gamma_3 & \Gamma_4 & 0 & 0 & 0 & 0 & 0 & 0 \\ 0 & 0 & \Gamma_5 & \Gamma_6 & 0 & 0 & 0 & 0 \\ 0 & 0 & \Gamma_7 & \Gamma_8 & 0 & 0 & 0 & 0 \end{bmatrix}_{\mathbf{q_0}} \begin{bmatrix} \delta_X \\ \delta_Y \\ \zeta_X \\ \zeta_Y \\ \dot{\delta}_X \\ \dot{\delta}_Y \\ \dot{\Omega}_X \\ \dot{\Omega}_Y \end{bmatrix} \quad (4.17)$$

where $\mathbf{\Gamma_0}$ is calculated at the equilibrium state $\mathbf{q_0} = \mathbf{0}$:

$$\Gamma_1 = \frac{1}{M}\frac{\partial(F_X/F_0)}{\partial\delta_X}\Big|_{\mathbf{q_0}}, \ \Gamma_2 = \frac{1}{M}\frac{\partial(F_X/F_0)}{\partial\zeta_Y}\Big|_{\mathbf{q_0}}, \ \Gamma_3 = \frac{1}{J_{y'}}\frac{\partial(N_{y'}/N_0)}{\partial\delta_X}\Big|_{\mathbf{q_0}}, \ \Gamma_4 = \frac{1}{J_{y'}}\frac{\partial(N_{y'}/N_0)}{\partial\zeta_Y}\Big|_{\mathbf{q_0}},$$

$$\Gamma_5 = \frac{1}{M}\frac{\partial(F_Y/F_0)}{\partial\delta_Y}\Big|_{\mathbf{q_0}}, \ \Gamma_6 = \frac{1}{M}\frac{\partial(F_Y/F_0)}{\partial\zeta_X}\Big|_{\mathbf{q_0}}, \ \Gamma_7 = \frac{1}{J_{x'}}\frac{\partial(N_{x'}/N_0)}{\partial\delta_Y}\Big|_{\mathbf{q_0}}, \ \Gamma_8 = \frac{1}{J_{x'}}\frac{\partial(N_{x'}/N_0)}{\partial\zeta_X}\Big|_{\mathbf{q_0}}$$

$$(4.18)$$

By calculating the eigenvalues of the Jacobian of $\mathbf{\Gamma}_0$, we determine complex frequencies that correspond to state solutions having the time-dependent form $\exp(\gamma_{a,b}t)$, where real values of $\gamma_{a,b}$ provide exponential damping or gain, and imaginary values provide oscillations. Four complex frequencies are found which satisfy:

$$\gamma_a = \pm\sqrt{\frac{1}{2}\left(\Gamma_1 + \Gamma_4 \pm \sqrt{(\Gamma_1 - \Gamma_4)^2 + 4\Gamma_2\Gamma_3}\right)} \equiv \gamma_{a,r} + i\omega_a \qquad (4.19a)$$

$$\gamma_b = \pm\sqrt{\frac{1}{2}\left(\Gamma_5 + \Gamma_8 \pm \sqrt{(\Gamma_5 - \Gamma_8)^2 + 4\Gamma_6\Gamma_7}\right)} \equiv \gamma_{b,r} + i\omega_b \qquad (4.19b)$$

where $\gamma_{a,r}$, $\gamma_{b,r}$, ω_a, ω_b are real values. The conditions for linear stability are $\gamma_{a,r} \leq 0$ and $\gamma_{b,r} \leq 0$, i.e., exponential growth is prohibited. For $\gamma_{a,r} = \gamma_{b,r} = 0$ as

found below, the sail oscillates about the equilibrium point with four characteristic periods that depend on system parameters such as the grating period, the size of the sail, the beam size and power, and the moment of inertia of the light sail. What is more, for the symmetric system considered in this report $\Gamma_1 = \Gamma_5 < 0$, $\Gamma_4 = \Gamma_8 = 0$, and $\Gamma_2\Gamma_3 = \Gamma_6\Gamma_7 < 0$, $\Gamma_1^2 > 4|\Gamma_2\Gamma_3|$ and we therefore find two degenerate frequencies: a high frequency ω_h and a low frequency ω_l satisfying

$$\omega_h^2 = (1/2)(\omega_0^2 + \Delta^2) \tag{4.20a}$$
$$\omega_l^2 = (1/2)(\omega_0^2 - \Delta^2) \tag{4.20b}$$

where $\omega_0^2 = \Gamma_1 + \Gamma_4 = \Gamma_5 + \Gamma_8$ and $\Delta^2 = ((\Gamma_1 - \Gamma_4)^2 + 4\Gamma_2\Gamma_3)^{1/2} = ((\Gamma_5 - \Gamma_8)^2 + 4\Gamma_6\Gamma_7)^{1/2}$. Therefore we expect the system to display two oscillation modes when excited close to equilibrium.

4.4 Numerical Solutions

Closed form solutions of the system equations of motion generally do not exist and therefore, numerical integration methods must be applied. For a representative non-optimized case we examined a laser-sail system having parameters listed in Table 6.1. We assumed a beam power of $P_0 = 10[\text{kW}]$ (as was used in microwave beam-rider experiments [7, 6]) illuminating a sail of radius $a = 1[\text{m}]$, with the beam waist $w_0 = 0.5[\text{m}]$ under-filling the sail.

We numerically computed Eqs. (4.13) - (4.16) for different initial values of linear and angular displacement, plotting the results in Fig. 4.2. The linear nature of the force and torque near equilibrium is clearly evident in Fig. 4.2 for the range $|\delta_{X,Y}/a| < 0.5$ and $\zeta_{X,Y}| < 2.5°$. We also observe that the force along the beam axis reaches roughly 90% of the maximum theoretical value of $2P_0/c$. Furthermore, the value of the roll torque N_z' is zero, and thus the system is does not acquire angular momentum about the sail axis. Changing only the angle ζ_X (ζ_Y) at equilibrium we also find that the torque N_Y' (N_X') is zero valued.

A perspective of the net force exerted on the sail at equlibrium is depicted in Fig. 4.3(a) where local transverse components of force are displayed, resulting in no net transverse force. Similarly, the net torque exerted on the sail at equilibrium is depicted in Fig. 4.3(b) where local transverse components of torque, are displayed, resulting in no net transverse torque. If the sail is displaced from equilibrium to the
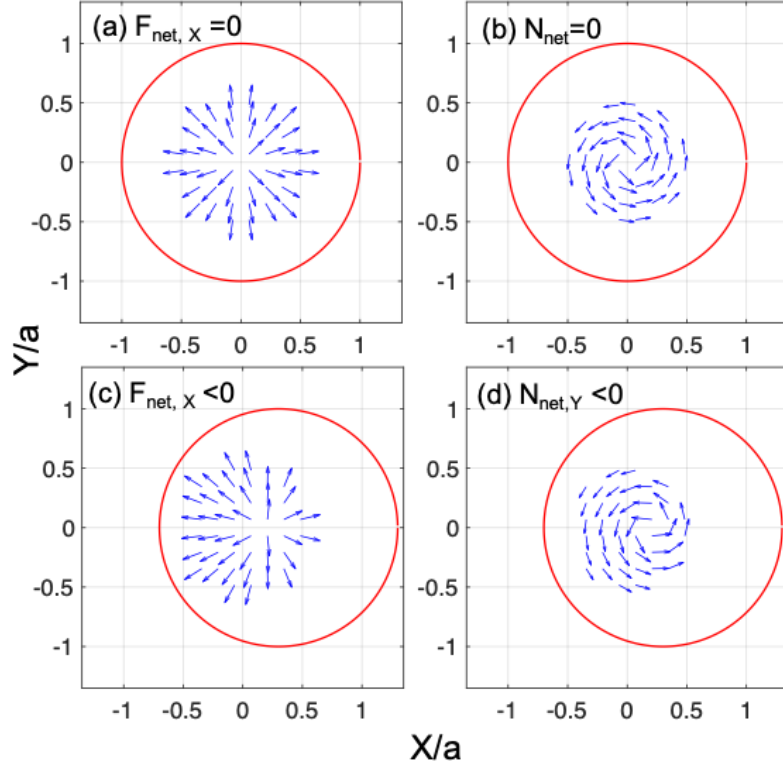
Figure 4.3: Local forces and torques exerted on an non-tilted axicon sail when the sail and optical axis are (a,b) co-linear, and (c,d) displaced. (c) The net force drives the sail toward the beam axis $(X, Y) = (0.0)$.

right, as in Fig. 4.3(c) the net force drives the sail to the left. In Fig. 4.3(d) the net torque is in the $-\hat{Y}$ direction.

Values of the slopes at the equilibrium points are obtained from Fig. 4.2, which along with the mass and moments of inertia in Table6.1, allow us to determine the values of Γ_j (see Eq.(4.18)). Inserting Γ_j into Eq.(4.20) we find $\omega_h = 0.18[\text{rad/s}]$ and $\omega_l = 0.087[\text{rad/s}]$, with respective oscillation periods $T_h = 35[\text{s}]$ and $T_l = 72[\text{s}]$. For a higher power laser beam $\tilde{P}$ we expect proportionally more optomechanical energy to be pumped into the system [52], resulting in higher squared values of frequency and lower squared values of the oscillation periods, $\tilde{T}_{h,l}$. Therefore

$$\tilde{T}_{h,l} = (P_0/\tilde{P})^{1/2} T_{h,l} \tag{4.21}$$

For example, if $P = 1[\text{GW}]$ the periods are expected to decrease to $T_h = 11[\text{ms}]$ and $T_l = 228[\text{ms}]$.

Solutions of the equations of motion for a given set of initial conditions were numerically solved by use of the 4th order Runge-Kutta method. An example that illustrates stable motion for small perturbations from equilibrium is shown in Fig. 4.4 for the system initially at rest and displaced: $\delta_X/a = -\delta_Y/a = 0.1$ and $\zeta_X = -\zeta_Y = 1°$. The phase diagrams correspond to an elapsed time of $t = 780 T_h = 27400[s]$. During this time the sail acquires a speed of $\Delta v_Z = 1.4[\text{km/s}]$ and traverses a distance of $\Delta Z = 19 \times 10^6[\text{km}] = 25 Z_0$, assuming the beam size is controlled so that it does not overfill the sail. As expected from our linear stability analysis, the system remains stable under this condition. The acceleration $a_Z = 0.51[\text{m/s}^2]$ may be increased in proportion to the laser power, thereby providing values of Δv_Z that are relevant for orbit-changing maneuvers, although the high oscillation frequencies (see above) may become mechanically intolerable if not damped.

An examination of Fig. 4.5 indicates that force and torque are nonlinearly related to linear and angular displacements for $|\delta_{X,Y}/a| \gtrsim 0.5$ and $|\zeta_{X,Y}| \gtrsim 2.5°$. Below these bounds the system may be characterized by linear and torsional spring models with stiffness values equal to the slopes in Fig. 4.2. Close to the nonlinear bounds the springs become soft and less able to provide a restoring force or torque. Beyond these bounds the system is driven away from equilibrium. To explore how the departure from linear behavior affects the range of stable motion for the system described in Table 6.1 we varied the initial conditions across the range $\delta_{X,Y} \in [-a, a]$, or $\zeta_{X,Y} \in [-10°, 10°]$, with $\dot{\delta}_{X,Y} = \dot{\Omega}_{X,Y} = 0$. We then numerically integrated the coupled equations of motion, categorized the observed motion as stable or unstable, and summarized the results in the stability maps shown in Fig. 4.5. The stable range of linear displacement (assuming $\zeta_{X,Y} = \dot{\delta}_{X,Y} = \dot{\Omega}_{X,Y} = 0$ at $t = 0$ indicates a stability zone defined by $\delta_X^2 + \delta_Y^2 \leq (0.3a)^2$ where the radius $0.3a$ is significantly smaller than the bound $\delta_{X,Y} = 0.5a$. We attribute this smaller zone to the weak force stiffness at $0.3a$ and coupling to motion in other degrees of freedom that do not provide an attraction to equilibrium. A linear zone boundary was found when varying both δ_X and ζ_Y (with other state parameters equal to zero), and is shown in Fig. 4.5(b). An examination of Fig. 4.5(b) indicates that the force at $\zeta_Y = 6°$ is equal and opposite to the force at $\delta_X = 0.3a$, suggesting both a reason and an equivalence for the the stability boundaries at $\delta_X = 0.3a$ and $\zeta_Y = 6°$. The same zone boundary relations was found when varying δ_Y and ζ_X. According to Fig. 4.5(c) the system stability is more robust to simultaneous displacements along and
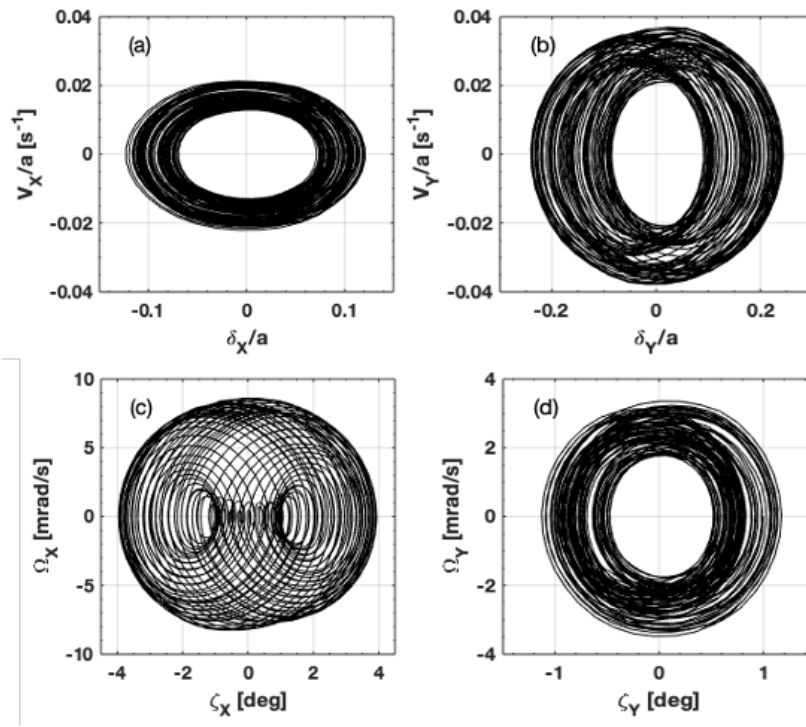
Figure 4.4: Phase plot for oscillations (a,b) along transverse direction and (c,d) in attitude about $(\hat{X}, \hat{Y})$ are shown, for an initial condition $\boldsymbol{q} = [0.1, -0.1, 1°, -1°, 0, 0, 0, 0]^T$ and time $t = 27400[s]$.

rotations about a common axis. Finally we explore an example where variations of the boom length and beam size affect stability. In this example we selected the initial condition: $\delta_X = -\delta_Y = 0.1a$ and $\zeta_X = -\zeta_Y = 1°$. As shown in Fig. 4.5(d) the system is generally more stable for long boom lengths, but for a given beam size there is a minimum boom length below which the system is unstable. For example, if the beam radius equals half the sail radius, $w_0 = a/2$, as listed in Table 6.1, we predict a minimum boom length of $D_b = 10a$. In comparison we made our numerical studies in Section 4.2 for a boom length of $D_b = 15a$, well into the stable regime. We also predict that stable motion may be achieved when the beam overfills the sail (i.e, $w_0 > a$), but only if the boom length is made significantly larger than the sail radius. For example if $w_0 = a$, stability requires $D_b > 28a$.
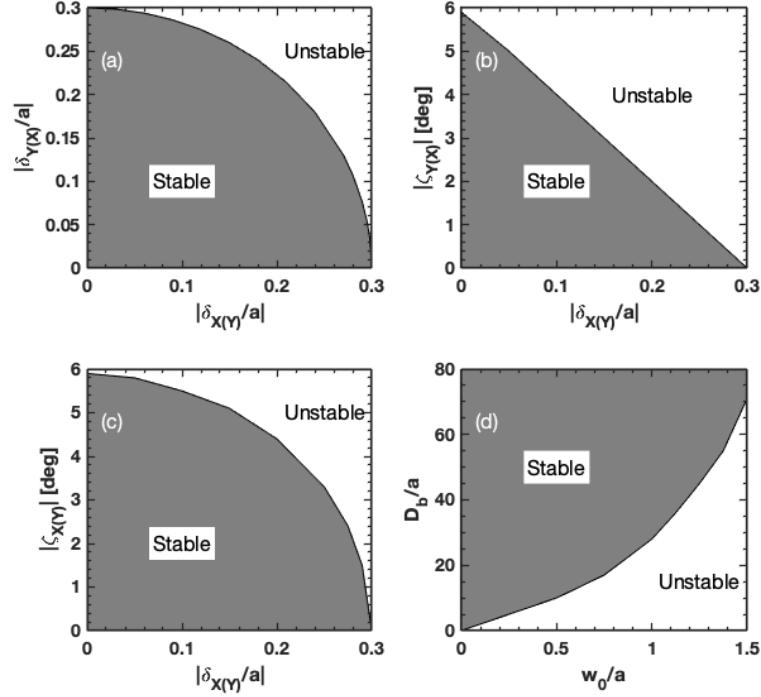
Figure 4.5: Regions of optomechanical stability for (a) relative linear displacement δ_X/a vs δ_Y/a, (b) orthogonal linear displacement and attitude axes, δ_X/a vs ζ_Y (or δ_Y/a vs ζ_X), (c) parallel linear displacement and attitude axes, δ_X/a vs ζ_X (or δ_Y vs ζ_Y) and (d) relative laser beam width vs. relative boom length w_0/a vs D_b/a.

4.5 Optimization of Sailcraft parameters

A stable diffractive axicon sailcraft with unity efficiency in the first order and a payload attached to it by means of a boom is shown in Fig.4.1. The stability of the sailcraft is shown to depend on several parameters, for example, boom length or diffraction efficiencies of different orders to name a few [54]. A sweep is performed for the following parameters looking for a combination that results in a stable sail, where the stability is evaluated for small perturbation using linear stability analysis [41]:

- the diffraction efficiency of mth reflected and transmitted order η_{r_m}, $\eta_{t_m} \in [0, 1]$.

- the ratio $\lambda/\Lambda \in [0.1, 0.9]$ where λ and Λ correspond to wavelength and grating period respectively.

- the boom length $D_b/L \in [-0.1, 0.2]$ where L is the radius of an axicon sail, where the negative (positive) sign implies a payload on the non-illuminated (illuminated) side of the sail.

- the beam-width $w_0/L \in [0.2, 2]$

To minimize the dimension of search space and to achieve tractable results, we keep the variables - beam width and boom length - fixed for a given instance. The results are displayed in Fig.5.2. It is evident from Fig.5.2(a-c), a stable sail may be achieved irrespective of the position of payload with respect to the sail center of mass i.e., $D_b/L \in [-0.1, 0, 0.1]$. What's more, the same is true even if the beam is expanding, as shown in Fig.5.2(d-f) when the beam-width w_0/L is more than tripled from the previous case. A quick glance on the same figure suggests a set of parameter values that are common in all the cases i.e., $\lambda/\Lambda = 0.9, \eta_{t_1} = 0.9, \eta_{r_0} = 0.1$, and all other diffraction efficiency values are zero. Thus, for these parameter values, a sail is stable for small perturbations while it continues to move forward under the influence of an expanding Gaussian laser beam.
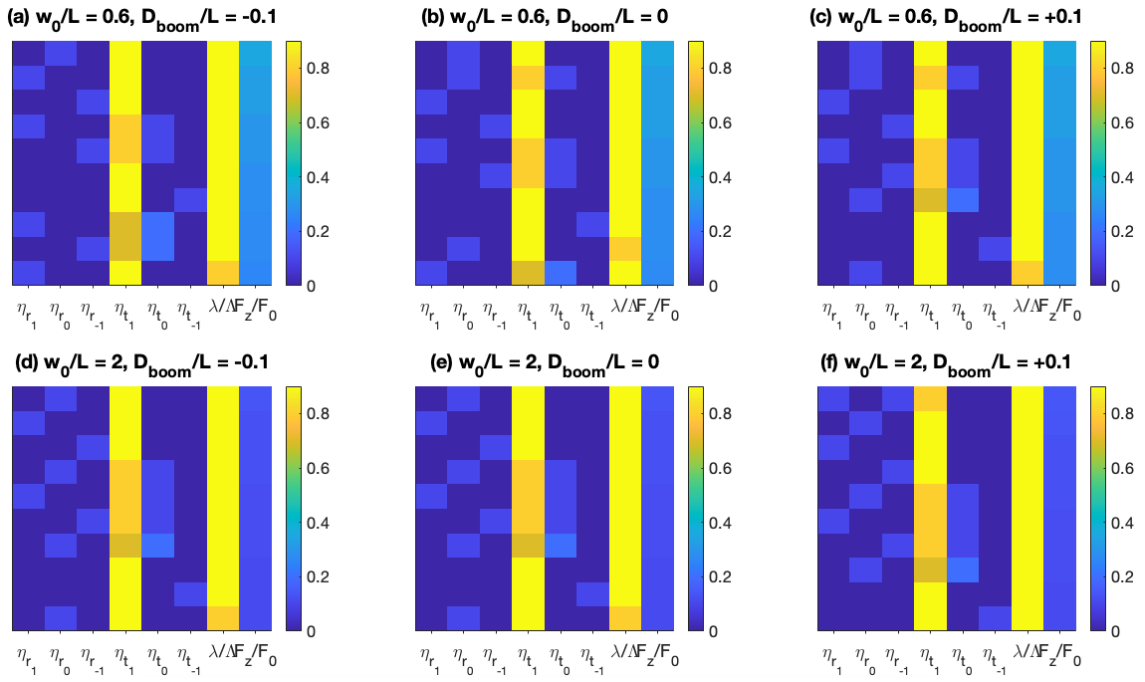
Figure 4.6: The set of parameter values required for a stable sail. The top ten results sorted by force along beam axis F_z are shown. $F_0 = 2P_0/c$, where P_0 is the peak power of incident beam.

Table 4.1: List of parameters and values

Parameters	Value
Light Sail	
Grating period, Λ	1.6 μm
Diffraction order, m	-1
Radius, a	1.0 m
Mass, M_s	0.50 g
Payload Mass, M_p	0.50 g
Boom Length, D_b	15.0 m
Boom Mass, M_b	0.17 g
Total Mass, M	1.17 g
Moments of Inertia, J'_x, J'_y	0.06 kg m^{-2}
Moments of Inertia, J'_z	0.25 gm^{-2}
Radius of Gyration, R_g	7.13 m
Laser Beam	
Power, P_0	10 kW
Gaussian beam waist, w_0	0.5 m
Wavelength, λ	1.0 μm
Diffraction length, Z_0	0.79×10^6m
System	
$\Gamma_1 = \Gamma_5$	-0.04 kg^{-1}m^{-1}
$\Gamma_2 = \Gamma_6$	0.05 kg^{-1}rad^{-1}
$\Gamma_3 = \Gamma_7$	-0.005 kg^{-1}m^{-3}
$\Gamma_4 = \Gamma_8$	0 kg^{-1}m^{-2}rad^{-1}
ω_0	0.2 rad/s
Δ	0.157 rad/s
ω_l	0.087 rad/s
ω_h	0.18 rad/s
T_h	35 s
T_l	72 s
Initial Conditions ($t = 0$):	
Displacement, (δ_X, δ_y)	(0.1 m, -0.1m)
Attitude, (ζ_X, ζ_Y)	$(1°, -1°)$
Linear Velocity, $(\dot{\delta}_X, \dot{\delta}_Y)$	(0,0)
Angular Velocity, $(\dot{\Omega}_X, \dot{\Omega}_Y)$	(0,0)

Chapter 5

Metasurface Beam-rider

The radiation pressure force and torque on a one-dimensional bi-grating composed of a $Si - SiO_2$ high contrast binary metagrating is analyzed for the purpose of stable beam riding whereupon a high power laser having an expanding Gaussian irradiance distribution propels the grating in outer space, free from gravitational forces. The binary metagrating structure has been simultaneously optimized to afford high forward thrust, and corrective restoring forces and torques in the event of small linear and angular disturbances. Unlike the designs in previous chapters, this design requires no offset between the sail and the payload by using a boom. We demonstrate that stability may be enhanced at the expense of forward thrust. The validity of our metamaterial findings is reinforced owing to good agreements between finite-difference time-domain and finite element numerical methods. To reduce mass and enhance forward acceleration this laser-driven sail was designed to be free of a stabilizing boom.

5.1 Introduction

Optical tweezers or single-beam optical traps are one of the most powerful means of contactless manipulation of nanoscopic/microscopic objects with a very diverse set of applications ranging from biology[22] to quantum optomechanics[8]. But the promise of optical tweezers to manipulate macroscopic objects of meter-scale has been held in check by the need for a tightly-focused beam that creates a gradient force in a very limited volume and effective distance. By engineering the scattering properties of the objects and the shape of the beam, the dynamics of macroscopic

objects may be controlled and used for successful trapping, manipulation, levitation, and even propulsion without the need for a tightly focused beam. Most recently, NASA and Breakthrough Starshot Initiative aim to leverage these radiation pressure forces to propel a meter-scale light sail to the nearest stars with relativistic speeds. Nearly all the stable geometric designs proposed so far in the literature are subprime in three senses: (a) the ability of a conical/spherical/concave/convex sail to maintain its shape is questionable (b) a flat diffractive/nanophotonic design demands an undesirable mast to offset the center of mass away from the sail to achieve stability [53] and (c) all the designs sacrifice on thrust force for levitation/propulsion to enable a restoring force for stability.

In this work, we demonstrate the stability of a bi-grating lightsail comprised of subwavelength unit-cells of Si/SiO$_2$. The unit-cell geometry is optimized to engineer diffraction efficiencies such that the sail is stable against linear and rotational perturbation without any offset between the center of mass and the sail while simultaneously achieving maximum forward thrust. This work is different from [5] in the sense: (1) forward thrust is also an objective of optimization (2) a stability basin is compared between two different forward thrusts that quantify the trade-off between forward thrust and stable initial conditions. What's more, the forces and torque are validated using FEM (MEEP) and FDTD (COMSOL) methods. The two-dimensional dynamical analysis and electromagnetic response presented in this work may be extended into three dimensions using the scheme described in [54, 37].

5.2   Theory

Consider the structure shown in Fig.5.1 composed of two different panels L (left) and R (right) of length ℓ. Each panel is comprised of an artificially designed subwavelength periodic lattice whose properties primarily arise from the design and distribution of meta-atoms or unit cells. Inspired by the principles of form birefringence and effective medium theory, the unit-cell of choice in this work is a ridge-width-modulated high contrast grating with Si nano-pillars on a low index SiO$_2$ substrate. As shown in Fig.5.1 (inset) is a multi-layer subwavlength binary unit-cell of period Λ. High-index Si nanopillars of height $h_1 = h_2$ are deposited on low-index SiO$_2$ substrate of thickness t. The width and position of the nanopillar is $w_{1,2}$ and $p_{1,2}$ respectively. There exist multiple benefits to using this subwavelength binary design: (a) this design has been shown to offer stable levitation [32], (b) optimal
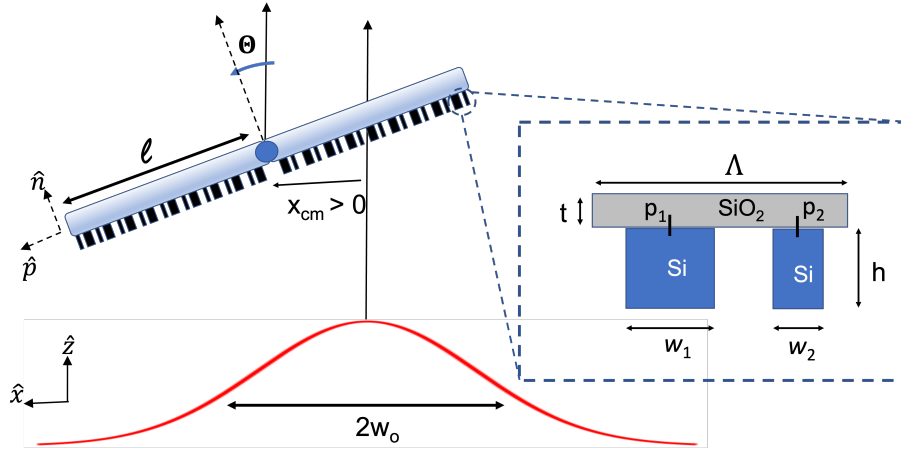
Figure 5.1: High contrast metasurface bi-grating configuration propelled by a Gaussian beam. The bi-grating is comprised of unit-cells with geometric parameters shown in the inset. $p_{1,2}$ is measured from the center of the unit-cell.

thermal management via radiative cooling [48], and (c) the feature sizes may be easily realized with existing e-beam lithography technology

The bi-grating may levitate or propel when illuminated owing to radiation pressure forces. To model these forces, it is convenient to consider two different frames of reference: $(\hat{x}, \hat{z})$ and $(\hat{p}, \hat{n})$ attached to the laser and bi-grating respectively. The bi-grating has a total mass M (including a payload) and the center of the bi-grating coincides with the center of mass of the system at x_{cm} such that there is no offset between the two. The two coordinate spaces are related to each other as $p = (x - x_{cm})/\cos\Theta$ where $\Theta = -\theta_i$ is the attitude of the sail rotated about $\hat{y}$ and θ_i is the angle of the beam incident on the bi-grating.

The meta-atoms offer exceptional control of wavefront and scattering response near their resonance, which may be engineered for desired force and torque on the bi-grating structure. Assuming a non-relativistic non-spinning bi-grating, the incident and scattered wavelengths are equal in the reference frame of the structure, and thus, the respective wave vectors may be expressed $\vec{k}_i = k\hat{n}$ and $\vec{k}_m^{L,R} = k(\cos\theta_m^{L,R}\,\hat{n} + \sin\theta_m^{L,R}\,\hat{p})$, where $k = 2\pi/\lambda$. The diffraction angles are governed by the grating equation,

$$\sin\theta_{t_m}^{L,R} = -\sin\theta_{r_m}^{L,R} = m\mathbb{K}^{L,R} - \sin\Theta \qquad (5.1)$$

where and $\mathbb{K}^{L,R}$ is the grating momentum such that $\mathbb{K}^L = -\mathbb{K}^R$ and $(\theta_{t_m}^{L,R}, \theta_{r_m}^{L,R})$ are the diffraction angles for the mth (transmitted, reflected) orders. The change in photon momentum $\Delta\vec{k}^{L,R} = (\vec{k}_i - \vec{k}_m^{L,R})/k_i$ in the reference frame of unit-cell may now be expressed

$$\Delta\vec{k}^{L,R}(\Theta) = -\sin\Theta\,\hat{p} + \cos\Theta\,\hat{n} - \sum_{m=-1}^{m=1}(\eta_{r_m}^{L,R}\sin\theta_{r_m}^{L,R} + \eta_{t_m}^{L,R}\sin\theta_{t_m}^{L,R})\hat{p}$$
$$- (\eta_{r_m}^{L,R}\cos\theta_{r_m}^{L,R} + \eta_{t_m}^{L,R}\cos\theta_{t_m}^{L,R})\hat{n} \tag{5.2}$$

where $\eta_{r_m,t_m}^{L,R}$ is the diffraction efficiency of mth reflected(r) or transmitted(t) modes from corresponding panels (L, R). Alternatively, the change in photon momentum may also be expressed

$$\Delta\vec{k}^{L,R}(\Theta) = \frac{1}{P_0/c}\left(\int_{\partial S}T_{ij}\cdot\hat{n}dA + \int_{\partial S}T_{ij}\cdot\hat{p}dA\right) \tag{5.3}$$

where T_{ij} the Maxwell Stress Tensor expressed as.

$$T_{ij} = \epsilon_0(E_iE_j - \frac{1}{2}|\mathbf{E}|^2\delta_{ij}) + \frac{1}{\mu_0}(B_iB_j - \frac{1}{2}|\mathbf{B}|^2\delta_{ij}) \tag{5.4}$$

where E and B are electric and magnetic field respectively, mu_0 and $epsilon_0$ are permeability and permittivity of free space and δ_{ij} is the kronecker delta function.

The bi-grating may experience force and torque when illuminated by a laser beam of peak power P_0, wavelength $\lambda << L$, characteristic beam-width $2w_0$, and a Gaussian irradiance distribution

$$I(p) = \frac{P_0}{2w_0^2\sqrt{\pi/2}}\cos\Theta\exp\left(-2\frac{(p\cos\Theta + x_{cm})^2}{w_0^2}\right) \tag{5.5}$$

and the force $\vec{F}^{L,R}$ and torque $\vec{N}^{L,R}$ of each panel may now be expressed

$$\vec{F}^L(p,\Theta) = \int_{-\ell}^0\frac{I(p)}{c}\Delta\vec{k}^Ldp \quad \& \quad \vec{F}^R(p,\Theta) = \int_0^\ell\frac{I(p)}{c}\Delta\vec{k}^Ldp \tag{5.6a}$$

$$\vec{N}^L(p,\Theta) = \int_{-\ell}^0 p\hat{p}\times\frac{I(p)}{c}\Delta\vec{k}^Ldp \quad \& \quad \vec{N}^R(p,\Theta) = \int_0^\ell p\hat{p}\times\frac{I(p)}{c}\Delta\vec{k}^Rdp \tag{5.6b}$$

such that the transverse (F_x) and longitudinal (F_z) forces in the reference frame of the beam may be expressed

$$F_x = (F_p^L \cos \Theta + F_p^R \cos \Theta + F_n^L \sin \Theta + F_n^R \sin \Theta)\hat{x} \qquad (5.7a)$$

$$F_z = (F_n^L \cos \Theta + F_n^R \cos \Theta - F_p^L \sin \Theta - F_p^R \sin \Theta)\hat{z} \qquad (5.7b)$$

and the torque is the same in both the frames of reference.

The non-spinning two-dimensional system described above entails 3 degrees of freedom: translation along $\hat{x}$ and rotation about $\hat{y}$ while it is propelled along $\hat{z}$. We define a state vector $\mathbf{x} = [x, \theta]^T$ to analyze the stable transverse dynamics of the bi-grating system. In a close analogy of a oscillating spring system, the transverse dynamics of the bi-grating may be linearized and expressed as a set of ordinary differential equations (ODE) $\ddot{\mathbf{x}} = -K\mathbf{x}$, where K is a Jacobian with *stiffness* coefficients

$$K = \begin{bmatrix} k_1 & k_2 \\ k_3 & k_4 \end{bmatrix} = \begin{bmatrix} \frac{1}{M}\frac{\partial F_x}{\partial x} & \frac{1}{M}\frac{\partial F_x}{\partial \Theta} \\ \frac{1}{J_y}\frac{\partial N_y}{\partial x} & \frac{1}{J_y}\frac{\partial N_y}{\partial \Theta} \end{bmatrix}_e \qquad (5.8)$$

where the coefficients are evaluated in the close proximity of equilibrium point $\mathbf{x}_e = [0, 0]^T$, implied by e. The metasurface is said to be marginally stable if $\mathrm{Im}(\mathbf{eig}(K)) = 0$ and $\mathrm{Re}(\mathbf{eig}(K)) < 0$ i.e., only real eigenvalues are allowed such that the frequencies of oscillation are real. In general, the system will exhibit two stable oscillation frequencies $\omega_{1,2} = \sqrt{-\mathrm{Re}(\mathbf{eig}(K))}/2\pi$ Hz. Note that, we add no restrictions on the nature of the stiffness coefficients, they can either be positive or negative.

5.3   Computational Electromagnetics & MEEP

We may conclude from Eq.5.2 and Eq.5.6 that it is possible to engineer a unit-cell geometry that simultaneously high forward thrust and stability against small perturbation. However, the forces depends on η and analytically characterizing the diffraction efficiencies is very difficult except for simpler geometries.

A closed-form solution to Maxwell's equations involving various media and boundary conditions for an arbitrarily shaped structure is almost impossible to derive analytically except a few simpler cases. However, real-world problems like scattering, absorption, and radiation in an arbitrarily shaped device may be designed, optimized, and modeled with the help of various computational numerical techniques. Computational Electromagnetics computes the evolution of $\vec{E}$ and $\vec{H}$ fields under
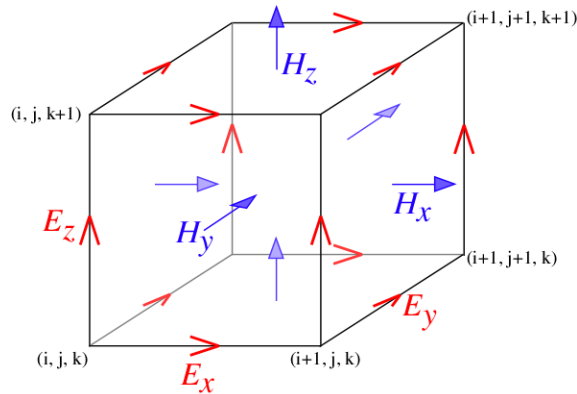
Figure 5.2: Yee lattice for a cubic grid voxel. [21].

constitutive relations and boundary conditions of the device. These fields may be used afterward to calculate the flow of power (Poynting vector), modes in a waveguide, dispersion, and scattering by the media.

There exist a plethora of numerical techniques to perform numerical electromagnetic simulations. The choice of technique is very important because each of those techniques is appropriate only for a particular kind of problem and a wrong technique may result in either wrong results or will take an excessively long time to compute. For example, computers often discretize space and time in orthogonal or non-orthogonal grids and accurate modeling of curved geometry often requires a non-orthogonal geometry, often used in Finite Element Methods (FEM). Whereas, transient fields and impulse field effects are modeled using finite difference time domain (FDTD) methods.

Since we are modeling diffraction gratings with simple geometries, we chose to perform electromagnetic simulations in MEEP, which is based on the FDTD method. FDTD discretizes the modeling space into what is known as Yee lattice, as shown in Fig.5.2 The three components of $\vec{E}$ are stored along the edges of the cube and the three components of $\vec{H}$ are stored on the faces of the cube. Maxwell's equations are now solved in a cyclic fashion- the electric field is solved at an instant, and the magnetic field is solved in the following instant and the process is repeated over and over again.

For the aforementioned unit-cell, rigorous diffraction theory must be applied. We make use of an FDTD based package in Python called MEEP [45] to solve

Table 5.1: Optimized Geometries [in μm] (t=0.5 μm, $\lambda = 1.2$ μm)

	n_{Si}	n_{SiO_2}	Λ	h	p_1	w_1	p_2	w_2	$F_z/(P_0/c)$
Unit-cell I	3.5220	1.4582	2.24	0.78	-0.50	0.80	0.46	0.56	120%
Unit-cell II	3.5220	1.4582	2.24	0.80	-0.52	0.76	0.46	0.54	170%

for Maxwells Equation. The boundary conditions are assumed to be PML (Bloch periodic) along $\hat{n}(\hat{p})$. To account for fabrication constraints and numerical dispersion problem in FDTD, we limit our resolution to a step size of 20 nm or 50 pixels per micron. When an in-the plane polarizatied light of wavelength λ is incident on the structure, the simulation is ran until the fields have decayed to 10^{-6} of their peak value. A similar FEA simulation is performed in COMSOL to validate the results from MEEP. The problem may now be formulated in terms of a multi-objective optimization problem i.e., for the set of variables $(\Lambda, h, p_{1,2}, w_{1,2})$ along with Si(n = 3.5220)/SiO$_2$(n = 1.4582), we are seeking a sail design with with two figures of merit (FOM): (a) FOM$_1$ = Im(**eig**(K)) is minimized until it is 0 and (b) the forward thrust F_z/F_0 is maximized, where $F_0 = 2P_0/c$. The optimization is performed using a genetic algorithm called NSGA-II [18] for the bi-grating-beam system for the following parameters: $L = 1$, $w_0 = 0.5L$, $\lambda = 1.2\mu$m, $M = 1$gm, and $P_0 = 10$ kW.

5.4 Pareto Optimization and NSGA-II

Pareto optimization, also known as multi-objective optimization, is a technique used in decision-making processes to find the optimal solutions when multiple conflicting objectives need to be considered simultaneously. It is based on the concept of Pareto dominance, which states that one solution is considered better than another if it is at least as good in all objectives and strictly better in at least one objective. In Pareto optimization, the goal is to find a set of solutions that represent a trade-off between different objectives, rather than a single optimal solution. These solutions are known as Pareto-optimal or non-dominated solutions. They lie on the Pareto front, which is the curve formed by connecting the best solutions in each objective space. Pareto optimization provides decision-makers with a range of choices, allowing them to make informed decisions based on their preferences and priorities.

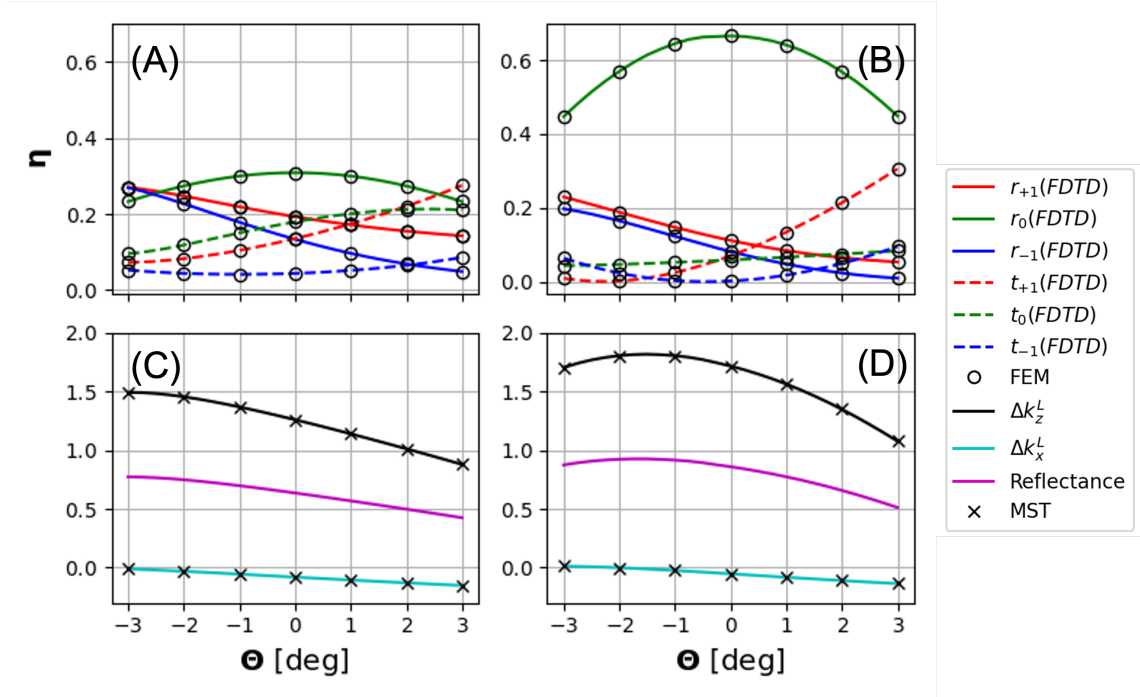NSGA-II (Nondominated Sorting Genetic Algorithm II) [19] is a popular algo-

Figure 5.3: The diffraction efficiencies of each orders for a sail tilted by Θ. (A) and (B) correspond to the two structures with $F_z/(P_0/c) = 1.26$ and $F_z/(P_0/c) = 1.70$ respectively. Straight Line and Circles correspond to MEEP (FDTD) and COMSOL (FEM) results respectively.

rithm used for Pareto optimization. It is an evolutionary algorithm that simulates the process of natural selection to evolve a population of solutions towards the Pareto front. NSGA-II maintains a diverse set of solutions by using a fast non-dominated sorting technique and a crowding distance assignment mechanism. The algorithm begins with an initial population of candidate solutions, typically generated randomly or through a heuristic. It then applies selection, crossover, and mutation operators to create a new population of offspring solutions. The non-dominated sorting technique is used to rank the solutions based on dominance relationships, dividing them into different fronts. Solutions in the first front are non-dominated, while those in subsequent fronts are dominated by solutions in previous fronts.

To maintain diversity in the population, NSGA-II uses a crowding distance measure to guide the selection of solutions for the next generation. The crowding distance is a measure of how close a solution is to its neighbors in the objective space. Solutions with larger crowding distances are preferred to maintain a uniform distribution along the Pareto front. The process of selection, crossover, and mutation, followed by non-dominated sorting and crowding distance assignment, is repeated for several generations. As the algorithm progresses, the population evolves towards the Pareto front, providing a diverse set of solutions that represent the trade-off between the conflicting objectives.

5.5   Result & Analysis

Since, this is a multi-objective optimization problem, there is no single solution. Instead, there exist many solutions that are Pareto-optimal i.e., lie at the optimal trade-off between two competing objectives. From the multiple Pareto-optimal solutions that were achieved, selected some fabrication-friendly designs shown in Table 5.1. The diffraction efficiency of both the unit-cell geometries comprising the left panel is evaluated using MEEP(FDTD) and COMSOL(FEA) and is shown in Fig.5.3(a) and (b) as the function of incident angle. An excellent agreement is evident between the two methods. The change in photon momentum $\delta \vec{K}(\theta)$ is evaluated using both diffraction efficiency and Maxwell stress tensor and an excellent agreement between the two may be seen in Fig.5.3(c) and (d). Clearly both the structure have very high reflectance that enables high forward thrust and hence Δk_z^L, whereas a non-zero Δk_x^L enables restoring stable force for non-equilibrium positions, as shown in Fig.5.3(c) and (d).
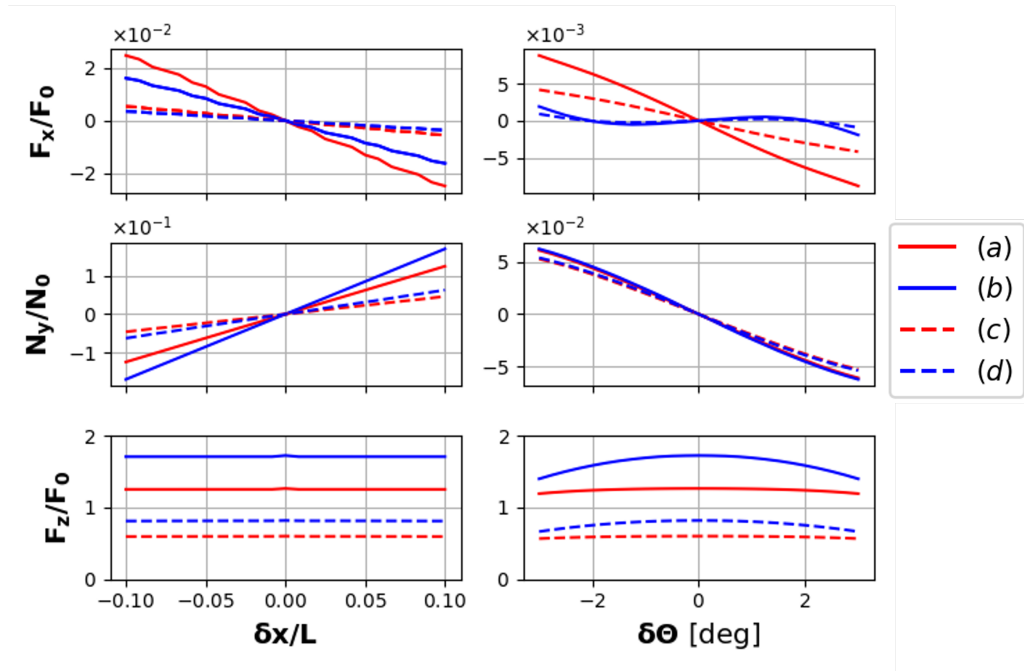
Figure 5.4: Force and Torque as a function of displacement and rotational perturbation for the two sail unit-cell designs. (a)$(w_0 = \ell/2, F_z/F_0 = 1.20)$ (b)$(w_0 = \ell/2, F_z/F_0 = 1.70)$ (c)$(w_0 = \ell, F_z/F_0 = 0.45)(d)(w_0 = \ell, F_z/F_0 = 0.60)$
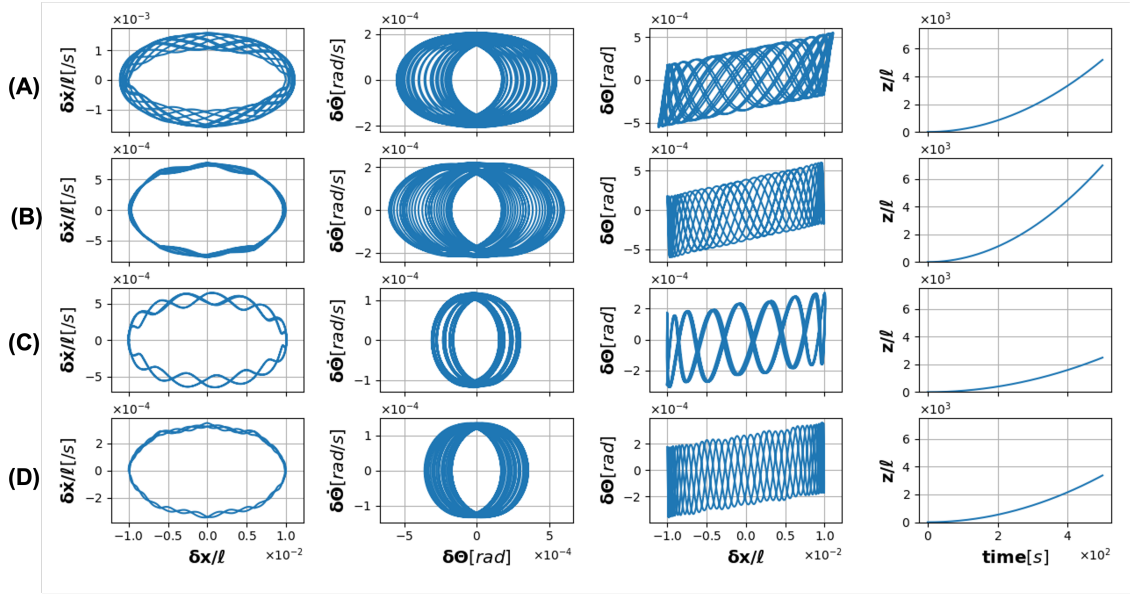
Figure 5.5: Runge-Kutta solution of equation of motion for the two sail designs for both (beam-width, forward thrust):(A)$(w_0 = \ell/2, F_z/F_0 = 1.20)$ (B)$(w_0 = \ell/2, F_z/F_0 = 1.70)$ (C)$(w_0 = \ell, F_z/F_0 = 0.60)$ (D)$(w_0 = \ell, F_z/F_0 = 0.45)$

The total force and torque on the bi-grating, however, is the result of the individual response of each panel with respect to the beam center. Thus, the force and torque are the functions of both angle and displacement from the equilibrium point. Shown in Fig.5.4 is the force and torque on the bi-grating for both the structures assuming an expanded filling $(w_0 = \ell)$ and non-expanded underfilling $(w_0 = 0.5\ell)$ beam. It is evident from the figure the restoring force and torque are linear for small perturbations from the equilibrium point and the slope of these curves correspond to Jacobians as described in Eq.5.8 for Linear stability analysis purposes.

Linear stability analysis however provides only a partial picture of stability i.e., the stability of the system for very small perturbations near the equilibrium point. And hence the equations of motion must be solved using numerical methods like Runge-Kutta to fully gain an understanding of system stability. For an initial perturbation of $(\delta x/\ell = 0.01, \delta\theta = 0.01\text{rad}, \delta\dot{x}/\ell = 0, \delta\dot{\theta} = 0)$, the equations of motion are solved for the two geometries and two different beam width $w_0 = 0.5\ell$ and $w_0 = \ell$. The results are shown in Fig.5.5. The phase maps for all the cases are
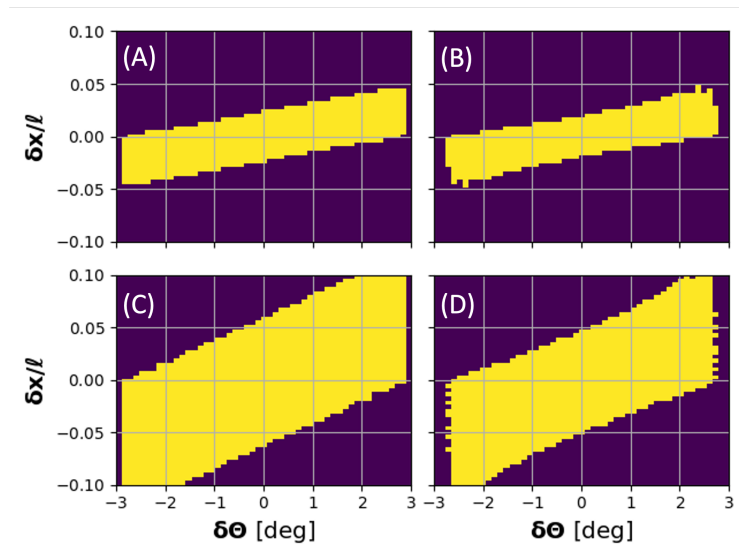
Figure 5.6: Light Sail with stable trajectory for initital perturbation and rotation assuming (beam width, forward thrust): (A)$(w_0 = \ell/2, F_z/F_0 = 1.20)$ (B)$(w_0 = \ell/2, F_z/F_0 = 1.70, 499/2601)$ (C)$(w_0 = \ell, F_z/F_0 = 0.60)$ (D)$(w_0 = \ell, F_z/F_0 = 0.45)$

closed, suggesting a stable system. Please note, these simulations were performed for $P_0 = 10$kW and for a gigawatt class laser as proposed in Breakthrough Starshot system will remain closed and bounded albeit the frequency of oscillation will be scaled accordingly.

The above simulation is repeated for a range of initial conditions to test the limits of stability and is shown in Fig.5.6. It is evident from Fig.5.6(A) and (B), an increase in forward thrust from 120% to 170% leads to 3.4% shrinkage in stable basin for an underfilling beam-width. Similar behavior may be observed for an expanding beam Fig.5.6(C) and (D) i.e., high forward thrust implies sacrifice on permissible stable conditions. However, the expanded beam imparts lower forward thrust than the non-expanded underfilling beam.

5.6 Conclusion

In conclusion, we designed, optimized, and cross-validated a rigid bi-grating light sail for stability and thrust. We proposed two different geometries with two dif-

ferent forward thrust forces while quantifying the bounds of stable initial condi-
tions. The sail is stable for both underfilling and expanded filling beams. The
design thus is an excellent choice for applications such as levitated optomechanics
of millimeter/centimeter-scale objects or laser propelled meter scaled light sail for
space missions limited to the solar systems. As a final remark, significant prac-
tical challenges exist in the realization of these sails. For example, the design is
very sensitive to wavelength and becomes unstable for Doppler-shifted wavelength
in the case of relativistic sails of Breakthrough Starshot. If a tunable phased-array
laser becomes a reality, the proposed design becomes an ideal choice. Moreover,
the non-rigidity of the light sail must be considered and modeled using Lagrangian
mechanics [43]. Similarly, the local deformation of the all-dielectric thin sail may be
optimized and modeled using the principles of conformal metasurfaces [63].

Chapter 6

Broadand Diffractive Solar Sail

The transverse radiation pressure force and acceleration is compared for two parametrically optimized designs: prismatic and two-pillar metasurface gratings. The numerical results were cross-verified with both Maxwell stress tensor and modal analysis. Solar blackbody irradiance was assumed for wavelengths ranging from 0.33 μm to the grating cutoff at 1.5 μm, encompassing 83% of the solar constant. This multi-objective optimizer study found that neither design comprised of Si_3N_4 performed as well as those corresponding to a low refractive index, low mass density material. The predicted transverse acceleration of the optimized low-index metasurface grating is compared to that of a state-of-the-art reflective solar sail.

6.1 Introduction

The in-space propulsion of sailcraft via solar radiation pressure was originally pioneered by in the 1920s by Tsander and Tsiolkvosy [59, 60]. In contrast to rockets which both transport significant amounts of fuel mass and make discrete orbit-changing burns, solar sails can attain extraordinarily high velocities given a low mass and continuous acceleration. Space organizations such as NASA, JAXA, and the Planetary Society, have improved the technical readiness level of solar sails in recent years, culminating in an assortment of proposed space science missions [33]. The advent of solar sailing has stimulated advanced concepts that consider the mission objectives as part of the sail design. For example, missions having a spiral trajectory toward or away from the sun benefit from a sail having an optimal "lift" force perpendicular to the sun line. To achieve lift a traditional reflective sail must

be tilted away from the sun; consequently the maximum lift cannot be achieved owing to the reduced illumination projected area. In contrast, optical scattering mechanisms like diffraction provide alternative means of transferring photon momentum to the sail in a preferred sun-facing orientation [57, 15, 16, 53, 54, 17, 25, 14, 58, 55, 1, 65, 9]. The maximum transverse force on the sail occurs when sunlight is uniformly scattered at 90° with respect to the surface normal of a sun-facing sail.
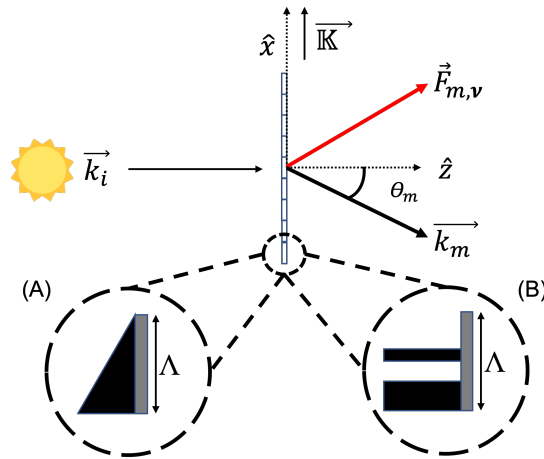
Figure 6.1: Schematic diagram of a solar sail with constituent (A) prism and (B) subwavelength pillar elements of period Λ and. The sail diffracts incident light $\vec{k_i}$ by θ_m into $\vec{k_m}$ owing to $\vec{\mathbb{K}}$, resulting in net radiation pressure force $\vec{F}$.

6.2   Theory

To advance the understanding of diffractive sails we explore two designs: a triangular prismatic grating and a metasurface grating comprised of two pillars. Two material strategies are analyzed for each design. First we consider an arbitrary non-dispersive dielectric material having a refractive index n_1 placed on a thin substrate of index $n_2 = 1.5$. Finite difference time domain (FDTD) methods are used to account for internal and external reflections of both polarization component of light, and moreover, the angular scattering distribution across a broad band of optical frequencies. Likewise, we determine the angular scattering distribution when the grating and thin substrate are made with Si_3N_4. The schematic illustration shown

in Fig. 6.1 depicts a portion of a flat rigid infinitely periodic grating with period Λ in the x, z-plane of incidence for a sun-facing configuration, comprised of either (A) prism elements or (B) pillars on a thin substrate. Structural flexing and non-normal incidence angle are beyond the scope of this baseline study. The grating period $\Lambda = 1.5\ [\mu\text{m}]$, or equivalently the grating frequency $\tilde{\nu} = c/\Lambda = 200[\text{THz}]$ was selected from a consideration of the spectral cut-off condition, the prism mass, and diffraction effects. The fraction of blackbody irradiance cut off from diffraction decreases with increasing value of Λ, whereas the mass of a prism varies as Λ^2. A large value of the transverse acceleration generally requires negligible spectral cut off and low mass, which combined with a diffraction analysis, provides a value of roughly $\Lambda = 1.5\ [\mu\text{m}]$.

Light is transmitted or reflected light into discreet diffraction angles θ_m measured with respect to the back surface normal as depicted in Fig. 6.1. In the reference frame of the sail, the incident and scattered wavelengths are equal, and thus, the respective wave vectors may be expressed $\vec{k}_i = k\hat{z}$ and $\vec{k}_m = k(\cos\theta_m\ \hat{z} + \sin\theta_m\ \hat{x})$, where $k = 2\pi/\lambda$. The diffraction angles are governed by the grating equation: $\sin\theta_m = m\lambda/\Lambda$ assuming normal incidence. We note that $\cos\theta_m = \pm\sqrt{1 - \sin^2\theta_m}$, where $+(-)$ corresponds to transmitted (reflected) light. The mth order photon momentum transfer efficiency imparted to the sail at the optical frequency $\nu = c/\lambda$ may be expressed $\vec{\eta}_{\nu,m} = (\vec{k}_i - \vec{k}_m)/k = (1 - \cos\theta_m)\ \hat{z} - \sin\theta_m\ \hat{x}$, where c is the speed of light, and normal incidence is assumed. For a light source having a spectral irradiance distribution $\tilde{I}(\nu)$ the net momentum transfer efficiency $\vec{\eta}$ may be found by integrating over all frequencies and summing over all allowed diffraction orders for both polarization modes [58]. For an unpolarized source like the sun, we assume the spectral irradiance is equally divided into s and p polarization states.

The net radiation pressure force on the sail may be expressed $\vec{F} = F_0\vec{\eta}$, where $F_0 = I_0 A/c$ where A is the sail area and I_0 is the irradiance. For example the solar blackbody irradiance between $\nu_{\min}$ and $\nu_{\max}$ of a band-limited blackbody source a distance r from the sun may be expressed

$$I_0 = \frac{R_S^2}{r^2} \int_{\nu_{\min}}^{\nu_{\max}} \tilde{I}(\nu)d\nu = \frac{R_S^2}{r^2}\frac{2\pi h}{c^2} \int_{\nu_{\min}}^{\nu_{\max}} \frac{\nu^3\ d\nu}{\exp(h\nu/k_B T) - 1} \tag{6.1}$$

where $R_S = 6.957 \times 10^8$ [m] is the solar radius, $h = 6.626 \times 10^{-34}[\text{J}\cdot\text{s}]$ is the Planck constant, $k_B = 1.381 \times 10^{-23}[\text{J/K}]$ is the Boltzmann constant, and we assign $T = 5770.2$ as the effective absolute temperature of the sun. Below we assume r
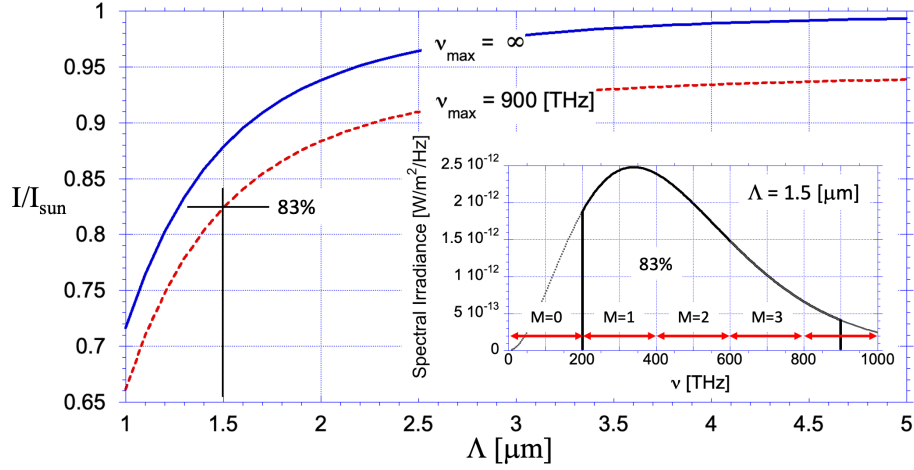
Figure 6.2: Fraction of integrated solar black body spectral irradiance for the range $\nu_{min} = c/\Lambda$ to ν_{max}, where $I_{sun} = 1360$ [W/m^2]. Insert: Black body spectral irradiance with range $\nu_{min} = 200$ [THz] ($\Lambda = 1.5$ [μm]) and $\nu_{max} = 900$ [THz] ($0.83 I_{sun}$). Arrows: Range of maximum mode number M.

corresponds to 1 [AU]. The case $\nu_{min,max} = 0, \infty$ corresponds to the so-called solar-constant, $I_{sun} = 1360$ [W/m^2]. Values of I_0 are plotted in Fig. 6.2 as a function of the grating period for $\nu_{min} = \tilde{\nu} = c/\Lambda$ and two different values of ν_{max}: ∞ (blue line) and 900 [THz] (red line). The case used for our FDTD model, $\lambda_{min} = 0.333$ [μm] and $\lambda_{max} = \Lambda = 1.5$ [μm] ($\nu_{min} = 200$ [THz], and $\nu_{max} = 900$ [THz]) includes up to four diffraction orders and spans 83% of the solar spectrum. Although wider bandwidths are of interest, FDTD run times become prohibitively long.

Following Ref [58] the net radiation pressure force on the sail owing to a band-limited source may be expressed

$$\vec{F}^{s,p} = \frac{A}{c} \int_{\nu_{\min}}^{\nu_{\max}} \sum_{m=M_\nu^-}^{M_\nu^+} \tilde{I}_m^{s,p}(\nu) \left((1 - \cos\theta_m)\, \hat{z} - \sin\theta_m\, \hat{x} \right) d\nu \qquad (6.2)$$

where $\tilde{I}_m^s(\nu)$ and $\tilde{I}_m^p(\nu)$ respectively correspond to the value of the spectral irradiance scattered into the mth diffraction order for the s and p polarization states, and where θ_m depends on frequency owing to the grating equation which may be expressed, $\sin\theta_m = mc/\nu\Lambda$. The frequency-dependent cut-off mode numbers at the normal
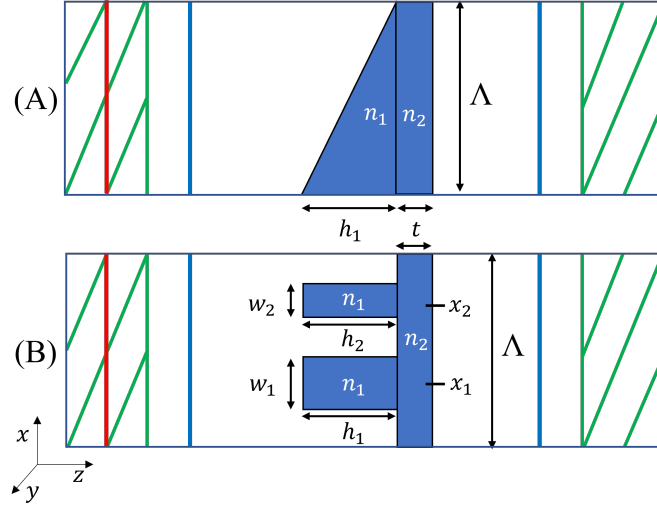
Figure 6.3:   FDTD Schematic: Unit cell of period Λ of (A) prism and (B) meta gratings with plane wave source (red line), field monitors (blue lines), and perfectly absorbing boundary layers (green areas).

incident are given by $M_\nu^\pm = \pm\mathrm{INT}[\nu/\tilde{\nu}]$ (or equivalently $\pm\mathrm{INT}[\Lambda/\lambda]$) where INT represents the integer value of the argument rounded toward zero. In a lossless system having no guided surface waves that extend to infinity, we expect

$$\tilde{I}(\nu) = \sum_{m=M_\nu^-}^{M_\nu^+} \left(\tilde{I}_m^s(\nu) + \tilde{I}_m^p(\nu) \right) \tag{6.3}$$

In general $\tilde{I}_m^s(\nu) \neq \tilde{I}_m^p(\nu)$ owing to polarization-dependent scattering.

The Maxwell stress tensor $\overline{\overline{T}}_\nu$ may be evaluated at each frequency as an alternative method to evaluate the net force $\vec{F}$:

$$\vec{F}^{s,p} = \int_{\nu_{\min}}^{\nu_{\max}} \vec{F}_\nu^{s,p} d\nu = \int_{\nu_{\min}}^{\nu_{\max}} \left(\oint_S \overline{\overline{T}}_{\nu,ij}^{s,p} \cdot d\vec{S} \right) d\nu \tag{6.4}$$

where S is an arbitrary surface enclosing the sail, $\mathrm{d}\vec{S}$ is the elemental area vector and

$$\overline{\overline{T}}_{\nu,ij}^{s,p} = \epsilon_0(E_{\nu,i}^{s,p} E_{\nu,j}^{s,p} - \frac{1}{2}|E_\nu^{s,p}|^2\delta_{ij}) + \frac{1}{\mu_0}(B_{\nu,i}^{s,p} B_{\nu,j}^{s,p} - \frac{1}{2}|B_\nu^{s,p}|^2\delta_{ij}) \tag{6.5}$$

where ϵ_0 and μ_0 are respectively the vacuum permittivity and permeability, E and B are respectively electric and magnetic field amplitudes, and δ_{ij} is the Kronecker delta function. For a structure that is periodic in the plane of incidence as depicted in Fig. 6.3 and extended over a distance L_y out of the plane, the only elemental areas that contribute to (6.4) are $d\vec{S}_{z=\pm z_0} = \pm dx\, dy\, \hat{x} \pm dx\, dy\, \hat{z}$. The force exerted across the area $L_y \times \Lambda$ of an infinitely period grating may therefore be expressed

$$\vec{F}^{s,p} = \int_{\nu_{\min}}^{\nu_{\max}} \left(\int_{\Lambda L_y} \left((\overline{\overline{T}}_{\nu,ij}^{s,p} \cdot d\vec{S})_{z=-z_0} + (\overline{\overline{T}}_{\nu,ij}^{s,p} \cdot d\vec{S})_{z=+z_0} \right) \right) d\nu$$

$$= L_y \int_0^{\Lambda} ((-T_{xx} - T_{zz})_{z=-z_0} + (T_{xx} + T_{zz})_{z=+z_0}) dx \tag{6.6}$$

where z_0 is an arbitrary distance from the grating, and the final integral includes the frequency-integrated stress tensor components T_{xx} and T_{zz}.

We used the open source FDTD numerical solver MEEP [46] to solve Eq.s (6.4) - (6.6), making use of fast built-in "methods" like `ForceSpectra` to calculate forces in a specified `ForceRegion`. To cross-validate the force values we randomly compared them to values obtained using Eq.(6.2), this time using diffraction mode options in MEEP. In both cases, Bloch periodic boundary conditions were employed. The power spectrum of a broadband source in MEEP is defined as the distribution function `GaussianSource(fcen, fwidth)` where `fcen` and `fwidth` are respectively the center and width of the Gaussian distribution. Force calculations are made in the frequency domain and we scaled them to correspond to the solar blackbody spectral irradiance. The red line in Fig. 6.3 depicts a planar light source propagating in the $\hat{z}$ direction. The blue lines represent so-called monitors where the electromagnetic fields $\vec{E}_\nu^{s,p}$ and $\vec{B}_\nu^{s,p}$ are evaluated for the determination of the Maxwell stress tensor, and where alternatively the spectral irradiance $\tilde{I}_m^{s,p}(\nu)$ may be determined to evaluate Eq. (6.2).

Note that, MEEP normalizes the source such that the power $P(\nu) = 1$ i.e., it assumes unit power across frequencies. An unpolarized light is 50 percent s and 50 percent $p-$polarized. Since we inject either one of the polarized source in a given simulation, the output $\tilde{I}_m^{s,p}$ must be multiplied by 0.5 such that $I^s = I^p = 0.5 I_0$. In other words, the total forces on the sail is the average of forces calculated for each polarization.

The green lines in Fig. 6.3 represent perfectly matched layers. The square numerical grid elements were set to $\delta x = \delta z = 20$ [nm]. The simulation ran until

either E_z or H_z decayed to 10^{-6} of the peak value.

The focus of this study was to determine optimized parameters of the two structures depicted in Fig. 6.3, both having the same period $\Lambda = 1.5$ [μm]: (A) a prismatic grating and substrate having four optimization parameters n_1, n_2, h_1, and t; and (B) a metasurface comprised of two pillars and a substrate having nine optimization parameters n_1, n_2, h_1, h_2, w_1, w_2, x_1, x_2, and t. We employed a multi-objective optimizer NSGA-II (with 40 agents, 40 offspring, 150 generations) [20] with the range of parameter values listed in Table 6.1. The objectives are to achieve the largest values of transverse force for both polarizations and to minimize the mass. A representative set of 40 solutions (called Pareto-optimal) were obtained. The same procedure was followed for silicon nitride ($n_{\mathrm{Si_3N_4}}$) structures, but in this case $n_1 = n_2$ and $h_1 = h_2$. Silicon nitride is relatively stable in a space environment, its optical properties are well characterized, and its lithographic fabrication techniques are mature. The refractive index $n_{\mathrm{Si_3N_4}}$ varies from ~ 2.00 at 200 [THz] to ~ 2.15 at 900 [THz] [39]:

$$n_{\mathrm{Si_3N_4}}^2 - 1 = \frac{3.0249\lambda^2}{\lambda^2 - 0.1353406^2} + \frac{40314\lambda^2}{\lambda^2 - 1239.842^2} \tag{6.7}$$

A solar sail is typically used to achieve a spiral trajectory toward or away from the sun. In this case, the flight time may be minimized when the transverse (lift) component of acceleration F_x/M_{sc} is a maximum, where $M_{sc} = m_{\mathrm{sail}} + m_{\mathrm{pl}}$ is the total mass of the sailcraft, m_{sail} is the mass of the diffractive sail material, m_{pl} is the mass of the payload and structural support mechanisms, and $F_x = F_x^s + F_x^p$. The transverse acceleration is optimized when both F_x^s and F_x^p are maximized and m_{sail}

Table 6.1: Multi-Objective Optimization Scheme: Nine variables, three objectives, and four constraints.

$\mathbf{x} \in$	$[x_{1,2}, w_{1,2}, h_{1,2}, n_{1,2}, t]$
max :	$F_x^s(\mathbf{x}),\ F_x^p(\mathbf{x})$
min :	$\mathrm{mass}(\mathbf{x})$
such that :	$1.5 \leq n_{1,2} \leq 3.5$
such that :	$-\Lambda/2 \leq x_{1,2} \leq \Lambda/2$
such that :	$0 \leq w_{1,2}, h_{1,2} \leq \Lambda$
such that :	$0.1\mu m \leq t \leq 0.5\mu m$

is minimized. The sail mass of our two designs may be expressed

$$m_{\text{sail}}^{\text{prism}} = \left(\frac{1}{2}\rho_1 h + \rho_2 t\right) N_x^2 \Lambda^2 = \left(\frac{1}{2}\rho_1 h + \rho_2 t\right) A \tag{6.8a}$$

$$\begin{aligned} m_{\text{sail}}^{\text{meta}} &= \rho_1(N_x w_1 h_1 + N_x w_2 h_2)N_x \Lambda + \rho_2 N_x^2 \Lambda^2 t \\ &= (\rho_1 w_1 h_1/\Lambda + \rho_1 w_2 h_2/\Lambda + \rho_2 t)\, A \end{aligned} \tag{6.8b}$$

where N_x is the number of grating periods across the sail, and A is the area of a square sail. Ignoring the payload mass ($m_{pl} = 0$) and writing the transverse component of force $F_x = I_0 A \eta_x/c = m_{\text{sail}} a_x$ we obtain the transverse acceleration for our unladen structures:

$$a_x^{\text{prism}} = \frac{I_0}{\alpha c} \frac{\eta_x}{\frac{1}{2}n_1 h + n_2 t} \tag{6.9a}$$

$$a_x^{\text{meta}} = \frac{I_0}{\alpha c} \frac{\eta_x}{n_1(w_1 \mathsf{f}_1 + w_2 \mathsf{f}_2) + n_2 t} \tag{6.9b}$$

where $\mathsf{f}_{1,2} = h_{1,2}/\Lambda$ is the fill factor, and for convenience we associate the refractive index and mass density with a proportionality factor α: $\rho_{1,2} \equiv \alpha n_{1,2}$. Using the space qualified polyimide material CP1 [44] as an example, with a specific gravity s.g. = 1.54 and a mean refractive index of 1.57 we obtain $\alpha = 0.98 \times 10^3$ [kg/m^3]. For our silicon nitride structures we instead combine its specific gravity, s.g. = 3.17 [30] with the mean index, 2.02, to obtain $\alpha = 1.57 \times 10^3$ [kg/m^3]. As seen in Eq. 6.9 the transverse acceleration is independent of the sail area and is implicitly dependent on the grating period Λ via the efficiency factor η_x (which is found by numerically determining the transverse force F_x value).

6.3   Results & Analysis

Forty representative Pareto-optimal solutions are plotted in Fig.6.4 for the two gratings having nine arbitrary parameters (A) and (B), and for the two gratings comprised of Si$_3$N$_4$ (C) and (D). The net transverse radiation pressure force F_x is plotted against the total mass of the sail, m_{sail}. In all cases a trend in the data appears: Higher mass sails provide higher forces. To select the most optimal design for each structure we use the greatest value of the transverse acceleration $a_x = F_x/m_{\text{sail}}$ as

the deciding factor (see straight line in Fig.6.4). The parameters for the Pareto-optimal solution that intersects this line are tabulated in Table 6.2 for the four different cases.

We find that both the prismatic and metasurface structures having arbitrary refractive indexes are able to produce large values of F_x, as is evident in Fig.6.4 for Case A and Case B. However, owing to the lower mass of the metasurface structure, its optimal acceleration $a_x = 1080$ [$\mu m/s^2$] is 48% greater than that of the prism grating. The Si_3N_4 structures, Case C and Case D, depict significantly less values of optimized acceleration. These values may be compared with a conventional aluminized polyimide sail [42] which is roughly 3 [μm] thick and achieves a momentum transfer efficiency of roughly 90% of the ideal value of 0.77 : $a_x = 680$ [$\mu m/s^2$]. This comparison suggests that an optimized metasurface sail is a competitive alternative to a conventional reflective sail. However, amongst the many unknown fabrication, packaging, unfurling, and space weathering issues is whether a large robust metasurface grating can be fabricated on a thin (< 1 [μm])substrate [1].

To better understand the spectral force characteristics of the four sails examined in this study, we plot the transverse spectral force distribution $F_{\nu,x} = F_{\nu,x}^s + F_{\nu,x}^p$ in Fig. 6.5. The blue line represents the FDTD-obtained values corresponding to the Maxwell stress tensor calculations, whereas the circles represent the values corresponding to our FDTD modal analysis. The excellent agreement between these two approaches provides a level of cross-validation of the methods. Fluctuations of the value of $F_{\nu,x}$ are indicative of pronounced diffractive variations of the transmitted and reflected light at different optical frequencies, as expected for a small period grating [57]. Also plotted in Fig. 6.5 are theoretical values of force for the ideal limit $\eta_x = 1$ (black line) and the ideal reflective sail $\eta_x = 0.77$ (red line): $F_{x,\nu} = \eta_x \tilde{I} \nu A/c$. These results suggest that the diffractive sails explored in this study may equal or exceed the acceleration of a reflective sail only if there is a small-mass advantage of the former. The prism and pillar designs suffer from the effects of external and internal reflections which can scatter light that opposes the desired transverse scattering direction. For example front surface reflections from the prism in Fig. 6.3 (A) have positive values of k_x which oppose the transmitted (refracted) rays. Those reflected rays carry 17% of incident beam power owing to Fresnel reflections. Less than two thirds of the incident radiation is refracted out the back surface owing to internal reflections and shadowing effects from the steep side facets. It is yet unknown whether the added mass of anti-reflection coatings would provide increased the transverse acceleration. Other unknowns that are beyond the scope
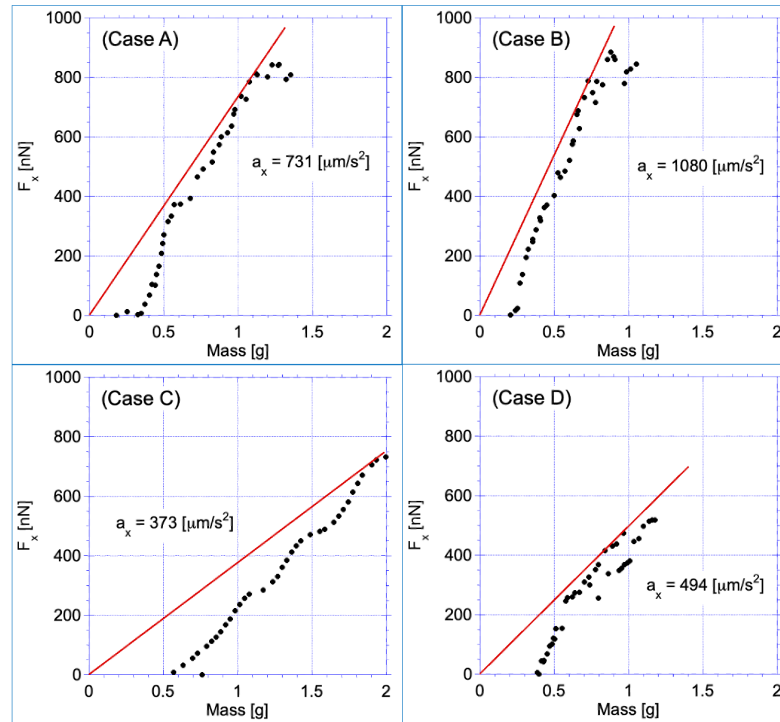
Figure 6.4: Pareto optimal solutions for (A) prismatic and (B) metasurface gratings having arbitrary refractive indexes, and for (C) prismatic and (D) metasurface gratings comprise of silicon nitride. A sun-facing square sail of area $1[\text{m}^2]$ illuminated with a band-limited solar black body is assumed. The optimal transverse acceleration a_x for each case is determined from the slope of the straight line, and the corresponding design parameter values for the intersecting points are given in Table 6.1.

of this paper include the practical limits of assumptions about the rigidity of the sail, the coherence properties of the incident sunlight, and whether the sail can be packaged and unfurled without changing its optical properties.

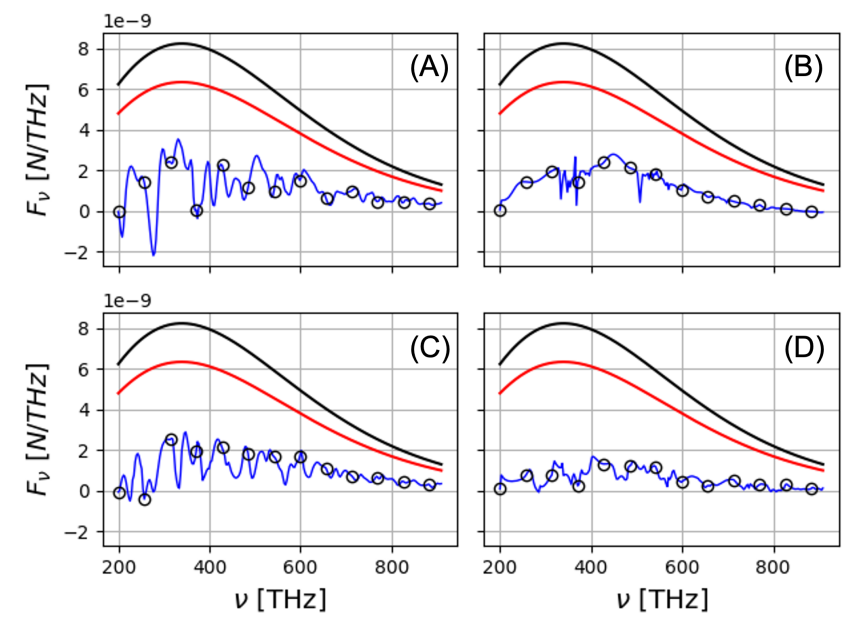Figure 6.5: Spectral transverse force distribution $F_{x,\nu}$ determined from Maxwell stress tensor (blue line) and modal analysis (open circles) for the four cases described in the text, and for an idealized reflective sail (red line) and the upper theoretical bound (black line). An area of 1 m² is assumed.

6.4 Conclusions

We performed FDTD simulations coupled with a NSGA-II multi-objective optimizer to determine design parameters for four different grating structures, each having a period of 1.5 [μm] and a sail area of 1 [m²]. The small grating period was selected to satisfy a small desired mass and a marginal cutoff wavelength of the solar blackbody spectrum. Our optimization study included 3 objectives and up to 9 variables, as well as both s and p polarization. The transverse component of radiation pressure force was determined for a truncated solar black body radiator (200-900 [THz] or equivalently, 0.33 to 1.5[μm]) at 1 [AU] for the purpose of two-orbit changing maneuvers in space. An optimized metasurface grating comprised of two pillars per period was found to provide 48% more transverse acceleration than an optimized prism grating owing to the small mass of the former grating. We found that Silicon

Nitride did not perform well for either the prism or two-pillar metasurface design. Although none of the structures provided radiation pressure force values exceeding those of an ideal flat reflective sail, the diffractive sail may nevertheless provide an acceleration advantage if the proposed sun-facing diffractive sail spacecraft has a total lower mass than a reflective sailcraft. The design of alternatives to flat reflective sails is an emerging area of research and we therefore believe continued exploration of diffractive designs such as hybrid reflective/transmissive structures will provide more efficient solar sails in the future.

Table 6.2: Optimized parameters and cost function values for (A) prism and (B) meta gratings of arbitrary dispersionless materials, and (C) prism and (D) meta gratings for Si_3N_4, each with period $\Lambda = 1.5[\mu m]$, $L_y = 1$ [m], $L_x = N\Lambda = 1$ [m], $A = L_x L_y$.

Parameters	A	B	C	D
$h_1[\mu m]$	0.76	1.12	1.02	0.62
$h_2[\mu m]$	-	1.26	-	h_1
$w_1[\mu m]$	-	0.32	-	0.16
$w_2[\mu m]$	-	0.16	-	0.24
$x_1[\mu m]$	-	0.06	-	0.38
$x_2[\mu m]$	-	0.44	-	0.1
Prism Angle	26.9°	-	34.2°	-
n_1	2.43	1.55	Si_3N_4	Si_3N_4
n_2	1.5	1.5	Si_3N_4	Si_3N_4
$t[\mu m]$	0.1	0.1	0.1	0.11
Force [nN]	785	787	722	416
mass [$\times 10^{-3}$ kg]	1.07	0.73	1.93	0.84
a_x [$\mu m/s^2$]	731	1080	373	494

Chapter 7

Future Work

Building upon the contributions of this thesis, we identify promising directions to advance our understanding and explore practical applications. By addressing existing limitations and delving deeper into the complexities of Diffractive Light & Solar Sails, we aim to inspire researchers and practitioners to pursue novel investigations that benefits academia and space exploration industry alike. Some of the potential avenues for future research are

7.1   Non-Rigid Sail

The study of rigid body dynamics provides a foundational framework for comprehending the motion of sails. However, in real-world scenarios, sails experience deformations and vibrations that significantly influence their dynamics. Ignoring these deformations can lead to inaccurate predictions and compromised designs. To address this, it becomes imperative to model sails as non-rigid or deformable structures to capture the complexities they exhibit. By employing non-rigid body dynamics, we can accurately model these deformations, which plays a vital role in predicting fatigue, stress distribution, and the overall performance of the sail system over time. This understanding is essential to ensure the longevity and optimal functionality of sails in various sailing applications

7.2 Curved Light Sails

In recent research[12], there is growing evidence suggesting that a curved sail design may offer the most optimal performance. While planar metasurfaces have been a common choice, an intriguing alternative lies in conformal metasurfaces[64]. These structures possess a unique characteristic – the ability to seamlessly integrate onto non-planar and curved surfaces, enabling them to conform perfectly to the underlying substrate or object. This distinctive feature makes conformal metasurfaces stand out as a compelling option for our application. Moreover, their seamless integration allows us to incorporate them into the modeling of non-rigid sail dynamics, accounting for deformations that may arise during operation. Integrating these advanced metasurfaces will pave the way for ground-breaking solutions.

7.3 Spin-Stabilized Sail

The concept of a flat disc-shaped light sail holds numerous advantages over a square-shaped sail, making it a promising choice for various reasons. Its spinning nature allows for simplified deployment through spin induced centrifugal force, providing tension to maintain a flat shape without requiring additional structural support or added mass. Moreover, strategically offsetting the center of pressure and center of mass induces precession, enabling precise attitude control, which is crucial for maneuverability in space. However, modeling a non-rigid spinning metasurface sail presents significant challenges, necessitating the development of new tools for faster and more accurate simulations. Overcoming these hurdles will unlock the full potential of spinning light sails, advancing space exploration and transportation capabilities.

7.4 Achromatic Liquid Crystal Gratings

Liquid crystal polarization grating exhibits promising characteristics, including nearly 100 percent diffraction efficiency in the first order, making it an attractive candidate for this application. The key to its achromatic design lies in a clever implementation: a stack of two chiral polarization gratings with opposite twist senses, leveraging the principle of retardation compensation. By strategically optimizing the thickness, birefringence, and nematic director angles of such gratings, we can achieve tailored

achromatic properties across the visible, infrared, and ultra-violet wavelengths, resulting in maximum force generation across the entire solar spectrum. This novel approach holds significant potential for enhancing solar sail performance and is a subject of exploration.

7.5 Contactless Optical Manipulation

The developed approach for manipulating a bi-grating sail demonstrates excellent scalability, making it versatile for controlling objects ranging from millimeter to meter scales, all without the requirement to focus incident light. This scalability opens up a plethora of exciting applications, such as precise control of miniature robots in complex biological fluids, contactless wafer-scale fabrication, and assembly processes, as well as novel space propulsion systems. The potential impact of this approach extends across diverse fields, promising groundbreaking advancements in robotics, nanotechnology, manufacturing, and space exploration.

Chapter 8

Publications

8.1 Journal Publications

[1] **Srivastava, Prateek R.**, Ying-Ju Lucy Chu, and Grover A. Swartzlander. "Stable diffractive beam rider." Optics letters 44, no. 12 (2019): 3082-3085.

[2] **Srivastava, Prateek R.**, and Grover A. Swartzlander. "Optomechanics of a stable diffractive axicon light sail." The European Physical Journal Plus 135, no. 7 (2020): 1-16.

[3] Chu, Ying-Ju Lucy, Monjurul Meem, **Prateek R. Srivastava**, Rajesh Menon, and Grover A. Swartzlander. "Parametric control of a diffractive axicon beam rider." Optics Letters 46, no. 20 (2021): 5141-5144.

8.2 arXiv Preprints

[1] **Srivastava, Prateek R.**, Apratim Majumdar, Rajesh Menon, and Grover A. Swartzlander Jr. "High Forward Thrust Metasurface Beam-Riding Sail." arXiv preprint arXiv:2303.06793 (2023).

[2] **Srivastava, Prateek R.**, Ryan M. Crum, and Grover A. Swartzlander Jr. "Broadband Diffractive Solar Sail." arXiv preprint arXiv:2306.14093 (2023).

8.3   Conference Publications

[1] Swartzlander, Grover A., Ying-Ju Lucy Chu, and **Prateek R. Srivastava**. "Beam riders and sailcraft based on diffractive light sails." In Laser Science, pp. JTu2A-37. Optica Publishing Group, 2018.

[2] Chu, Ying-Ju Lucy, **Prateek R. Srivastava**, Monjurul Meem, Rajesh Menon, Nelson Tabiryan, and Grover A. Swartzlander Jr. "Radiation pressure on bi-grating and axicon diffractive beam-riding light sails." In Optical Trapping and Optical Micromanipulation XVIII, vol. 11798, pp. 91-94. SPIE, 2021.

[3] Swartzlander, Grover, Ying-Ju Lucy Chu, **Prateek Srivastava**, Les Johnson, Nelson Tabiryan, Seongsin Margaret Kim, and Rajesh Menon. "Thin Diffractive Optics for In-Space Propulsion and Attitude Control Via Radiation Pressure." In Flat Optics: Components to Systems, pp. FTh3C-4. Optica Publishing Group, 2021.

[4] Peng, Xiaopeng, **Prateek R. Srivastava**, and Grover A. Swartzlander. "CNN-based Real-time Image Restoration in Laser Suppression Imaging." In Applied Industrial Spectroscopy, pp. JTh6A-10. Optica Publishing Group, 2021.

[5] Swartzlander, Grover A., **Prateek R. Srivastava**, and Ryan M. Crum. "Performance Advantages and Design Challenges of Diffractive Solar Sails." In Laser Science, pp. JW5A-7. Optica Publishing Group, 2022.

Appendix A: Broadband Imaging with Phase Mask

The half-right PSF developed to protect an imaging sensor from laser dazzle or damage has only been optimized for a single wavelength. In practice, neither the scene nor the imaging sensor is just limited to a single wavelength and hence requires an optimization in the broadband regime to correct for chromatic aberration. We explored the impact of wavelength on PSF and possible artifacts introduced by the imaging sensor due to the Bayer filter.

Coherent & Incoherent Imaging Theory

The formation of image of an object in the image plane can be modeled using the principles of Fourier optics. The object lies in the plane with spatial coordinates (ξ, η) plane and the image is observed in the sensor array plane with the coordinates (u, v). We consider a singlet optical system with lens and phase mask at a distance z_{XP} from the sensor plane, with spatial coordinates (x, y). The schematics of the imaging system is shown in Fig.8.1.

Coherent Imaging Theory

An imaging system with coherent illumination allows us to perform mathematical operations on optical *field*. Let $U_o(x, y, \lambda)$ be the object field, then the ideal geometric field $U_g(u, v, \lambda)$ can be expressed as a scaled copy of object field:

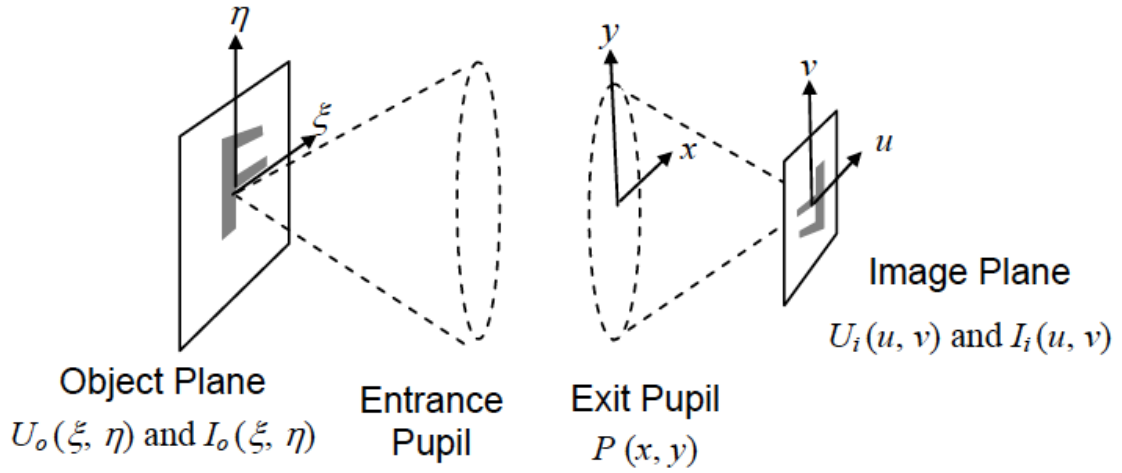$$U_g(u, v, \lambda) = \frac{1}{|M|} U_o\left(\frac{u}{M}, \frac{v}{M}, \lambda\right) \tag{8.1}$$

Figure 8.1: Imaging system coordinates. (Picture credit: [62])

where M accounts for the magnification. For a negative M, the image will appear inverted relative to the object. The ideal geometric image is "blurred" by the imaging system because of the convolution operation described by

$$U_i(u, v, \lambda) = h(u, v, \lambda) \circledast U_g(u, v, \lambda) \tag{8.2}$$

where $h(u, v, \lambda)$ is the *coherent impulse response* or *point spread function* (PSF) of the system, assuming a *linear shift-invariant* imaging system. In the frequency domain, the Eq.8.2 may be expressed as

$$G_i(f_u, f_v, \lambda) = H(f_u, f_v, \lambda)G_g(f_u, f_v, \lambda) \tag{8.3}$$

where spatial frequency coordinates and spatial coordinates are related to each other as follows

$$f_u \to \frac{x}{\lambda z_{XP}}, \quad \text{and} \quad f_v \to \frac{y}{\lambda z_{XP}} \tag{8.4}$$

and $H(f_u, f_v, \lambda)$ is the *coherent amplitude transfer function* or ATF and is defined as

$$H(f_u, f_v, \lambda) = P(x, y) = P(-\lambda z_{XP} f_u, -\lambda z_{XP} f_v, \lambda) \tag{8.5}$$

where P is the exit pupil function as we are dealing with image plane. Clearly, the pupil is a function of wavelength λ and the negative sign accounts for the inversion

of ideal geometric image. In general, the pupil function is circular and may be expressed

$$P(x,y) = circ\left(\frac{\sqrt{x^2 + y^2}}{w_{xp}}\right) \tag{8.6}$$

where $w_{XP} = D_{XP}/2$ and D_{XP} is the lens and phase mask diameter. The ATF is

$$H(f_u, f_v, \lambda) = circ\left(\frac{\sqrt{(\lambda z_{XP} f_u)^2 + (\lambda z_{XP} f_v)^2}}{w_{XP}}\right) \tag{8.7}$$

or

$$H(f_u, f_v, \lambda) = circ\left(\frac{\sqrt{f_u^2 + f_v^2}}{f_o}\right) \tag{8.8}$$

where f_o is the *coherent cut-off frequency* defined by

$$f_o = \frac{w_{XP}}{\lambda z_{XP}} \tag{8.9}$$

If a coherent image is to be observed, the irradiance $I_i = |U_i|^2$ is what is recorded on the sensor. As a result, the irradiance image can gain *twice* the frequency content and the cut-off frequency is

$$2f_o = \frac{2w_{XP}}{\lambda z_{XP}} = \frac{1}{\lambda f/\#} \tag{8.10}$$

Incoherent Imaging Theory

The imaging theory discussed in the previous section is only true in an ideal case. In an ideal case, the scene is illuminated by source with a spectrum of wavelengths with rapidly changing phase. Thus, what is observed at the sensor is the *time-average squared magnitude* of the field. For an incoherent illuminated scene, the response of the imaging system may be expressed

$$I_i(u, v, \lambda) = |h(u, v, \lambda)|^2 \circledast I_g(u, v, \lambda) \tag{8.11}$$

where $|h(u,v)|^2$ is the *incoherent* PSF and I_g is the geometric irradiance image

$$I_g(u, v, \lambda) = \frac{1}{|M|} I_o\left(\frac{u}{M}, \frac{v}{M}, \lambda\right) \tag{8.12}$$

In the frequency domain, Eq.8.11 may be expressed

$$\mathcal{G}_i(f_u, f_v, \lambda) = \mathcal{H}(f_u, f_v, \lambda)\mathcal{G}_g(f_u, f_v, \lambda) \tag{8.13}$$

where $\mathcal{H}$ is the *optical transfer function* or OTF. Conventionally, the OTF is normalized as follows

$$\mathcal{H}(f_u, f_v, \lambda) = \frac{\mathscr{F}\{|h(u, v, \lambda)|^2\}}{\overset{+\infty}{\underset{-\infty}{\iint}}|h(u, v, \lambda)|^2 du dv} \tag{8.14}$$

The normalization scales the OTF such that it has a value of 1 at the DC frequency $(f_u, f_v) = 0$, since OTF is not supposed to affect the total optical power in ideal geometric image.

Broadband Imaging Theory

When an object or scene is illuminated by a broadband light source, it radiates wavelengths all the wavelengths simultaneously. Thus, a broadband object scene $I_o(\lambda)$ is created. To produce a multiwavelength full color image, three color RGB components are required at each pixel. This can be achieved by a single CMOS sensor fitted with a patterned color filter array (CFA) in mosaiced form (e.g., Bayer pattern). Each filter enables a pixel to register light of a specific color. The pixels are finally demosaiced to produce 3 different channels of an RGB image. To emulate the spectral response of a human eye, wavelength range $\Lambda \in [400, 690]$ nm is assumed. The spectral response of a conventional Bayer CFA comes very close to the response of an average human eye. Assuming the transmittance $T_c(\lambda)$ of a Bayer CFA, where $c \in \{r, g, b\}$ channel. The intensity registered in the c channel is the integration of monochromatic intensities $I_o(\lambda)$ over the wavelength range Λ with the weights $T_c(\lambda)$

$$I_{g,c}(u, v) = \frac{1}{|M|}I_{o,c}\left(\frac{u}{M}, \frac{v}{M}\right) = \int_\Lambda I_o\left(\frac{u}{M}, \frac{v}{M}, \lambda\right)T_c(\lambda)d\lambda \tag{8.15}$$

Thus, a multi-spectral broadband image is reduced to three channel RGB image.

Numerical Simulations

To simulate broadband imaging with and without phase mask, we tried to emulate the entire imaging chain as much as possible, starting from hyperspectral images to

mosaicing-demosaicing due to Bayer CFA on the sensor. In the following sections, the simulation procedure is described in the order of light reflected from a natural scene to finally being sensed by the sensor.

Broadband RGB Image

To simulate an ideal RGB image of a natural scene, we use multispectral AVIRIS (Airborne Visible Infrared Imaging Spectrometer (AVIRIS) images from NASA [1]. We selected the free of charge Moffett Field data and extracted 30 channels in the range $\Lambda \in [400, 690]$ nm with the wavelength step $\delta\lambda = 10$ nm. As an example, the images from 30 channels, $I_o(\lambda)$, are shown in Fig.8.2 (a). Using the transmittance $T_c(\lambda)$ of a Bayer CFA in Sony NEX5N CMOS sensor is shown in Fig.8.2 (b), a ground-truth 'ideal' RGB image is reconstructed using Eq.8.15 and is shown in Fig.8.2 (c), where we assume $M = 1$. Note that, the weights $T_c(\lambda)$ are normalized such that $\int_\Lambda T_c(\lambda)d\lambda = 1$.

Broadband RGB Image with Phase Mask

To simulate an 'ideal' RGB image blurred by the phase mask, we consider an imaging system comprised of a generalized pupil function

$$P(x, y, \lambda) = P_A(x, y,)t_A(x, y, \lambda) = circ\left(\frac{\sqrt{x^2 + y^2}}{w_{XP}}\right) exp(j\varphi(x, y, \lambda)) \qquad (8.16)$$

where $P_A(x, y)$ is the aperture of optics, $t_A(x, y, \lambda)$ is the complex transmittance screen or phase mask, $\varphi(x, y, \lambda)$ is the phase function like half-axicon or azimuthal-harmonic, and w_{XP} is the width of exit pupil. In this simulation, we assume a half-axicon phase mask expressed by

$$\varphi(x, y) = 20\pi \, \frac{\rho}{R} \, \text{sign}(x) \qquad (8.17)$$

where $(\rho, \theta) \equiv (x, y)$ are the polar coordinates of optical plane of lens and phase mask, R is the radius of aperture, and sign is the signum function. Assuming the phase mask is fabricated by etching an optical material like borosilicate crown glass

---

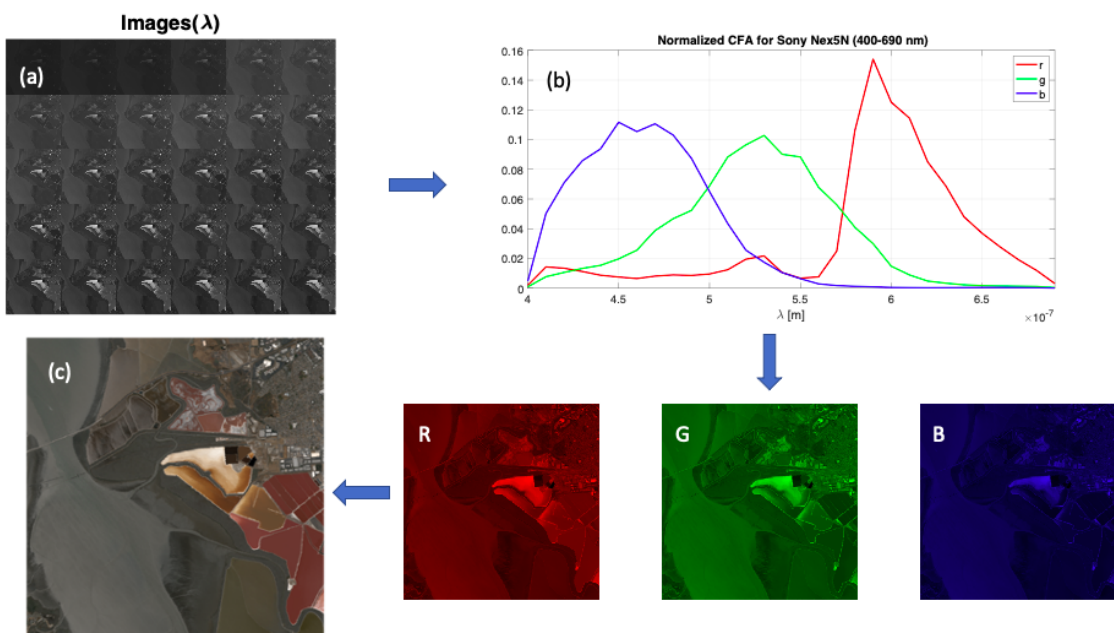[1]https://aviris.jpl.nasa.gov/index.html

Figure 8.2: (a) 30 multispectral images of Moffett Field in the range $\Lambda \in [400, 700]$ nm (b) Spectral Response of the CFA for SONY Nex5N sensor (c) reconsctructed 'ideal' RGB image.

(N-BK7) for the design wavelength λ_o, the phase as a function of wavelength is expressed

$$\varphi(x, y, \lambda) = \varphi(x, y, \lambda_o) \frac{\lambda_o(n(\lambda) - 1)}{\lambda(n(\lambda_o) - 1)} \tag{8.18}$$

where

$$\varphi(x, y, \lambda_o) = 2\pi \frac{d(x, y)}{\lambda_o}(n(\lambda_o) - 1) \tag{8.19}$$

where $d(x, y)$ is the depth of etched glass. The refractive index of the optical material NBK-7 is expressed in terms of Sellemeir dispersion formula

$$n(\lambda)^2 = 1 + \frac{1.03961212\lambda^2}{\lambda^2 - 0.00600069867} + \frac{0.231792344\lambda^2}{\lambda^2 - 0.0200179144} + \frac{1.01046945\lambda^2}{\lambda^2 - 103.560653} \tag{8.20}$$

or alternatively in terms of Cauchy's dispersion formula

$$n(\lambda) = 1.5046 + \frac{0.00420}{\lambda^2} \tag{8.21}$$

where λ is in μm. The coherent PSF of the imaging system as a function of wavelength is now expressed

$$h(u, v, \lambda) = \mathscr{F}\{P(x, y, \lambda)\} \tag{8.22}$$

and the incoherent PSF is $|h(u, v, \lambda)|^2$. As an example, an azimuthal-harmonic and half-axicon phase functions and corresponding coherent PSF is shown in Fig.8.3 and Fig.8.4. Note that, the size of PSF decreases with an increase in wavelength for the azimuthal-harmonic PSF. Whereas, for the half-axicon phase mask, the PSF size remains the same, but the thickness of arc tends to increase with wavelength.

Assuming the wavelength range Λ is discretized into N wavelengths with wavelength steps with step size $d\lambda = \Lambda/N$, the incoherent imaging theory may be extended to the wavelength range as follows

$$I_{s,c}(u, v) = \int_\Lambda |h(u, v, \lambda)|^2 \circledast I_g(u, v, \lambda) \, T_{s,c}(\lambda) \, d\lambda + \epsilon_{s,c} \tag{8.23}$$

where ϵ is the noise and N images corresponding to λ_N are convolved with N PSFs resulting into N blurred images I_s. Shown in Fig.8.5(a) are 30 images convolved with 30 PSFs. The broadband images are narrowed down into three-channel RGB color images on the sensor $I_{s,c}$ by taking into account $T_c(\lambda)$ and summing up over the entire wavelength range Λ, as shown in Fig.8.5(e). Note that, a smaller $d\lambda$ will imply a larger N and a better image reconstruction albeit a longer computation time.
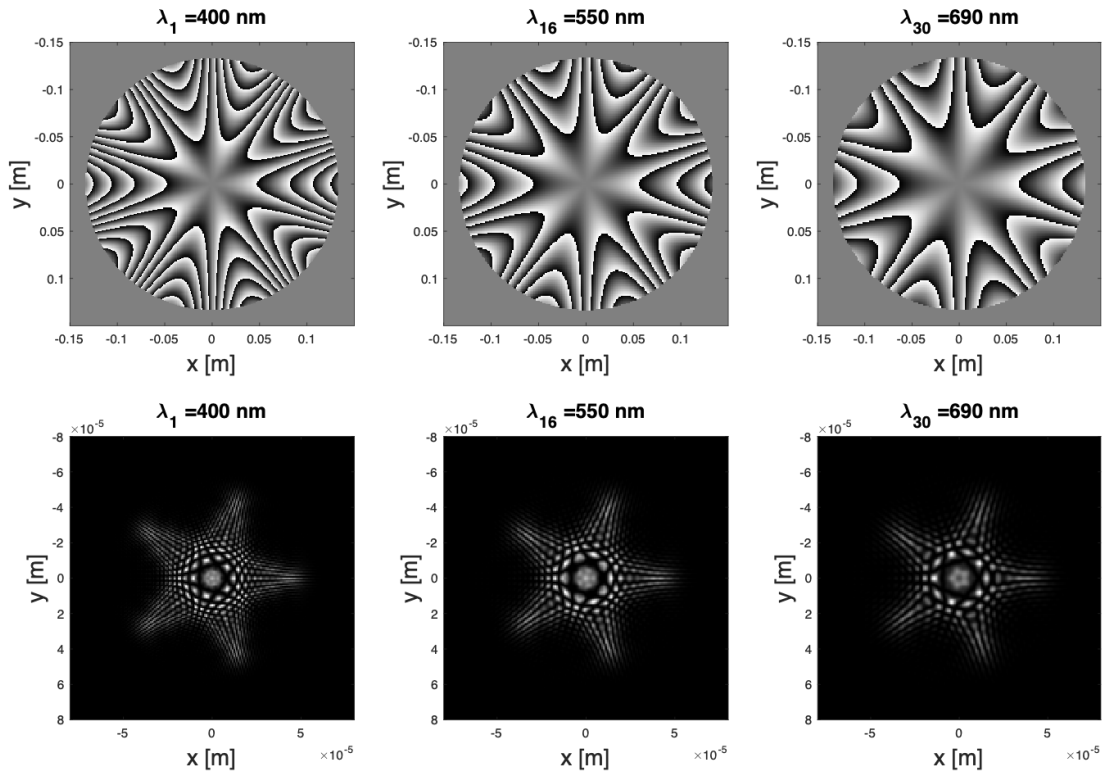
Figure 8.3: Half-axicon Phase Mask and corresponding PSF as a function of wavelength.

Mosaicing-Demosaicing

To render a color image, a three channel RGB image is required. To reduce the cost and complexity, most cameras sensors are fitted with a Bayer filter array. A Bayer filter array is an arrangement of color filters that let each pixel in a single-sensor digital camera subsample and register a *mosaiced* image i.e., record only red, green, or blue data at a time. That is if (u_c, v_c) are the subsampled Bayer encoded output from the sensor for the corresponding channel then $\cup_c u_c = u$, $\cup_c v_c = v$, and $(u_c, v_c) \cap (u_{c'}, v_{c'}) = \varnothing$ for $c \neq c'$. The patterns emphasize the number of green sensors to mimic the human eye's greater sensitivity to green light. To emulate the
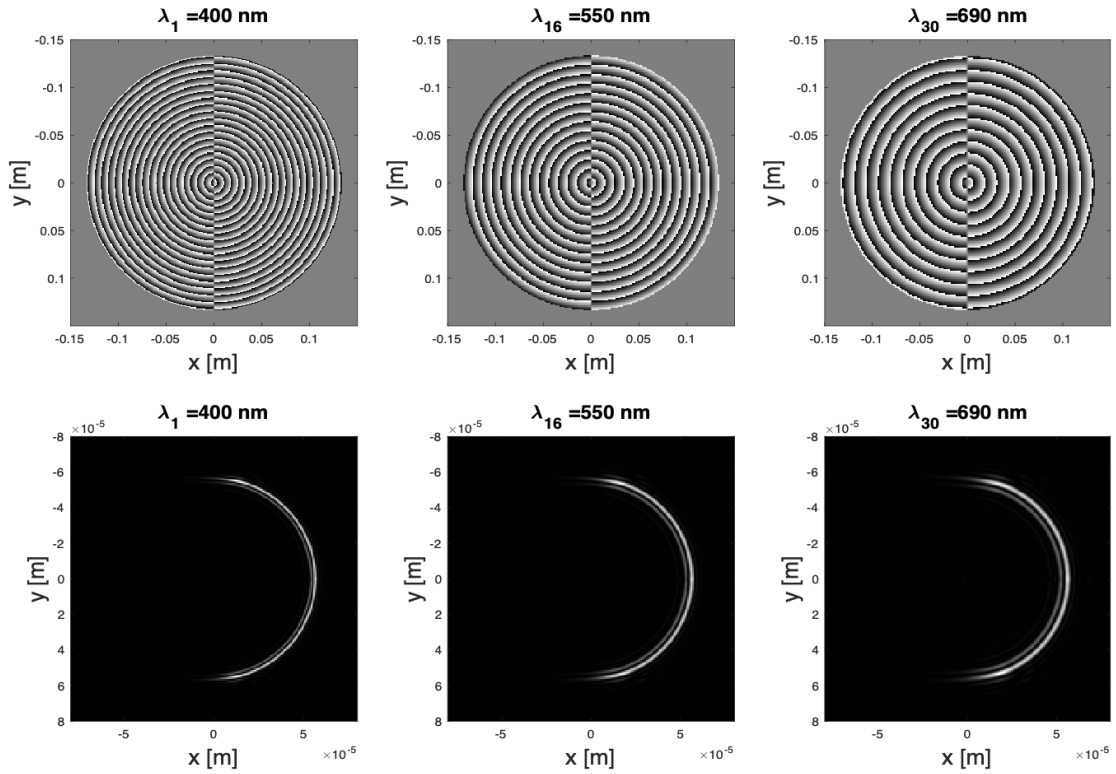
Figure 8.4: Half-axicon Phase Mask and corresponding PSF as a function of wavelength.

behaviour of such an RGB sensor, the blurred image as seen by the sensor is mosaiced and is shown in Fig.8.5(c). Before deblurring, the image is to be *demosaiced* i.e., the Bayer encoded image is to be converted into a truecolor RGB image. In this work, we use the inbuilt MATLAB® function called `demosaic`

$$I_{s,c}(u,v) = \texttt{demosaic}(I_{s,c}(u_c,v_c),\ \texttt{'BayerPattern'}) \tag{8.24}$$

where `demosaic` uses gradient corrected linear-interpolation method [40] to convert the Bayer encoded image $I_{s,c}(u_c,v_c)$ into a truecolor image $I_{s,c}(u,v)$ and the Bayer pattern, say 'RGGB', is specified by `'BayerPattern'`. Hence, the blurred image on the sensor is demosaiced and is shown in Fig.8.5(d).
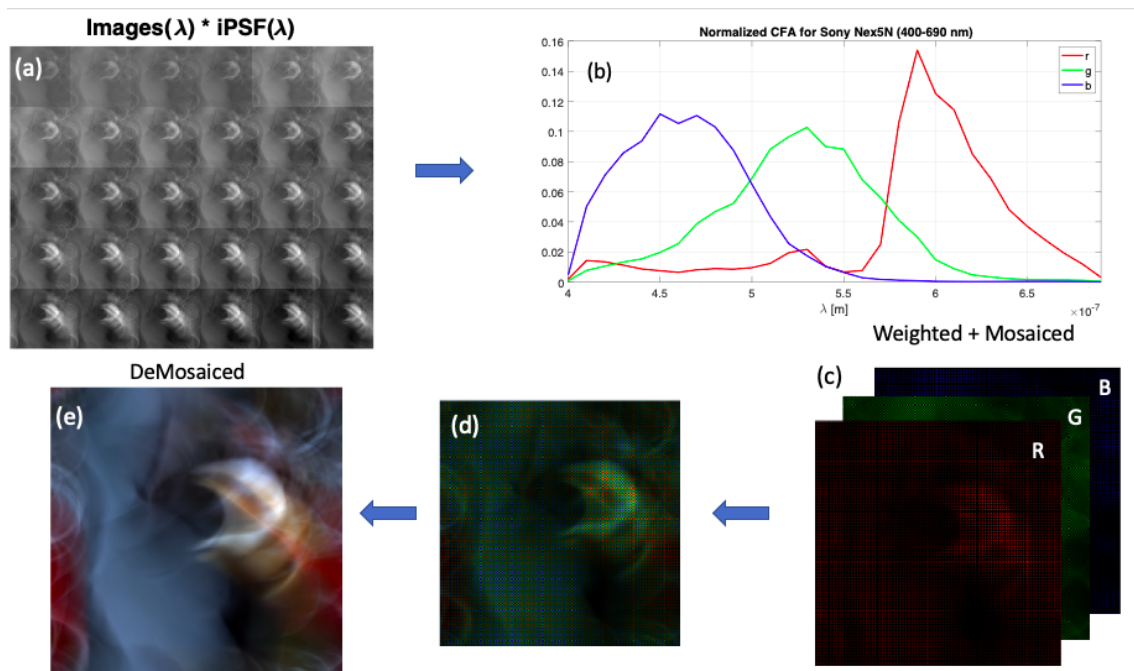
Figure 8.5: (a)Multi-spectral images blurred with PSFs of corresponding wavelengths (b) transmittance of CFA of SONY NEX5N CMOS sensor (c) mosaiced R,G, and B channel as registered by the sensor (d) mosaiced raw image (e) Blurred RGB image after demosaicing
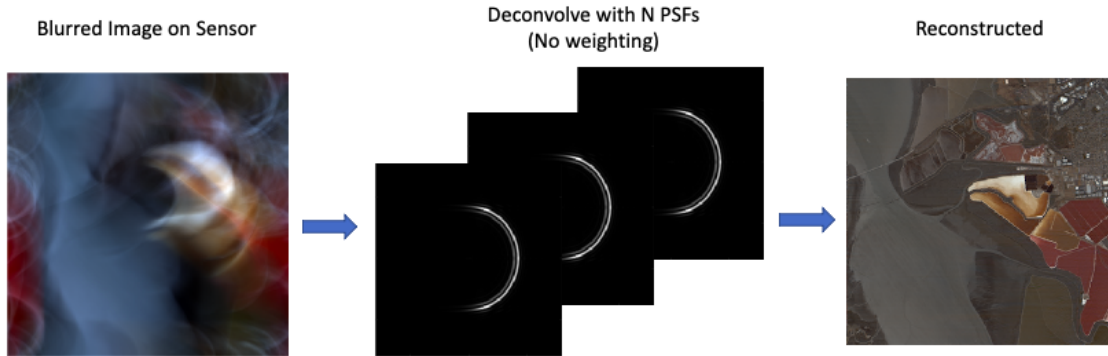
Figure 8.6: Each channel of blurred RGB is deconvolved with N PSFs corresponding to N wavelengths, resulting in N images for each channel. N images for each channel are integrated separately into 3 images, corresponding to RGB channels.

Deblurring the RGB Images

To deblur the three images registered by the sensor, we employed many well-known deconvolution algorithm including but not limited to Weiner, Blind, Lucy-Richardson deconvolution, and Regularized filter. Regularized filter appears to have best performance so far and is employed using the inbuilt MATLAB® function called `deconvreg`

$$I_{i,c}(u, v, \lambda_j) = \texttt{deconvreg}(I_{s,c}(u, v), \ |h(u, v, \lambda_j)|^2) \tag{8.25}$$

which deconvolves the blurred images $I_{s,c}$ in each channel using the regularized filter algorithm, returning N deblurred images $I_{i,c}$ corresponding to each λ_N. The assumption is that the blurred images were created by convolving the true images with PSFs and possibly by adding noise ϵ. The algorithm is a constrained optimum in the sense of least square error between the estimated and the true images under requirement of preserving image smoothness [28]. The scheme is shown in Fig.8.6. .

In the end, the N deblurred broadband images corresponding to each channel are integrated along λ to achieve three narrowband RGB images

$$\tilde{I}_{i,c}(u, v) = \sum_{j=1}^{N} I_{i,c}(u, v, \lambda_j) \tag{8.26}$$

.

A final results comparing the reconstruction of images blurred by (b) Half-axicon and (d)Azimuthal harmonic phase masks, with the (a,c) ground-truth is shown in Fig.8.7. We have used SSIM as a metric to evaluate the reconstruction, which suggests better color and structural reconstruction for half-axicon phase mask. Thus, half-axicon not only offers superior reconstruction but also super color reproduction. .
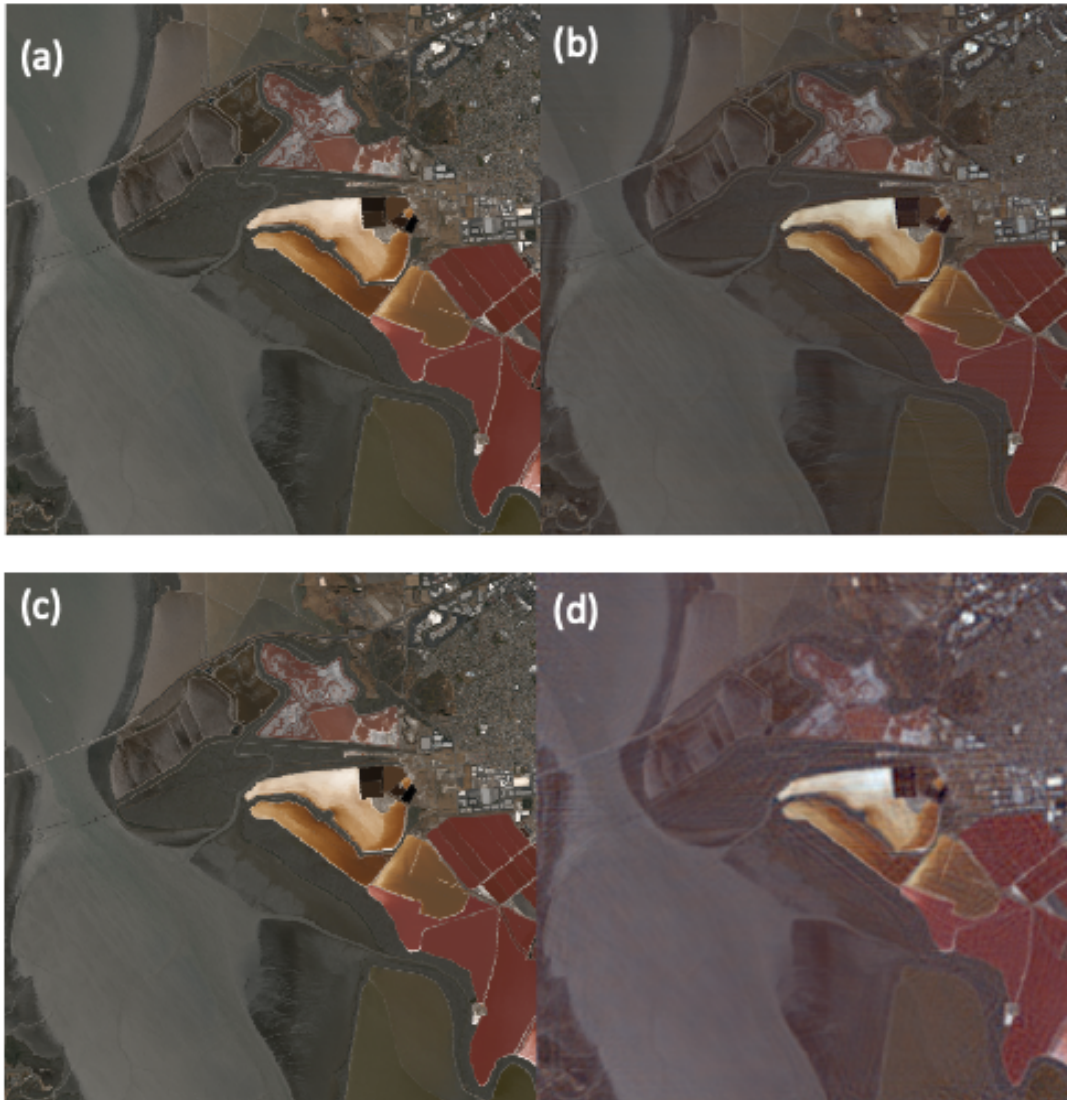
Figure 8.7: (a,c) ground-truth RGB image (b) reconstructed image blurred by half-axicon and (d) azimuthal harmonic. SSIM between (a) and (b) is 0.864 and between (c) and (d) is 0.598.

Bibliography

[1]   Mohamed Ismail Abdelrahman and Francesco Monticone. *How Thin and Efficient Can a Metasurface Reflector Be? Universal Bounds on Reflection for Any Direction and Polarization*. 2022. DOI: `10.48550/ARXIV.2208.05533`. URL: `https://arxiv.org/abs/2208.05533`.

[2]   Miguel Alcubierre. "The warp drive: hyper-fast travel within general relativity". In: *Classical and Quantum Gravity* 11.5 (1994), p. L73.

[3]   Arthur Ashkin. "Acceleration and trapping of particles by radiation pressure". In: *Physical review letters* 24.4 (1970), p. 156.

[4]   Harry A Atwater et al. "Materials challenges for the Starshot lightsail". In: *Nature materials* 17.10 (2018), pp. 861–867.

[5]   Harry A. Atwater et al. "Materials challenges for the Starshot lightsail". In: *Nature Materials* 17.10 (May 2018), pp. 861–867. DOI: `10.1038/s41563-018-0075-8`. URL: `https://doi.org/10.1038/s41563-018-0075-8`.

[6]   Gregory Benford. "Experimental Tests Of Beam-Riding Sail Dynamics". In: *AIP Conference Proceedings*. AIP, (2003).

[7]   James Benford et al. "Experimental tests of beam-riding sail dynamics". In: *AIP Conference Proceedings*. AIP, (2002).

[8]   M. Bhattacharya, A. N. Vamivakas, and P. Barker. "Levitated optomechanics: introduction". In: *Journal of the Optical Society of America B* 34.6 (June 2017), LO1. DOI: `10.1364/josab.34.000lo1`. URL: `https://doi.org/10.1364/josab.34.000lo1`.

[9] Olivia Borgue and Andreas M. Hein. "Transparent occulters: A nearly zero-radiation pressure sunshade to support climate change mitigation". In: *Acta Astronautica* 203 (Feb. 2023), pp. 308–318. DOI: `10.1016/j.actaastro.2022.12.006`. URL: `https://doi.org/10.1016/j.actaastro.2022.12.006`.

[10] Breakthrough Starshot. *Breakthrough Initiatives*. `https://breakthroughinitiatives.org/`. Accessed: June 04, 2020.

[11] Robert W Bussard. "Concepts for future nuclear rocket propulsion". In: *Journal of Jet Propulsion* 28.4 (1958), pp. 223–227.

[12] Matthew F. Campbell et al. "Relativistic Light Sails Need to Billow". In: *Nano Letters* 22.1 (Dec. 2021), pp. 90–96. DOI: `10.1021/acs.nanolett.1c03272`. URL: `https://doi.org/10.1021/acs.nanolett.1c03272`.

[13] Elias Chahine et al. "Dynamics and control of microwave-propelled sails". In: *AIAA Space Conference & Exposition.* (2003).

[14] Yin Chu, Shahin Firuzi, and Shengping Gong. "Controllable liquid crystal diffractive sail and its potential applications". In: *Acta Astronautica* 182 (May 2021), pp. 37–45. DOI: `10.1016/j.actaastro.2021.02.003`. URL: `https://doi.org/10.1016/j.actaastro.2021.02.003`.

[15] Ying-Ju Lucy Chu, Eric M. Jansson, and Grover A. Swartzlander. "Measurements of Radiation Pressure Owing to the Grating Momentum". In: *Phys. Rev. Lett.* 121 (6 Aug. 2018), p. 063903. DOI: `10.1103/PhysRevLett.121.063903`. URL: `https://link.aps.org/doi/10.1103/PhysRevLett.121.063903`.

[16] Ying-Ju Lucy Chu, Nelson V. Tabiryan, and Grover A. Swartzlander. "Experimental Verification of a Bigrating Beam Rider". In: *Phys. Rev. Lett.* 123 (24 Dec. 2019), p. 244302. DOI: `10.1103/PhysRevLett.123.244302`. URL: `https://link.aps.org/doi/10.1103/PhysRevLett.123.244302`.

[17] Ying-Ju Lucy Chu et al. "Parametric control of a diffractive axicon beam rider". In: *Optics Letters* 46.20 (Oct. 2021), p. 5141. DOI: `10.1364/ol.438954`. URL: `https://doi.org/10.1364/ol.438954`.

[18] K. Deb et al. "A fast and elitist multiobjective genetic algorithm: NSGA-II". In: *IEEE Transactions on Evolutionary Computation* 6.2 (Apr. 2002), pp. 182–197. DOI: `10.1109/4235.996017`. URL: `https://doi.org/10.1109/4235.996017`.

[19] Kalyanmoy Deb et al. "A fast and elitist multiobjective genetic algorithm: NSGA-II". In: *IEEE transactions on evolutionary computation* 6.2 (2002), pp. 182–197.

[20] Kalyanmoy Deb et al. "A fast and elitist multiobjective genetic algorithm: NSGA-II". In: *IEEE transactions on evolutionary computation* 6.2 (2002), pp. 182–197.

[21] MEEP Developers. *Yee Lattice*. URL: https://meep.readthedocs.io/en/latest/Yee_Lattice/.

[22] K Dholakia and T Čižmár. "Shaping the future of manipulation". In: *Nature Photonics* 5.6 (May 2011), pp. 335–342. DOI: 10.1038/nphoton.2011.80. URL: https://doi.org/10.1038/nphoton.2011.80.

[23] CJ Everett and SM Ulam. *On a Method of Propulsion of Projectiles by Means of External Nuclear Explosions. Part 1*. Tech. rep. LOS ALAMOS SCIENTIFIC LAB ALBUQUERQUE NM, 1955.

[24] Zhiyuan Fan et al. "Perfect Diffraction with Multiresonant Bianisotropic Metagratings". In: *ACS Photonics* 5.11 (2018).

[25] Shahin Firuzi, Yu Song, and Shengping Gong. "Gradient-index solar sail and its optimal orbital control". In: *Aerospace Science and Technology* 119 (Dec. 2021), p. 107103. DOI: 10.1016/j.ast.2021.107103. URL: https://doi.org/10.1016/j.ast.2021.107103.

[26] Robert L Forward. "Antimatter propulsion". In: *J. Br. Interplanet. Soc.;(United Kingdom)* 35 (1982).

[27] Robert L Forward. "Roundtrip interstellar travel using laser-pushed lightsails". In: *Journal of Spacecraft and Rockets* 21.2 (1984).

[28] Rafael C Gonzalez, Richard Eugene Woods, and Steven L Eddins. *Digital image processing using MATLAB*. Pearson Education India, 2004.

[29] Shulabh Gupta. "Single-order transmission diffraction gratings based on dispersion engineered all-dielectric metasurfaces". In: *Journal of the Optical Society of America A* 33.8 (2016).

[30] William M Haynes, David R Lide, and Thomas J Bruno. *CRC handbook of chemistry and physics*. CRC press, 2016.

[31] Gary B Hughes et al. "DE-STAR: phased-array laser technology for planetary defense and other scientific purposes". In: *Nanophotonics and Macrophotonics for Space Environments VII*. Vol. 8876. SPIE. 2013, pp. 132–146.

[32] Ognjen Ilic and Harry A. Atwater. "Self-stabilizing photonic levitation and propulsion of nanostructured macroscopic objects". In: *Nature Photonics* 13.4 (Mar. 2019), pp. 289–295. DOI: `10.1038/s41566-019-0373-y`. URL: `https://doi.org/10.1038/s41566-019-0373-y`.

[33] Les Johnson, Grover A Swartzlander, and Alexandra Artusio-Glimpse. "An overview of solar sail propulsion within NASA". In: *Advances in Solar Sailing* (2014), pp. 15–23. URL: `https://ntrs.nasa.gov/api/citations/20140000641/downloads/20140000641.pdf`.

[34] Montgomery H Johnson and Edward Teller. "Intensity changes in the Doppler effect". In: *Proceedings of the National Academy of Sciences* 79.4 (1982), pp. 1340–1340.

[35] Thomas Kailath. *Linear systems*. Prentice-Hall, (1980).

[36] Hassan K Khalil and Jessy W Grizzle. *Nonlinear systems*. Vol. 3. Prentice hall Upper Saddle River, NJ, 2002.

[37] Avinash Kumar, Daniel Kindem, and Ognjen Ilic. "Optomechanical Self-Stability of Freestanding Photonic Metasurfaces". In: *Physical Review Applied* 16.1 (July 2021). DOI: `10.1103/physrevapplied.16.014053`. URL: `https://doi.org/10.1103/physrevapplied.16.014053`.

[38] John Denholm Lambert. *Numerical methods for ordinary differential systems: the initial value problem*. John Wiley & Sons, Inc., 1991.

[39] Kevin Luke et al. "Broadband mid-infrared frequency comb generation in a Si_3N_4 microresonator". In: *Optics Letters* 40.21 (Oct. 2015), p. 4823. DOI: `10.1364/ol.40.004823`. URL: `https://doi.org/10.1364%2Fol.40.004823`.

[40] H.S. Malvar, Li-wei He, and R. Cutler. "High-quality linear interpolation for demosaicing of Bayer-patterned color images". In: *2004 IEEE International Conference on Acoustics, Speech, and Signal Processing*. IEEE. DOI: `10.1109/icassp.2004.1326587`. URL: `https://doi.org/10.1109/icassp.2004.1326587`.

[41] Zachary Manchester and Abraham Loeb. "Stability of a Light Sail Riding on a Laser Beam". In: *The Astrophysical Journal Letters* 837.2 (2017).

[42] Colin Robert McInnes. *Solar Sailing*. Springer London, 1999. DOI: 10.1007/ 978-1-4471-3992-8. URL: https://doi.org/10.1007/978-1-4471-3992-8.

[43] V. J. MODI. "Attitude Dynamics of Satellites with Flexible Appendages-A Brief Review". In: *Journal of Spacecraft and Rockets* 11.11 (Nov. 1974), pp. 743–751. DOI: 10.2514/3.62172. URL: https://doi.org/10.2514/3.62172.

[44] NeXolve LaRC CP1 Polyimide. https://www.matweb.com/search/datasheet_print.aspx?matguid=290379e273ae48139ac2628a3a9610e4. Accessed: Jan 2023.

[45] Ardavan F. Oskooi et al. "Meep: A flexible free-software package for electromagnetic simulations by the FDTD method". In: *Computer Physics Communications* 181.3 (Mar. 2010), pp. 687–702. DOI: 10.1016/j.cpc.2009.11.008. URL: https://doi.org/10.1016/j.cpc.2009.11.008.

[46] Ardavan F. Oskooi et al. "Meep: A flexible free-software package for electromagnetic simulations by the FDTD method". In: *Computer Physics Communications* 181.3 (Mar. 2010), pp. 687–702. DOI: 10.1016/j.cpc.2009.11.008. URL: https://doi.org/10.1016/j.cpc.2009.11.008.

[47] Elena Popova, Messoud Efendiev, and Ildar Gabitov. "On the stability of a space vehicle riding on an intense laser beam". In: *Mathematical Methods in the Applied Sciences* 40.4 (2017).

[48] Mohammad Mahdi Salary and Hossein Mosallaei. "Photonic Metasurfaces as Relativistic Light Sails for Doppler-Broadened Stable Beam-Riding and Radiative Cooling". In: *Laser & Photonics Reviews* 14.8 (July 2020), p. 1900311. DOI: 10.1002/lpor.201900311. URL: https://doi.org/10.1002/lpor.201900311.

[49] Hakob Sarkissian et al. "Polarization-controlled switching between diffraction orders in transverse-periodically aligned nematic liquid crystals". In: *Optics Letters* 31.15 (2006).

[50] Edl Schamiloglu et al. "3-D simulations of rigid microwave-propelled sails including spin". In: *AIP Conference Proceedings*. AIP. (2001).

[51] Anthony E Siegman and AE Siegman. *An introduction to lasers and masers*. McGraw-Hill, (1971).

[52] Prateek R Srivastava, Ying-Ju Lucy Chu, and Grover A Swartzlander. "Stable diffractive beam rider". In: *Optics letters* 44.12 (2019).

[53] Prateek R. Srivastava, Ying-Ju Lucy Chu, and Grover A. Swartzlander. "Stable diffractive beam rider". In: *Optics Letters* 44.12 (June 2019), p. 3082. DOI: 10.1364/ol.44.003082. URL: https://doi.org/10.1364/ol.44.003082.

[54] Prateek R. Srivastava and Grover A. Swartzlander. "Optomechanics of a stable diffractive axicon light sail". In: *The European Physical Journal Plus* 135.7 (July 2020). DOI: 10.1140/epjp/s13360-020-00542-1. URL: https://doi.org/10.1140/epjp/s13360-020-00542-1.

[55] Anirban S. Swakshar, Seongsin M. Kim, and Grover A. Swartzlander. "Broadband radiation pressure on a small period diffractive film". In: *Optics Express* 30.25 (Nov. 2022), p. 45279. DOI: 10.1364/oe.473004. URL: https://doi.org/10.1364/oe.473004.

[56] Grover A Swartzlander. "Radiation pressure on a diffractive sailcraft". In: *Journal of the Optical Society of America B* 34.6 (2017).

[57] Grover A. Swartzlander. "Radiation pressure on a diffractive sailcraft". In: *Journal of the Optical Society of America B* 34.6 (May 2017), p. C25. DOI: 10.1364/josab.34.000c25. URL: https://doi.org/10.1364/josab.34.000c25.

[58] Grover A. Swartzlander. "Theory of radiation pressure on a diffractive solar sail". In: *Journal of the Optical Society of America B* 39.9 (Sept. 2022), p. 2556. DOI: 10.1364/josab.468588. URL: https://doi.org/10.1364/josab.468588.

[59] K Tsander. *From a Scientific Heritage, NASA Technical Translation TTF-541, 1967, a translation of Iz Nauchnogo Naslediya*. 1924.

[60] Konstantin Eduardovich Tsiolkovsky. "Extension of man into outer space". In: *Proceedings of the Symposium on Jet Propulsion*. Vol. 2. 1921.

[61] Dylan C Ullery et al. "Strong Solar Radiation Forces from Anomalously Reflecting Metasurfaces for Solar Sail Attitude Control". In: *Scientific reports* 8.1 (2018), p. 10026.

[62] David Voelz. "Computational fourier optics: a MATLAB tutorial". In: Society of Photo-Optical Instrumentation Engineers. 2011.

[63] Kedi Wu et al. "Author Correction: Modelling of free-form conformal metasurfaces". In: *Nature Communications* 11.1 (Oct. 2020). DOI: 10.1038/s41467-020-18924-5. URL: https://doi.org/10.1038/s41467-020-18924-5.

[64] Kedi Wu et al. "Modelling of free-form conformal metasurfaces". In: *Nature Communications* 9.1 (Aug. 2018). DOI: 10.1038/s41467-018-05579-6. URL: https://doi.org/10.1038/s41467-018-05579-6.

[65] Peng Zhang et al. "General passive stability criteria for a Sun-pointing attitude using the metasurface sail". In: *Aerospace Science and Technology* 122 (Mar. 2022), p. 107380. DOI: 10.1016/j.ast.2022.107380. URL: https://doi.org/10.1016/j.ast.2022.107380.